Study of Second Generation High Temperature Superconducting Coils for Energy Storage System

Zhang, Huiming

Award date:
2016

Awarding institution:
University of Bath

Study of Second Generation High Temperature Superconducting Coils for Energy Storage System

by

Huiming Zhang

Supervisor: Dr. Weijia Yuan

Thesis submitted for the degree of

Doctor of Philosophy

in

The department of

Electronic and Electrical Engineering
University of Bath

February 2016

Signature: Date:

Acknowledgements

I would like to thank my supervisor Dr. Weijia Yuan. He has guided me into the amazing research area of superconductivity which makes full use of my educational background. Also, his passion and creativity have shown me an excellent example of the academic field. His encouragement continually inspires me for the work ahead.

I would also like to thank Dr. Min Zhang for her thoughtful discussion during the past two years. I would like to express my gratitude to Dr. Zanxiang Nie and Dr. Xi Xiao at Tsinghua University. Their help in electronic development has been of vital importance. Dr. Paul Leonard, Dr. Jiahui Zhu and Dr. Wenjiang Yang deserve my warmest thanks for their kind discussion and support.

I also wish to thank the students in my office. Their passions and pursuit for knowledge propel me to reach further in my research. Working in this environment gives me the greatest happiness.

Finally, my parents and younger brother deserve much gratitude for their support behand.

Abstract

Emerging energy technologies give us the opportunity to manage the challenges posed by climate change, environmental degradation and oil shortages. Superconducting energy storage system (SMES) is a promising candidate technology due to its potential for promoting renewable energy and stabilising grid systems. It enables improvements to power grid capacity, reliability and efficiency. SMES also has the advantages of high cyclic efficiency, quick response times, deep discharge and recharge abilities and being easy to build hybrid energy storage system. This dissertation studies the key technologies for the design and application of SMES using 2G HTS materials.

The first part of this dissertation investigates through experiments the behaviour of 2G HTS tape under an external magnetic field and impregnation. It is found that that the critical current and *n* value are closely related under a magnetic field, which can be verified by theoretical analysis. Different impregnation materials are tested to enhance the superconducting tapes. The experiments find that Gallinstan does not cause degradation of the impregnated tape. However, the degree of degradation caused by different resins varies: Stycast Black degrades the tape a small amount, while Stycast 1266 and Araldite degrade the tape considerably. Reasons for the degradation are discussed and suggestions for coils fabrication are presented.

Superconducting coils are studied experimentally and numerically under self field and an external field. This numerical model is based on minimization of the magnetic energy using the line current assumption. Good agreement was achieved between the numerical model and the experiments. Then the coils with two different tapes are investigated under a DC magnetic field. The load line method is improved to take into account the anisotropy in 2G HTS coils. In order to calculate the magnetic field and AC losses of a stack of superconducting coils, coupling of the critical state model with the line front track approximation is proposed and validated.

Some critical issues related to SMES design are discussed. A conceptual design of a 60 kJ SMES is presented. The design process includes magnetic optimization, current

lead design and cooling system selection. This SMES is then hybridized with a battery and applied in wave generator system to analyse the extension of battery life. Finally, different configurations of SMES are compared and an economic analysis is performed.

Original work in this dissertation includes:

1. Multiphysics modelling of HTS coils using magnetic energy minimization based on homemade finite element analysis code. This method couples the magnetic energy minimization with magnetic, thermal and mechanical fields for the first time, and efficiently simulates the superconducting coils using fewer elements and avoiding high non-linearity.

2. Efficient numerical modelling of a stack of HTS pancake coils using the line front track approximation. Accurate current distribution, magnetic field and AC losses are calculated and compared to established H-formula methods. This method is further applied to a real 2G HTS SMES design for the first time.

3. Detailed conceptual design of a 60 kJ HTS SEMS, which is hybridized with a battery to smooth the output of the renewable energy system. Extension of the battery lifetime is modelled and discussed for the first time, based on the rainflow counting method.

Table of Contents

List of Figures

List of Abbreviations

1G	First Generation
2G	Second Generation
AC	Alternate Current
ASTM	American Society for Testing and Materials
BSCCO	Bismuth Strontium Calcium Copper Oxide
CSM	Critical State Model
DC	Direct Current
DDLWEC	Direct Drive Linear Wave Energy Converters
DOD	Depth of discharge
FACTS	Flexible AC Transmission System
FEM	Finite Element Method
HTS	High Temperature Superconductor
LTS	Low Temperature Superconductor
MMEV	Minimum Magnetic Energy Variation
PCS	Power Condition System
PDE	Partial Differential Equation
SMES	Superconducting Magnet Energy Storage
SSO	Sub Synchronous Oscillation
SSR	Sub Synchronous Resonance
YBCO	Yttrium Barium Copper Oxide

List of Symbols

Symbol	Description	Unit
A	Magnetic vector potential	*Wb/m*
A^k	Magnetic vector potential for the *k*th element	*Wb/m*
A_i^m	Magnetic vector potential of the *i*th element at *m*th step	*Wb/m*
B	Magnetic flux density	T
B_0	Characteristic magnetic field	T
$B_{0\perp}$	Characteristic magnetic field in the perpendicular direction	T
$B_{0\parallel}$	Characteristic magnetic field in the parallel direction	T
B^k	Magnetic flux density for the *k*th element	T
B_r	Magnetic flux density in the radius direction	T
B_z	Magnetic flux density in the *z* direction	T
C	Heat capacity	$J/(m^3K)$
C_d	The number of cycles-to-failure for a depth of discharge *d*	
C_I	Capacity of a battery under constant discharging current *I*	*Ah*
C_j	Voltage gauge of the *j*th tape	*V*
C_{test}	Consumed battery life during the test	
DOD	Depth of discharge	
d	Discharge depth	
d^i	Magnetic flux moving distance	*m*
E	Electric field	*V/m*
E_c	Critical electric field, $1e^{-4}$ *V/m*	*V/m*

E_S	Stored energy	*J*
E_z	Electric field in the *z* direction	*V/m*
E_θ	Circumferential electric field	*V/m*
F_p	Pinning force on the vortices	*N*
F_L	Lorentz force on the vortices	*N*
f	Frequency	*Hz*
f_i^m	Magnetic vector potential of the *i*th element at the (*m-1)*th step	*Wb/m*
H	Magnetic field	*A/m*
H_c	Critical magnetic field for a Type I superconductor	*A/m*
H_{c1}	Lower critical magnetic field in a Type II superconductor	*A/m*
H_{c2}	Higher critical magnetic field in a Type II superconductor	*A/m*
H_x	Magnetic field in the *x* axis	*A/m*
H_y	Magnetic field in the *y* axis	*A/m*
I	Transporting current	*A*
I_c	Critical current	*A*
I^k	Transporting current of the *k*th element	*A*
$I_{\max}$	Peak transporting current	*A*
I_{rms}	RMS current	*A*
J	Current density	A/m^2
J'	Testing current density	A/m^2
J_c	Critical current density	A/m^2
J_{c0}	Critical current density under a self field	A/m^2
J_m	Critical current density in the subcritical region	A/m^2
J_m^i	Critical current density in the subcritical region of the *i*th pancake	A/m^2
K	Global stiffness matrix	
k	Ratio between B_{10} and B_{20}	

k_1	Thermal conductivity	*W/(mK)*
k_e	Elemental stiffness matrix	
$k_{i,j}$	The *i*th row, *j*th column of the elemental stiffness matrix *k*	
k_B	Boltzmann constant	$m^2kg/(s^2K)$
L	Inductance of a coil	*H*
L_n	Loss factor	
L_p	Pinning potential range	
l	Length of the current lead	*m*
M_i^k	Mutual inductance matrix	*H*
N	Number of turns	
N_i, N_j, N_k	Shape function	
n	N value	
P	Power of the cryocooler	*W*
Q	AC loss in one cycle	*J/cycle*
Q_I	Capacity of the discharging current *I*	
Q_{lead}	Thermal load of the current lead	*J*
R	Escaped rate	
r_0	Radius of the roil	*mm*
S	Cross-section domain	m^2
SOC	State of charge	
T	Current vector potential	
T_c	Critical temperature	*K*
T_n	Temperature	*K*
T_{test}	Period of the test	*h*
T_{total}	Estimated total battery life during the test	*h*
t	Time	*s*
t_0	Thickness of the tape	*mm*
U	Global field vector	

U_p	Pinning potential energy	J
u_i, u_j, u_k	Node displacement	m
V	Electric potential	V
V_{rms}	RMS voltage	V
w	Width of the tape	mm
γ	Anisotropy ratio	
Φ_0	Magnetic flux carried by each vortex	Wb
μ_0	Vacuum permeability	N/A^2
ν_0	Attempt frequency	Hz
θ	Angle	
ρ	Resistivity	$\Omega \cdot m$
σ	Stress tensor	Pa

Chapter 1. Introduction

1.1 Background

Climate change is one of the great challenges in the 21st century [1]. Seeking a green economy is the priority task for all countries. The transition to a sustainable and low carbon economy will involve major changes to the ways energy is supplied and used. Transforming the electricity system lies at the heart of these changes. Emerging technologies give us the opportunity to manage these challenges.

The UK electricity system faces considerable challenges. According to the UK Low Carbon Transition Plan (2009), it is expected that around 30% of electricity will be generated from renewable sources by 2020 [2]. By 2050, the electricity sector should be almost entirely decarbonized, with significantly increased levels of electricity production and demand incorporation of heat and transport sectors into the electricity system. In order to achieve these aims, it is incredibly important to increase the amount of renewable energy, such as wind, solar and ocean energy, in the power system.

The past decade has witnessed a large increase in electricity generation from renewable sources around the world, especially in wind and photovoltaic energy. The 2012 global wind power market grew by more than 10% compared to 2011, as shown in Figure 1-1, and nearly 45 GW of new wind power sources were brought online, representing investments of about £50 billions [3]. At the same time, solar and ocean energy also underwent a remarkable penetration. For example, the UK government said that 4 million homes would be powered by the sun within eight years [4], meaning that there would be 22,000 MW of installed solar power capacity by 2020.

Such a large proportion of renewable sources connected to power generation and distribution systems brings significant challenges to the power system due to their intermittent and unpredictable nature. The present power systems are built 50 years ago with few automatical devices and are not flexible enough to upgrade, leading to substantial wastage of green energy. As renewable penetration increases, it will be

economically and environmentally beneficial to promote microgrids which will be able to make the best use of local renewable energy sources. Within a microgrid, power available from renewable energy sources fluctuates dramatically depending upon the environmental conditions, e.g. wind strength and sunlight, which can vary on timescales from seconds to days. Therefore, it is a great challenge to manage the stability, security and reliability of a microgrid from the practical view.

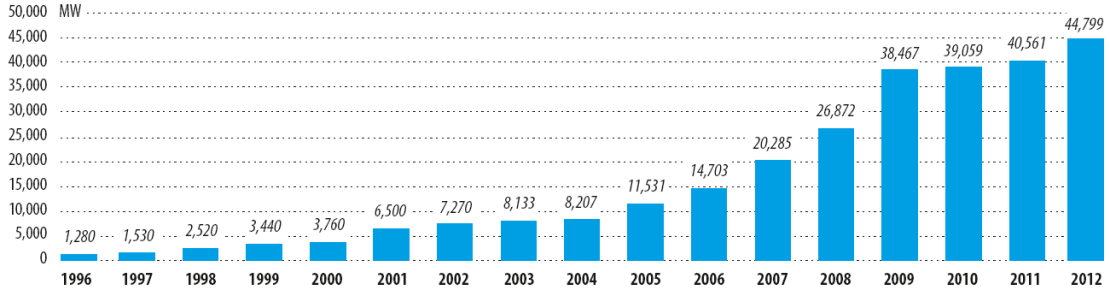

Figure 1-1 Global annual wind installed capacity before 2012 [3]. Wind generators have been installed continually during the past two decades.

The introduction of energy storage into the microgrid can alleviate the problems caused by the intermittent and unpredictable nature. Generally speaking, energy storage systems perform three functions: energy management, power bridging and power quality control. They are installed to harness the energy generated by renewable energy sources to overcome their intermittency and uncertainty. Due to the large variation in load/generation balance of renewable energy sources, an energy storage system capable of responding quickly to power fluctuations on a short timescale, ranging from seconds to minutes, will be of significant value. Therefore, a game-changing energy storage system should have large power density with fast response, to support renewable energy integration into microgrids.

Superconducting magnetic energy storage (SMES) systems are one such enabling technology, offering high power density and quick response speed. Their high power density is due to their ability to respond quickly to the demand request as the energy conversion is constrained in the electromagnetic process, and is not involving with any mechanical, hydraulic or chemical processes. Compared to conventional energy storage technologies, another advantage of SMES is the significant amount of energy saved because the energy is stored as a lossless persistent current. Moreover, the devices can

be made much smaller in size, and they are greener and safer than conventional technologies.

Investigation of SMES for power systems began in 1969, and the first system was discussed using low temperature superconductors (LTS) [5]. At present, LTS SMES, which functions using liquid helium, is technically mature and can be used to provide good quality power to end users. However, high temperature superconductors (HTS), which operate at 77 K, can operate at higher magnetic fields than LTSs, and this capability offers the potential to create more compact SMES devices. The cooling systems of HTS SMES are easier and the associated costs are decreased compared to LTS SMES. Research on HTS SMES has been a popular topic for the past decade.

Most HTS SMES projects are focused on the use of Bismuth Strontium Calcium Copper Oxide (BSCCO) superconductors, which are the first generation (1G) HTS. Superconductivity in BSCCO conductors was discovered in the late 1980s and commercial SMES beame available in the 1990s. So far, several HTS SMES systems based on BSCCO conductors have demonstrated the feasibility of applying HTS SMES to power systems [6-8]. However, it was also found that wide application of BSCCO-related SMES was very challenging for two major reasons. Firstly, the cost of BSCCO superconductors is high, and further price reduction is difficult because large amounts of silver are indispensable during the fabrication process [9]. Secondly, the performance of 1G HTS is poor under a magnetic field, which decreases the efficiency of superconducting devices based on BSCCO conductors [10].

The second generation (2G) HTS tapes, based on Yttrium-Barium-Copper-Oxide (YBCO), are state-of-the-art conductors with significantly higher irreversibility fields and critical current density values in an external magnetic field. They can be operated either by liquid nitrogen, gaseous helium, or commercial cryocoolers, thereby eliminating the requirement for expensive liquid helium. In the near future, 2G HTS will be developed with a substantial increase in critical current density, along with a lower cost in terms of dollar per kiloamp-meter ($/kA•m) than 1G HTS and copper [10]. This means that even taking into account the cooling cost, 2G HTS SMES systems will be cost competitive compared to conventional technologies. Thus, the technology is now on the edge of inclusion in widespread industrial applications. There is now a critical opportunity to develop 2G HTS SMES systems.

Magnesium diboride MgB_2 shows a wide application prospect in the field of low field application for its relatively simple structure and rather higher critical temperature than LTS. It can be operated in the environment of liquid H_2 and thus reduce the cryogenic cost. Compared with 2G HTS, the obvious advantages of MgB_2 includes the cheap material and isotropic magnetic property which makes it attractive for 20K application. So far, there are some conceptual designs for MgB_2 in energy storage system[11-14].

A number of countries are active in developing SMES technology using 2G HTS conductors, including a 2.5 MJ SMES system for grids in the U.S., a 2.5 MJ SMES system for power quality in Korea [15] and a MJ-range SMES for voltage quality in Japan [16].

This dissertation studies the key technologies for design and application of SMES in power system. The first part of this dissertation investigates the behaviour of 2G HTS tapes under external magnetic field and impregnation through experiments. This is followed by studying superconducting coils experimentally and numerically under self field and external field. This numerical model is based on minimization of magnetic energy with sheet current model. In order to calculate the magnetic field and AC losses of a stack of superconducting coils, line front track approximation is proposed. Finally primary design and application of SMES system in renewable energy generation are presented and discussed.

1.2 Scope of the study

Superconducting coils are the core components of superconducting devices, especially for a superconducting magnetic energy storage system. Our research is focused on solving the issues that arise during the fabrication and modelling of superconducting coils, employing the recently developed numerical models and technologies. Among these problems, the decisive factor is the estimation of AC losses and critical current, because it determines the rated operating conditions and the cryogenic system design.

Firstly, achieving a high current-carrying capability in the superconductors is one of the most important objectives for superconducting device design. However, the critical current is often constrained by the existence of an external magnetic field, as the critical currents of HTSs are field dependent. In addition to this, the impregnation process also

induces critical current degradation due to the thermal mismatch properties between the superconductor and the impregnation materials. Further research on single tape performance under an external magnetic field and impregnation is necessary. These experiments will not only help to select the proper superconductors and the impregnation materials, but also provide raw data for the numerical model which can be used to predict the performance of superconducting coils.

Secondly, critical current and AC losses are two major parameters that characterize the performance of the superconducting coils. Critical current is a key factor for the stored energy, and AC loss determines the operating conditions and cryogenic system design. Thus, prediction of the critical current and the AC loss are critical to superconducting coil design. However, accurate and quick estimation of the critical current and AC loss values of HTS coils is very challenging. First, superconductivity is a very complex physical phenomenon. The relationship between the electric field, E, and current density, J, is highly non-linear. Secondly, the geometry of a HTS tape has a large aspect ratio, resulting in huge numbers of meshes in a numerical simulation. Thirdly, the strong field dependencies of the critical current on magnetic, thermal and strain fields require multiphysics modelling. Efficient numerical modelling of superconducting coils is therefore of vital importance.

The third area in this research is the feasibility study of integrating a superconducting energy storage system with renewable energy generation, from technical and economic perspectives. One problem in SMES design is to calculate the AC losses of the superconducting coils for its intensive calculation problem. We aim to propose one efficient calculation scheme for large SMES coil. The SMES, hybridized with battery, is used to stabilize the voltage output of a wave generator, which proves the feasibility in renewable energy integration. Finally, we consider the cost of different configurations for kJ, MJ and GJ SMES, from the economic aspects.

1.3 Structure of the dissertation

This dissertation will investigate all the aforementioned problems related to superconducting coils, with the aim of proposing an engineering solution for application of superconducting energy storage system. The structure of this dissertation is as follows:

Chapter 2 presents a brief introduction to superconductivity, including the main commercially available high temperature superconductor materials. Modelling methods used for superconducting simulation are reviewed and their pros and cons are summarized. Finally, the SMES system and its development history are introduced.

Chapter 3 proceeds to research 2G HTS tapes under an external magnetic field and impregnation. The critical currents and the *n*-values are measured under a varying external DC magnetic field. The magnetic field dependency of the critical current and the *n*-value is discussed and analysed. Different impregnation materials are introduced and their influences on the critical current and AC losses are investigated.

Chapter 4 presents experimental and numerical investigations on single 2G superconducting coils. The critical current and AC losses of several pancake coils are measured. These results are compared to numerical results based on minimization of the magnetic field energy. The critical currents of these coils under a DC magnetic field are also investigated and calculated.

In Chapter 5, a numerical model based on the line front track for a multi-pancake coil is proposed and validated. This model is compared to and verified by current distribution and AC loss results obtained from H formula. This model is further used to study the AC losses of a stack of pancake coils in a 2 kJ SMES system.

Chapter 6 presents a conceptual design process of a 60 kJ SMES-battery hybrid energy storage system. The optimal configuration of a 60 kJ SMES for a wave generator is achieved based on electromagnetic field simulation. The life time of the battery is analyszed using rainflow counting algorithm. This is followed by the economic analysis of different scale SMES systems.

Finally, Chapter 7 gives concluding remarks, as well as some ideas for future work.

1.4 Thesis contributions

The main contributions from this thesis can be summarised as follows:

1. Fully multiphysics modelling of 2G HTS coils is proposed and validated using magnetic energy minimization, based on homemade finite element analysis code. This method couples the magnetic energy minimizaiton with magnetic, thermal and

mechanical fields for the first time and simulates the superconducting coils efficiently for less elements and avoiding high non-linearity. Critical current and AC losses of the 2G HTS coils can be calculated accurately and efficiently. This model can be used to analyse the thermal and mechanical process when the superconducting coil charges and discharges.

2. Efficient numerical modelling of a stack of HTS pancake coils with thousands of turns is presented using line front track approximation. Accurate current distribution, magnetic field and AC losses are calculated and compared with established H-formula methods. We further analyze the screening current and the AC losses in different pancakes, finding that most part of the losses is generated in the top and bottom coils. This method is further applied in a real 2G HTS SMES design for the first time.

3. Design of a hybrid energy storage using an SMES system and battery. The full details are presented for the design of a 60 kJ SMES. The electromagnetic and mechanical fields are calculated using the line front approximation. This SMES is applied to a renewable energy system. Extension of the battery life time with the use of SMES is discussed using the rainflow counting method. Rough cost estimation of the SMES system with different energy scales is presented and discussed.

Chapter 2. Superconductivity and Superconducting Energy Storage

Superconductivity was discovered in 1911 by Kamerlingh Onnes, shortly after helium gas was first liquefied. The special properties of superconductors, such as zero-resistance and the Meissner Effect drove electrical engineers to develop new technologies and design new devices [9]. This chapter gives a brief introduction to superconductors and theories. Particular attention is paid to the simulation of 2G HTS superconducting coils. Finally, a short introduction to SMES technologies and projects are presented.

2.1 Fundamentals of superconductivity

2.1.1 History

The early history of superconductivity was closely related to the development of cryogenic technology. In 1908, in a laboratory at Leiden University, the Dutch physicist Heike Kamerlingh Onnes successfully liquefied helium for the first time in history. Three years later, when Onnes was measuring the resistance of mercury in liquid helium, he found that the resistance vanished abruptly and completely instead of decreasing continuously upon cooling as expected. His further work on this topic confirmed this unexpected result, and it was at this point that the word “superconductivity” was coined to describe this new state of matter [9]. The discovery of superconductivity earned Kamerlingh Onnes a Nobel Prize in 1913.

In the following decades, many pure metals were found to behave in a similar way to liquid helium, as well as some alloys, such as NbTi and Nb_3Sn. These materials were called low temperature superconductors (LTSs), as their superconductivity only existed below 40 K. The alloys were more attractive compared to the pure metal

superconductors, since they could remain the superconducting state under rather high magnetic fields and had many potential applications in high energy physics facilities.

However, the expense required to sustain the low temperature environment was enormous and their practical applications were limited for a long time. Considerable progress was made in 1986, by discovering the superconductivity of ceramic cuprates at temperatures above 77 K. Owing to the discovery of superconductivity in temperatures achievable using liquid nitrogen, Muller and Benodz were awarded the 1987 Nobel Prize. This remarkable discovery excited the whole superconductivity community and very rapid progress was made in the late 1980s. In the early 1990s, BSCCO was made commercially available, and was termed as 1G HTS. Soon it was found that the current carrying capability of BSCCO degraded rapidly under an external magnetic field. Adding to this, silver was the primary raw material required for the fabrication process, which made it very hard to decrease the price of the material. Because of these problems, the efficiency and cost of BSCCO devices were unattractive. In the middle of the 2000s, YBCO tape was commercially produced at a scale of 100 m. It could transport large currents in a high magnetic field. Research and use of YBCO superconductors has been very active during the past several years. At the same time, continuously efforts have also been made to improve the performance of BSCCO conductors. The latest progress in BSCCO 2212 is that the critical current of round BSCCO wire has been improved and generates 2.6 T in 31.2 T background field [17].

2.1.2 Superconducting properties

Superconductivity is widely perceived to be a phenomenon of zero electrical resistance. In a superconductor the voltage drops abruptly to zero when the material is cooled below its critical temperature. Another way to demonstrate this property is by inducing persistent current in a circuit loop. An electric current flowing through a loop of superconducting wire can persist for a long time without a power source. More precise measurement reveals that the resistance of a superconductor is smaller than 10^{-25} Ωm. For comparison, the resistance of copper is 10^{-8} Ωm at room temperature, and 10^{-10} Ωm at liquid nitrogen temperature. This property is traditionally named as zero-resistance or ideal conductivity.

Most superconducting devices employ the fundamental property that they can carry current without energy dissipation. This feature only exists when the transporting

current density is below a certain value, the critical current, I_c. If the current density exceeds I_c, the superconductivity disappears, known as quenching. The critical current I_c is characterized by the critical electric field of E_c, $1e^{-4}$ V/m, in the *E-I* curve. A typical *E-I* curve is presented in Figure 2-1. Unlike a traditional conductor, depicted by the linear Ohm's law, a superconductor can be described using the *E-J* power law:

$$E = E_c \left(\frac{I}{I_c} \right)^n \qquad \text{Equation 2-1}$$

where E is the longitudinal electric field along the superconductor, and n is a characteristic parameter, often larger than 20.

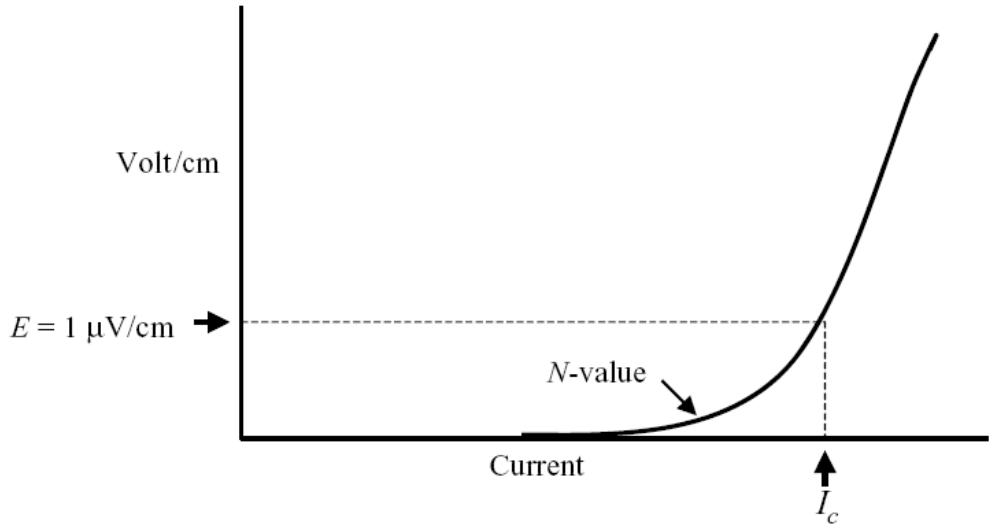

Figure 2-1 Typical *E-I* curve of superconductors. The critical current is defined by the voltage drop of 1 $\mu V/cm$.

Although zero-resistance is straightforward in characterizing superconductors, the fundamental criterion for superconductivity is the Meissner Effect. Meissner and Ochsenfeld observed that when pure tin was cooled in the presence of a magnetic field, on reaching its superconducting transition temperature the magnetic flux was suddenly completely expelled from its interior, as shown in Figure 2-2. This discovery became known as Meissner Effect. The Meissner Effect is similar to diamagnetism in other normal materials. The difference is that superconductors can expel the magnetic flux completely, showing that they are perfect diamagnetic materials.

The London model shows that the Meissner Effect results from the induced current in the surface of the conductor, and the thickness of the induced current is called

penetration depth. The Meissner Effect allows the current to penetrate from the boundary to the centre when the applied current increases.

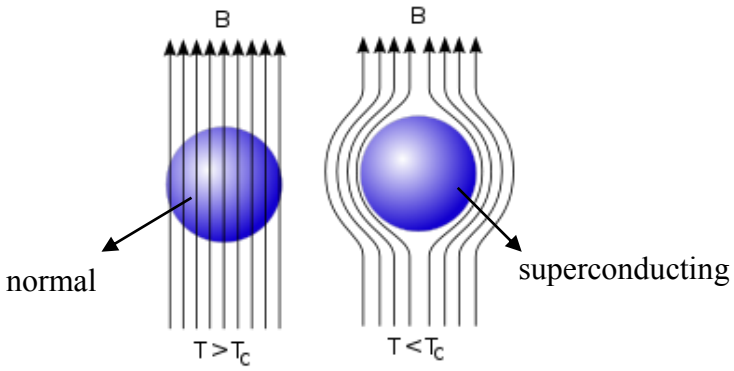

Figure 2-2 A superconductor under an external magnetic field expels the magnetic field inside the conductor. This is named as the Meissner Effect.

The existence of superconductivity is highly dependent on the surrounding physical conditions. Temperature, magnetic field and current density are three typical major parameters. Each parameter has its own critical value, defined by the superconducting/normal transition process, denoted by T_c, H_c and J_c. For example, the critical temperature of certain superconductors marks the emergence of superconductivity when the conductor is continually cooled. The relationship between critical temperature, critical magnetic field and critical current is very complex. Figure 2-3 presents the critical surface of *T-H-J* for a superconductor.

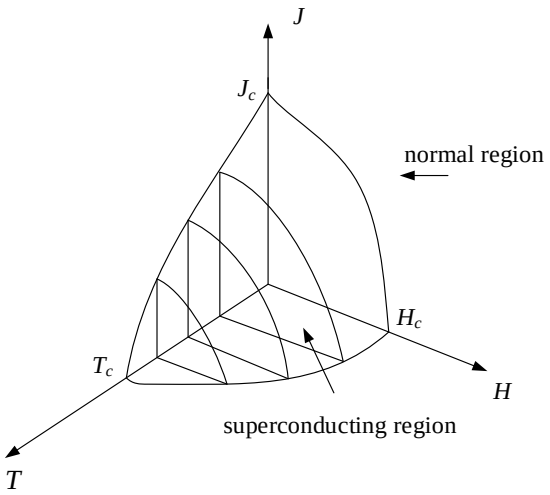

Figure 2-3 The critical surface of *T-H-J* for superconductors. The zone within the surface is the superconducting region, and the remainder of the zone is the normal region.

Based on the behaviour of superconductors under a magnetic field higher than the critical magnetic field, superconductors can be classified into two groups. Some superconductors return to a normal state, while others enter a mixed state. Type I superconductors have only a superconducting state and a normal state. Thus, they have only one critical magnetic field H_c value, as shown in Figure 2-4(a). Most metallic superconductors belong to this group. Type II superconductors have three states: the superconducting state, the mixed state and the normal state, as shown in Figure 2-4(b). The two boundaries between these three regions are H_{c1} and H_{c2}, respectively. Examples of type II materials are alloys and compounds such as Nb_3Sn, NbTi, MgB_2 and all high-T_c cuprates.

The critical fields, $\mu_0 H_c$, for type I superconductors are relatively low, i.e. 10 mT, which means that even their self-fields can destroy the superconducting state. Applications of type I superconductors are therefore limited. On the other hand, the upper critical fields H_{c2} of type II superconductors can be very high (At 4 K the upper critical field for H_{c2} is 12 T for NbTi, 27 T for Nb_3Sn, 15 T for MgB_2, and > 100 T for YBCO and Bi-2223 [28]), indicating their potential use in high field magnets. This thesis is therefore interested in type II superconductors.

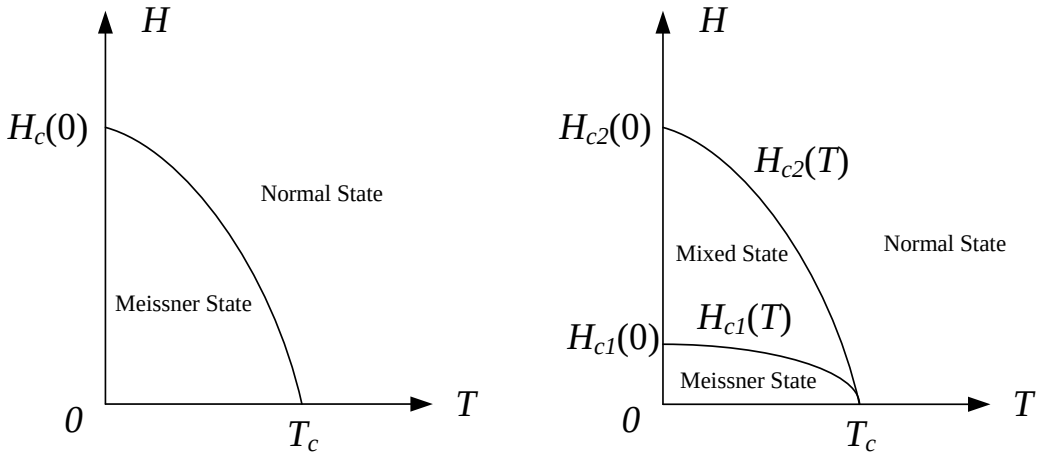

(a) (b)

Figure 2-4 Phase diagrams of Type I and Type II superconductors. Type I superconductors have two regions: Meissner State and Normal State; Type II superconductors have three states, Meissner State, Normal State and Mixed State.

Most power superconducting applications require that the superconductor is in the form of a long, strong and flexible conductor so that it can replace traditional wires.

However, current HTS materials are easily cracked due to their ceramic nature. YBCO tape is produced by coating YBCO powder onto a specially prepared substrate. Figure 2-5 shows the typical structure of a coated YBCO superconductor. The YBCO layer is only 1 μm thick. And it has been demonstrated that the thicker the superconducting layer, the lower the current density the tape can carry [18].

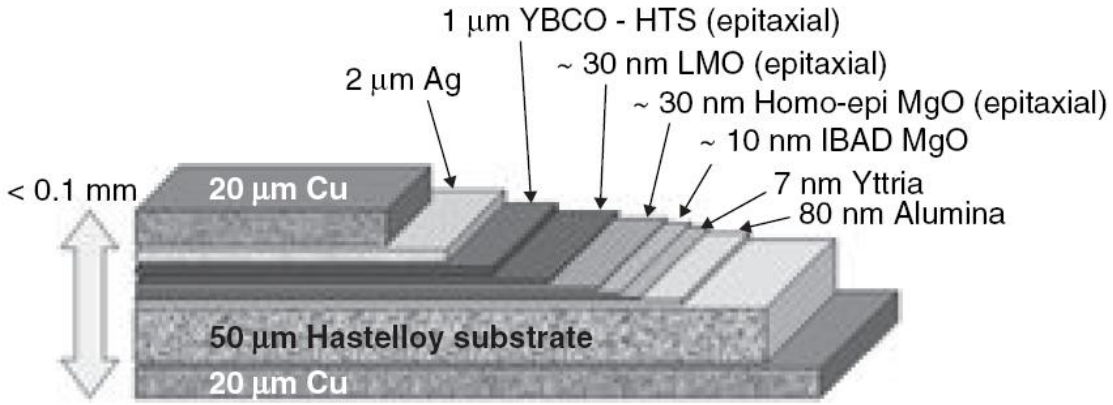

Figure 2-5 Configuration of a YBCO coated superconductor [10]. The superconducting YBCO layer is 1 μm thick, and is surrounded by substrate and stabilizer.

In order to investigate the macro behaviour of a superconductor in magnetic field, Bean proposed the famous critical state model (CSM) in the 1960s [19, 20]. The CSM divided a superconductor into two regions: the penetrated area or critical region, and the unpenetrated area, also called the subcritical region. It was assumed that the current density in the critical region was equal to the constant critical current density, J_c, and the magnetic field was equal to zero in the subcritical region, which was indicated by the Meissner Effect. The Bean model has been verified by numerous experiments and it has been widely applied in analytical and numerical calculation for its simplicity. Experiments have shown that the critical current is degraded under a magnetic field, as depicted in Figure 2-6. Kim [21] raised a new model, now called the Kim model, to modify the constant J_c assumption in the CSM. He claimed that the critical current depended on the local magnetic flux density, B:

$$J_c(B) = J_{c0}\frac{B_0}{B + B_0} \qquad \text{Equation 2-2}$$

where J_{c0} is the critical current density with no external field, and B_0 is a fitting parameter obtained from experimental results, as shown in Figure 2-6.

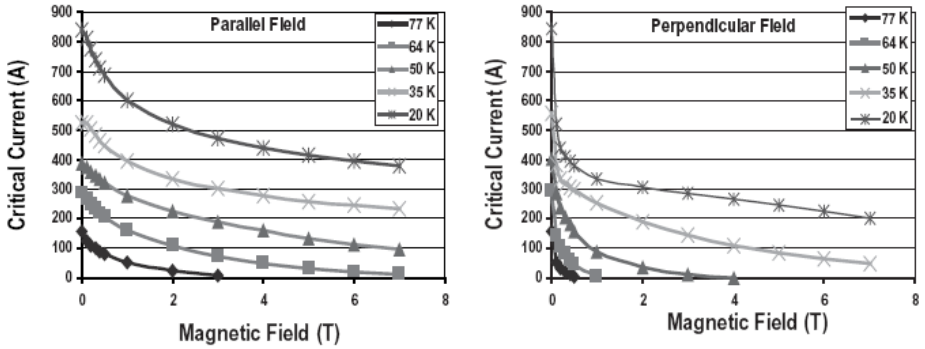

Figure 2-6 Critical current as a function of the parallel and perpendicular magnetic fields at different temperatures for YBCO tape by AMSC in 2006. The critical current is decreased by the existence of an external magnetic field [10].

2.1.3 Superconducting theories

Since the discovery of superconductivity in 1911, the physics community has been eager to explore its mechanism. Although the journey to the theory of superconductivity is still continuing, there have been many achievements and these theories have greatly extended our understanding to superconductivity.

In 1934, the Dutch physicists Gorter and Casimir proposed a simple physical model, the two-fluid model, based on a thermodynamic treatment of superconductivity [22]. This model introduced two new points:

(1). After transition to the superconducting state, some of the free electrons are "frozen" as ordered superconducting electrons. Thus the total electrons can be divided into two parts: superconducting electrons and normal electrons. The ratio of superconducting electrons to total electrons is closely related to the temperature. When the temperature decreases to absolute zero degree, all the electrons become superconducting.

(2). The zero resistivity is due to the fact that superconducting electrons are different from normal electrons in terms of their motion. Normal electrons induce resistance because of electron scattering, while the superconducting electrons follow a completely ordered motion with no scattering.

The two-fluid model is a phenomenological model which can explain a few superconducting phenomena. It can give a rough understanding of superconductivity at the macro level. This marks the first step of developing a superconductivity theory.

The second step was made by the London brothers, who suggested the London model to explain the Meissner Effect [23]. To maintain the Meissner Effect, there was a superconducting current flowing within the very small penetration depth along the surface. The penetration depth was negligible compared to the superconducting thickness. Another contribution of the London model was that it laid the foundation to utilize the Maxwell equation to describe the electromagnetic behaviour of superconductors.

One of the major achievements of the 1950s was the establishment of the Ginzburg-Landau theory [24]. This theory assumed that the emergence of superconductivity was the result of second-order phase transitions. It bridged the macro phenomenon with micro parameters by revealing the quantum nature of superconductivity. A major success of the Ginzburg-Landau theory was the prediction of type-I and type-II superconductors.

Another major achievement of superconductivity research is the BCS theory [25], proposed by Bardeen, Cooper and Schrieffer. Based on BCS theory, the key to superconductivity was the introduction of the Cooper pair, which held the superconducting electrons. The formation of the Cooper pair was the consequence of the energy gap below the critical temperature, showing that a Cooper pair was more stable than a normal electron. The existence of a Cooper pair rendered the electrons resistant to scattering by the lattice vibration, which was the mechanism of zero resistance. BCS theory was considered to be a great success since it presents a reasonable explanation for the rich phenomena of superconductivity, such as the temperature dependency of the energy gap E and the critical magnetic field.

2.1.4 Superconductor materials

Parallel to the search for the mechanism of superconducting, the investigation to identify technically useful superconductors has been another hot topic over the past decades. The critical values of superconductors must be large enough for technical applications, so only type II conductors are suitable. The first superconductors used for industrial applications were two kinds of low temperature superconductors (LTS): niobium-tin (Nb_3Sn) and niobium-titanium (NbTi). Their superconductivity is successfully explained by the BCS theory.

However, the low operating temperature requirement limited their wide application. In 1986, lanthanum-barium-copper-oxide ($La_{2-x}Ba_xCu_1O_4$) was found to be superconducting with a critical temperature of 40 K. This critical temperature exceeded the upper limit of the BCS theory prediction, therefore this new group of superconductors were usually referred to as "unconventional superconductors", or "high temperature superconductors" after their high transition temperatures.

In 2001, the discovery of superconductivity in MgB_2 by Jun Akimitsu's group produced a boom in applied superconductivity research [26]. This conductor had a critical temperature of 39 K and the critical field H_{c2} of 33T, higher than that of Nb_3Sn. Thus MgB_2 seemed to be the most promising material for the next generation high field magnets and a strong competitor for Nb_3Sn and NbTi.

Six superconductors are currently used for industrial-scale applications, and are known as technical superconductors:

- Niobium-titanium (NbTi)
- Niobium-tin (Nb_3Sn)
- Bismuth-strontium-calcium-copper-oxide (BSCCO 2212)
- Bismuth-strontium-calcium-copper-oxide (BSCCO 2223)
- Rare-earth-barium-copper-oxide (REBCO)
- Magnesium-diboride (MgB_2)

Only the BSCCO2212, BSCCO2223 and REBCO superconductors can be practically used in industrial applications at 77 K (the liquid nitrogen temperature). The first two are denoted as first generation (1G) HTS materials, and are manufactured using powder-in-tube (PIT) manufacturing processes. Although the fabrication technologies are quite mature and their properties are sufficient, the high cost is a hindrance to wide usage. It is very difficult to reduce their high cost because silver is an unavoidable requirement for the fabrication process. Silver is used as a sheath material and it is crucial to the success of the PIT processes for both BSCCO 2212 and BSCCO 2223, as it is the only material that is both chemically compatible with BSCCO and permeable to oxygen at the processing temperature. It also decreases the formation temperature of the BSCCO 2223 phase. Silver comprises approximately 60% of the cross-section and thereby

contributes to a significant fraction of the cost of BSCCO 2223 wire. Besides the high cost, 1G superconductors do not perform as well as 2G REBCO conductors, under external magnetic field.

Contrary to the powder-in-tube processes used to fabricate 1G HTS, REBCO conductors are produced by multilayer coating on a textured substrate, and this techniques are named as "coated conductor technologies". Figure 2-7 presents the schematics of the epitaxial multilayer structure of 2G REBCO superconductors. A nickel alloy strip is typically used as the depositing base, upon which a buffer layer and a superconducting layer are deposited successively. The buffer layer prevents metal atoms from diffusing from the substrate into the REBCO layers. The superconducting behaviour is utterly dependent on the grain directions, so epitaxial growth is required. The initial texture for epitaxial growth is either formed within the metallic substrate by the rolling-assisted, biaxial textured growth (RABiTS) method, or, in the initial buffer layers by using an ion-beam-assisted deposition technique. After this, a thin layer of silver is added to the REBCO layer to protect it against environmental degradation and to enhance the electrical contact. Finally, copper is applied over the silver layer to enable current transfer and stabilize the superconductor.

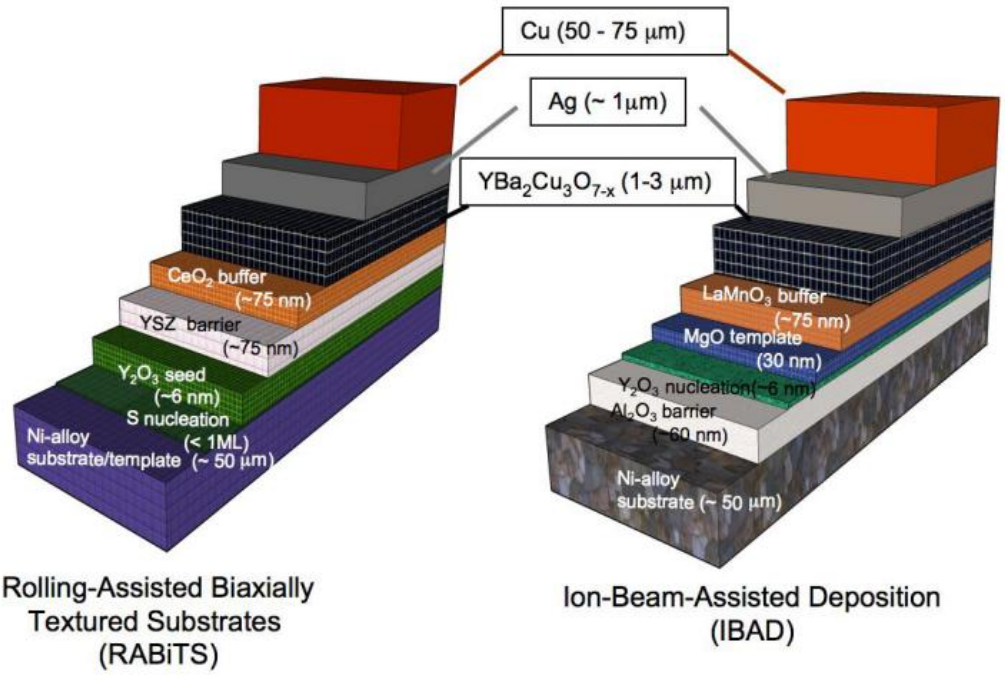

Figure 2-7 The configuration of 2G coated conductors constructed using two techniques. The left is produced using RABiTS by American Superconductor, and the right using IBAD, by SuperPower [27]

2.2 Modelling methods

Since the fabrication technologies have achieved great successes so far, electrical and manget engineering have been focusing on the application of these superconducting materials. Both analytical and numerical models have been developed during the past two decades for designing superconducting devices. Analytical methods employ relatively simple formulas and calculate the magnetic field for simple geometries. They are fast methods that offer us the opportunity to understand the basic mechanism of electromagnetic behaviour. However, there are some limitations, such as the constraints on the simple geometry and tape configuration. On the other hand, numerical methods are more flexible and powerful.

From the mathematical point of view, there are two existing numerical schools in solving engineering continuum problems. The first method is the field approach, which involves the solution of partial differential equations (PDE) using element approximation. The second approach is denoted as the source distribution technique, which makes use of Green's function and seeks the field directly by integration of trying source distribution. This thesis refers to these two approaches as the differential method and the integral method, respectively. In other references they sometimes are referred to as the partial differential equation (PDE) and integral equation (IE) methods.

As noted in the previous section, the most obvious feature of a superconductor is the Meissner Effect under a magnetic field, due to the induced surface current. The induced current generates a magnetic field opposing the external field, and thus reduces the magnetic flux density inside the superconductor to zero. The most difficult part of the model is to determine the current distribution by the self field or external field. Both the differential method and the integral method try to numerically calculate the current distribution. The following section presents a short review of current distribution simulation methods: the analytical method, differential and integral methods.

2.2.1 Analytical method

Norris [28] first summarized the AC loss calculation using complex variable analysis of simple geometries in 1970. He derived the AC loss calculation equations for a single tape with the cross-sectional geometries of rectangle, circle and ellipse. His results employed the original Bean model, assuming the critical current density to be constant.

These results were widely used as benchmark examples for modern experimental and simulation results. According to Norris's calculation, the AC loss for a single rectangle tape is:

$$Q = \mu_0 I_c^{\,2} L_n \qquad \text{Equation 2-3}$$

where L_n is the loss factor, a parameter related to the carrying current, which can be found in a table in the original paper.

Brandt [29] later extended Norris's calculation for a single tape with a large width/thickness ratio. Brandt also proposed a method to calculate the current distribution during the process of current changing. According to Brandt's paper the AC loss in single tape is [30]:

$$Q = \frac{\mu_0 I_{\max}^{\,2}}{\pi} f_n\left(\frac{I_0}{I_{\max}}\right) \qquad \text{Equation 2-4}$$

$$f_n(x) = (1-x)\ln(1-x) + (1+x)\ln(1+x) - x^2 \qquad \text{Equation 2-5}$$

2.2.2 Differential methods

The basic idea of the differential method relies on Ampere's law, which relates the magnetic field to the current source. Since the finite element method (FEM) is a powerful tool for solving PDEs, it is natural to use the FEM with Ampere's law to calculate current distributions. We can transform the Maxwell's equation into different formats to satisfy FEM implementation. There are some differences in choosing different formats of PDEs and the selection of format results in three formulas: *A-V* formula [31], *T-Ω* formula [32] and *H*-formula [33]. The name of each formula is based on the variables solved by the formula. Grilli summarized different formulations commonly used to solve the Maxwell equations with numerical models [34]. To use all differential methods, it is necessary to predefine the resistance and to set the boundary conditions and initial values. Superconductivity is described by the *E-J* law, as shown in Figure 2-2. The smooth current-voltage characteristic is especially preferable for FEM simulation. From the *E-J* law, we can easily determine the resistance of the material as:

$$\rho = \frac{E_c}{J_c}\left(\frac{J}{J_c}\right)^{n-1} \qquad \text{Equation 2-6}$$

Normally, this resistance is measured by current-voltage experiments and applied to the FEM analysis. For most differential problems the boundary conditions are infinitely far away, hence the simulation volume is much larger than the superconducting regions.

The *A-V* formula is widely used and highly developed method for conventional materials, and it can also be applied to superconductors [35].

The control equation of *A-V* formula is:

$$\nabla \times \left(-\frac{1}{\mu_0} \nabla \times A \right) = \frac{1}{\rho} \left(-\frac{dA}{dt} - \nabla V \right) \qquad \text{Equation 2-7}$$

where A and V are state variables, standing for the magnetic vector potential and electrostatic potential, respectively. V is a scalar field related to the electric field, E. It can be interpreted as the potential due to electrostatic charges. In many cases the electrostatic potential V is ignored. Hauser developed a special element, and first modelled the force and the displacement in superconducting bearing using the commercial FEM code, ANSYS [36].

The control equation can also be formulated using the current vector potential, T, and the scalar magnetic potential, Ω, in an equation very similar to the *A-V* formula. The current vector potential, T, and scalar magnetic potential, Ω, are defined as:

$$\nabla \times T = J \qquad \text{Equation 2-8}$$

$$H = T - \nabla \Omega \qquad \text{Equation 2-9}$$

where Ω is calculated analogous to the way that static charges determine V in the *A-V* formulation. The control PDE of *T-Ω* formula from the Maxwell equations can be obtained using:

$$\nabla \times \left(\rho \nabla \times T \right) = -\mu_0 \left(\frac{dT}{dt} - \nabla \left(\frac{d\Omega}{dt} \right) \right) \qquad \text{Equation 2-10}$$

Amemiya raised the *T-Ω* formula with the normal node element in a superconductor in 1998 and used it for different boundaries and geometries [32]. Stenvall presented the vector potential eddy current formulation for solving the hysteresis losses of superconductors using the finite element method [37, 38]. He incorporated edge element in this method and compared the results to the existing analytical method, obtaining good agreement.

The latest established formula was the *H*-formulation, which was first reported in 2006 and was used by many research groups worldwide. Compared to the other differential methods, the *H* formulation has advantages of using the fewest variables, easily setting boundary conditions and avoidance of unstable calculations. Another obvious advantage is that it can be applied using commercial software, which frees us from complicated and tedious programming.

According to Faraday's Law:

$$\nabla \times E = -\mu \frac{dH}{dt} \qquad \text{Equation 2-11}$$

Since *H* has H_x and H_y two components in 2D geometry:

$$\begin{bmatrix} \frac{\partial E_z}{\partial y} \\ -\frac{\partial E_z}{\partial x} \end{bmatrix} = -\mu \begin{bmatrix} \frac{dH_x}{dt} \\ \frac{dH_y}{dt} \end{bmatrix} \qquad \text{Equation 2-12}$$

Inserting *E-J* law into the above equation:

$$\begin{bmatrix} \frac{\partial \left(E_c \left(\frac{J}{J_c} \right)^n \right)}{\partial y} \\ -\frac{\partial \left(E_c \left(\frac{J}{J_c} \right)^n \right)}{\partial x} \end{bmatrix} = -\mu \begin{bmatrix} \frac{dH_x}{dt} \\ \frac{dH_y}{dt} \end{bmatrix} \qquad \text{Equation 2-13}$$

Ignoring the displacement current for quasi-approximation problems, Ampere's law gives:

$$J = \frac{\partial H_y}{\partial x} - \frac{\partial H_x}{\partial y} \qquad \text{Equation 2-14}$$

Thus, the control *H*-formula yields:

$$\begin{bmatrix} \dfrac{\partial\left(E_c\left(\dfrac{\frac{\partial H_y}{\partial x}-\frac{\partial H_x}{\partial y}}{J_c}\right)^n\right)}{\partial y} \\ -\dfrac{\partial\left(E_c\left(\dfrac{\frac{\partial H_y}{\partial x}-\frac{\partial H_x}{\partial y}}{J_c}\right)^n\right)}{\partial x} \end{bmatrix} = -\mu \begin{bmatrix} \dfrac{dH_x}{dt} \\ \dfrac{dH_y}{dt} \end{bmatrix} \qquad \text{Equation 2-15}$$

This equation can be represented by the general PDE form:

$$\nabla \times (\rho \nabla \times H) + \mu \frac{dH}{dt} = 0 \qquad \text{Equation 2-16}$$

Hong implemented this approach in COMSOL and applied it to magnetisation simulation with impressive results [33]. His work provided a new way to carry out numerical modelling with the COMSOL commercial software. Grilli employed this approach in AC loss calculation first and compared it to experimental results, which verified the model [39]. Zhang further extended this model to complicated materials and geometries with experimental results [40, 41]. The *H*-formula employs the magnetic field variable *H* as a state parameter directly, so it is especially efficient to incorporate the Kim model.

Although differential methods are hugely successful at simulating current distribution, there are some natural drawbacks to hinder them from future device-scale simulations. The YBCO layer has a thickness of 1 μm and the tape has a width/thickness ratio of greater than 4000. Additionally there is a drastic change in current density, which requires very fine meshes to gain an accurate current distribution. At the same time, differential methods require boundary setting which further increases the complexity of the meshes. What's more, the superconductor model is highly non-linear which significantly increases the calculation time. This is impractical when applied to a real engineering device simulation, where hundreds of tapes are wound together to generate the expected magnetic field. The emergence of integral methods offers a promising method for simulating current distribution since they overcome these limitations by the incorporation of reasonable assumptions.

2.2.3 Integral methods

With the development of differential FEM methods in the last century, integral equation methods have also drawn considerable attention. The choice of integral methods is made to avoid the use of global meshes and also to avoid the need to specify external boundary conditions. The integral method was first employed in magnet design, and was later extended to assess the effects of eddy currents in the design of both accelerator and Tokamak magnets [42].

The basic idea of superconductor modelling is minimization of the magnetic energy in the superconducting region. In this approach, trying current distribution is specified in the whole superconducting area. The whole energy can then be obtained using integrated parameters, such as the magnetic flux density, B, or magnetic vector potential, A. With the help of mathematical optimization algorithms, we can find the optimal current distributions.

Clem proposed an numerical method to estimate the AC losses of a stack of infinateYBCO tapes based on integral equations [43]. According to the previous results, he also assumed that the tape is homogenous, carrying the same net current, and that the critical current penetration in the superconductor is a line vertical to the width direction. The second assumption is that each tape has a constant penetration depth. These two assumptions built the foundations for trying current selection. From the Green theorem, the vector potential, A, and magnetic flux density, B, can be derived respectively:

$$A(r) = \frac{1}{2\pi}\int_S J \cdot \log(r - r')dr' \qquad \text{Equation 2-17}$$

$$B(r) = \frac{\mu_0}{4\pi}\int_S \frac{Idl \times r'}{r^3} \qquad \text{Equation 2-18}$$

Based on Clem's idea of the line front track assumption, Yuan raised a new model by replacing the frontier with a quadratic function [44, 45]. This model minimised the total perpendicular B square in the subcritical region. In Yuan's model the same homogenous approximation was applied, but allowing for a magnetic field dependence on the critical current density. Further extension was made to the cylindrical geometry for coils with a small inner radius. Yuan verified his model with experimental results.

Pardo and Gormory proposed a minimum magnetic energy variation (MMEV) which minimizes the functional in the J formulation and constrains the current in each tape. The energy was calculated by $A \cdot J$ across the superconducting area [46, 47]. All current distributions with discrete values below the critical current density were calculated, and the current with the least energy was chosen as the stable state. The current distribution and AC losses were compared to analytical and experimental results.

Prigozhin created the variational method to investigate the current distribution of a bulk superconductor in the mid 1990s [48]. Since the thickness of the YBCO layer is so small, usually 1 μm, it was natural to consider it as a sheet. In 2011, he extended his model to coated conductors, and this new model was called the sheet current model [49]. Based on the current density distribution, an inequality was drawn from Bean's model. After some transformation and variational processes, this problem became a quadratic optimisation problem and the optimal current distribution denoted for the minimised energy state. The MMEV and the sheet current model share the same energy formation and can yield the same current distribution.

All integral methods have the virtue of fast calculation. This efficiency comes from two aspects. The first reason is that the critical current state avoids nonlinear iterations, which appear in differential methods due to the E-J power law. The second reason is the avoidance of global mesh generation. In the integral method, only the values at the points of interest are calculated, particularly in large aspect ratio tapes, rather than the whole area as in FEM methods. Both these reasons make integral methods attractive for future simulations, especially in superconducting devices based on YBCO tapes.

2.3 AC loss

2.3.1 AC loss mechanism and classification

When superconductors are exposed to an AC electromagnetic field, energy is dissipated, which is referred as the AC loss. From a macroscopic perspective, AC loss results from the induced electric field by the transporting AC current or the time-varying external magnetic field. From a microscopic perspective, AC loss is the energy dissipation during the movement of the depinned flux lines.

AC loss can be classified into two groups: magnetisation loss and transporting loss. The superconductor can be magnetized by an external magnetic field and, similar to ferrous materials, the magnetisation *B*-*H* curve can be plotted during the magnetisation process. Thus, the magnetisation loss can be calculated by integrating *BH* across the close *B*-*H* curve. The transporting loss is the dissipated energy when the superconductor is carrying an AC current. Both losses should be considered when the superconductor is transporting AC current in an external time-varying magnetic field.

From the aspects of physical mechanisms, AC loss can be divided into three types: hysteresis loss, eddy loss and coupling loss. Hysteresis loss is caused by the movement of the penetrated magnetic flux in the superconductors under AC conditions. Eddy loss is generated by the induced circulating currents in the normal metal parts of the superconductors. Coupling loss is caused by the currents coupling two or more superconducting filaments via the normal metal regions separating them. Under power frequency, the major part of AC losses is due to hysteresis loss [50].

2.3.2 Measurement techniques

There are two ways to measure AC losses in a superconductor: the calorimetric method and the electrical method.

A calorimetric method to measure AC losses in superconducting tapes was introduced in [51, 52]. Figure 2-8 presents the measurement system. This method is based on the idea that the AC loss produces heat, which boils a corresponding amount of liquid nitrogen. Thus, the AC loss in the coil can by measured through the gas evolution rate in the boil-off chamber. This technique is relatively easy to set up, however, it has limitations in terms of sensitivity and the need for expensive experimental equipment.

The second method to measure AC losses in superconductors is the electrical method [53]. Figure 2-9 gives an example circuit. The superconducting device is connected to an AC current using a power amplifier controlled by a function generator. Thus, a suitable AC current supply is introduced to the system. A compensation coil is used to eliminate the inductive part of the voltage so that only the in-phase resistive component remains. A lock-in amplifier is used to detect voltage signals in-phase with

the operating current. The resistive part in the sample can thus be collected and the AC losses can be calculated. The AC loss per unit length per cycle (the unit of AC loss) is:

$$Q = \frac{I_{rms} V_{rms}}{f} \qquad \text{Equation 2-19}$$

The first difference between the electrical method and the calorimetric method is that the electrical method can only measure the transporting losses, however the calorimetric method can measure both the transporting losses and magnetisation losses. However, the electrical method is less time consuming than the calorimetric method, in terms of efficiency.

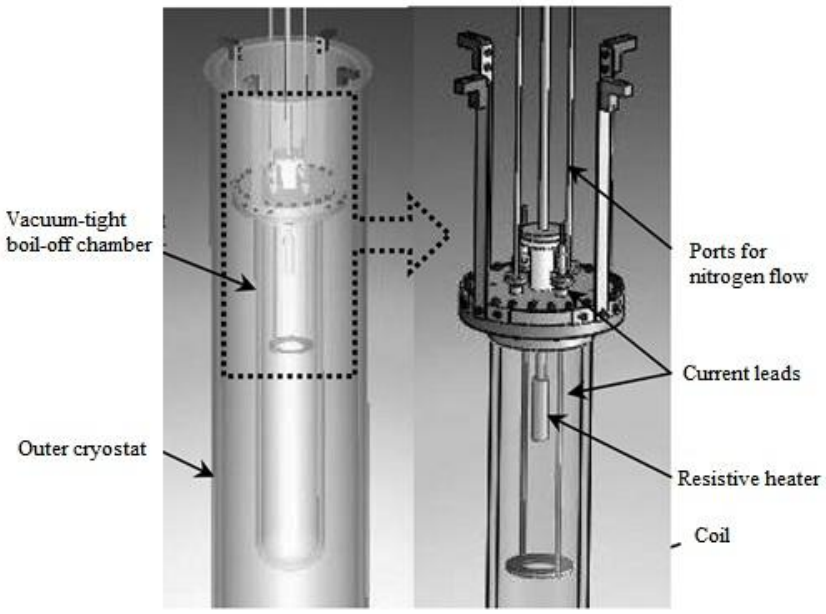

Figure 2-8 Schematic of the experimental apparatus used for AC loss measurements in superconducting pancake coils using the calorimetric liquid nitrogen boil-off technique [54]

2.3.3 AC loss calculation methods

Like Joule heating, AC loss can be calculated by:

$$q = E \cdot J \qquad \text{Equation 2-20}$$

where q is the heat density with units of W/m^3. As we have seen, J can be directly derived by the methods presented in sections 2.2.1 and 2.2.2. The problem is how to calculate the electric field E.

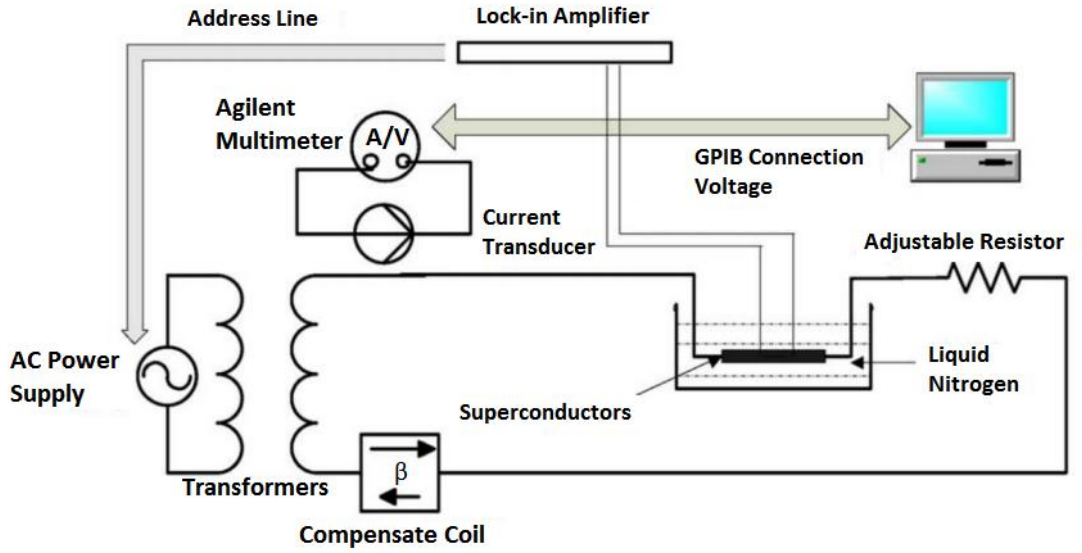

Figure 2-9 AC loss measurement system using the electrical method

For the H formula, E can easily be found using the E-J law, while for the integral method, careful derivations should be performed. As we have pointed out in last section:

$$E = -\frac{dA}{dt} - \nabla V \qquad \text{Equation 2-21}$$

where ∇V is the gauge of the potential. According to the Bean model assumption, the electric field in subcritical region is equal to 0. Thus in the subcritical region:

$$\nabla V = -\frac{dA_{subcritical}}{dt} \qquad \text{Equation 2-22}$$

Since ∇V remains constant across the section, the electric field in the section can be expressed:

$$E = -\frac{dA}{dt} - \frac{dA_{subcritical}}{dt} \qquad \text{Equation 2-23}$$

The total AC loss of the section can be integrated across the section:

$$Q = \int_T \int_S E \cdot J dx dy dt \qquad \text{Equation 2-24}$$

2.4 Thermal and mechanical modelling

After establishing the current distribution calculation, multiphysics modelling is required to simulate the thermal and mechanical fields within the system. There are several reasons for the implementation of thermal and mechanical field modelling.

For thermal modelling, quench simulation is a priority task of superconducting coil design and is closely related to the safe operation of the coils. Once the quench is triggered under the time-varying magnetic fields, the current decaying process, temperature distribution and voltage between the terminals are key issues for magnet stability. All these processes can be simulated and visualized with the help of thermal coupled simulations. Another reason for using thermal simulation is to design the cryogenic system. The selection of the cryocooler and the configuration of the coldhead can be optimized using the results of the temperature distribution simulation.

High current in the superconducting tapes coupled with high magnetic field may result in an enormous Lorentz force, which may destroy the whole system. Thus, mechanical stability requires the accurate simulation of stress and strain distributions. Secondly, most superconductors are wound into coils, or pancakes, to function as magnets, and many experiments have shown that the winding process degrades the critical current of the tapes [55]. Understanding the mechanical stress distribution helps us to avoid degradation and to optimize the coil design.

Park presented the optical configuration of a 600 kJ SMES acquired by Auto Tuning Niching Genetic Algorithm [56]. Electromagnetic fields and stresses were then calculated by FEM for different operating currents. The stresses (radial and hoop stress) imposed on the designed HTS magnets were calculated by the program, and the results of the stress analysis were discussed. The results showed that the hoop stress was the main concern in SMES design. In this research the superconductors were considered to be normal conductors, and this simplification sometimes was not appropriate

Zhang performed an experimental and numerical study of a YBCO pancake coil with a magnetic substrate in COMSOL [40, 41]. The influence of the magnetic substrate under AC and DC conditions was studied. It was observed that when the applied DC current approaches the critical current, the coil loss profile changed completely in the magnetic substrates due to the change in the magnetic field distribution.

In summary, up to now papers about multiphysics solutions for superconducting coils using HTS are very limited, and the model is not fully developed. Some papers have focused on thermal fielded calculations of several tapes, such as quench propagation and the minimal energy zone. Other papers have studied the mechanical field simulation

using the homogenous material model. Few work involves the complete multiphysics modelling in superconducting coils.

2.5 Superconducting energy storage

2.5.1 Structure and application

Efficient and reliable electric energy storage technologies have become more and more important in the past few decades [57]. SMES has many advantages and shows the potential for further application [58]. It is well accepted that SMES devices have large roundtrip efficiency and large power density. Furthermore, SMES has a long calendar life, long lifecycle and rapid response to power demands. Therefore, from a technical sense, SMES is an ideal storage system for electrical utilities.

SMES stores energy in the form of persistent current in superconducting coils and exchanges the energy between the coils and the grid when necessary. Since no energy conversion takes place during the charging and discharging process, the efficiency is extremely high and the response time is very short. SMES system consists of four parts: the superconducting magnetic coils, the power conditioning system (PCS), the cooling system and the control system, as presented in Figure 2-10 [59].

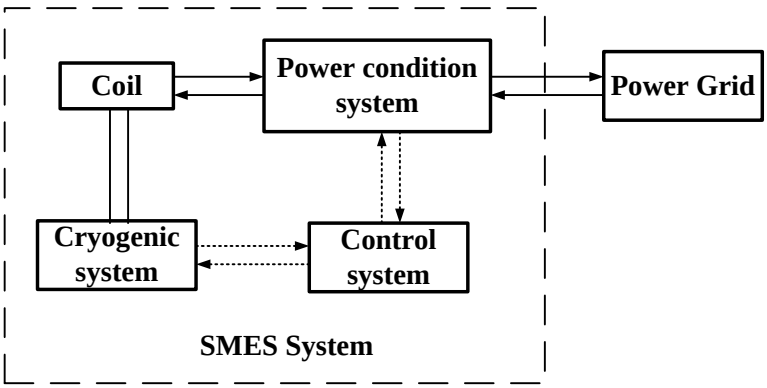

Figure 2-10 SMES system has four parts: superconducting coil, power conditioning system (PCS), cryogenic system and control system. It connects to the power grid through PCS.

Superconducting magnets are the key part of SMES systems. In a 2G HTS SMES, the magnet is assembled from pancake coils. The major part of the power conditioning system is an AC/DC converter, which transfers energy from the superconducting magnets bi-directionaly. While the cooling system plays the role to sustain the required

cryogenic environment for superconductivity. The control system regulates both the PCS and cryogenic system. For instance, if the transporting current exceeds the critical current, which may cause a quench, the control system may increase the cooling power and trigger the quench protection.

SMES systems offer significant benefits to power systems. These applications can be classified into three aspects: system stability enhancement and power quality improvement.

Modern power systems have obvious limitations in terms of stability and security, because they lack sufficient components that can absorb and release energy quickly [60]. The stability of a power system relies on the inertial energy storage of the generators, relay protection and other automatic devices, which act as passive protection. As an active power source, SMES can be used to eliminate the lower frequency oscillation of an interconnected power grid, and to migrate sub synchronous resonance (SSR) and sub synchronous oscillation (SSO). As a reactive power source, SMES can also provide the necessary voltage support for a transmission line, particularly for the end loads. Figure 2-11 shows that SMES can provide both active and reactive power to the grid.

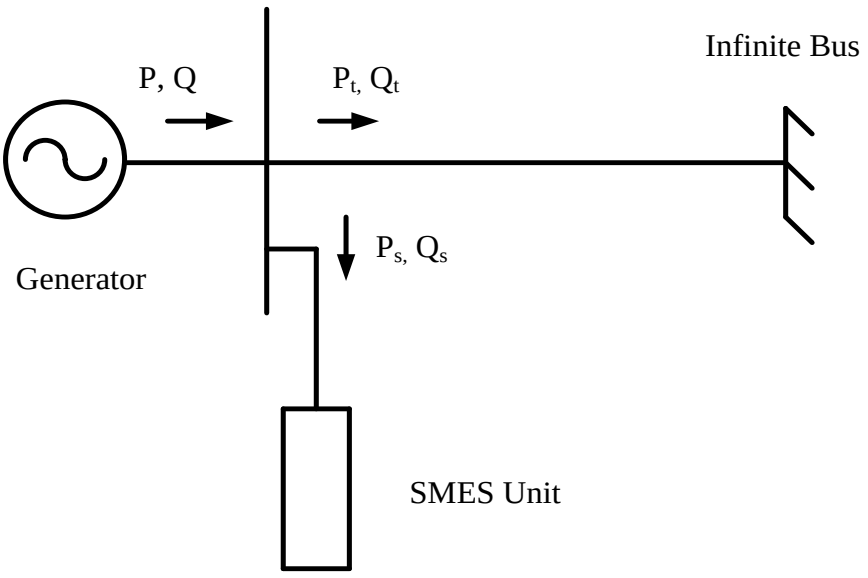

Figure 2-11 SMES unit connected to generator providing both active and reactive power. Active power is denoted by P and reactive power is noted by Q

In order to improve power quality, SMES can be used as an energy storage system for a flexible AC transmission system (FACTS) devices [59]. A static synchronous compensator (StatCom) is one of the core units and core technologies in a FACTS. Its major role is to compensate the reactive power, maintain the voltage between joint points, and to improve the steady-state and dynamic performance of the system. The active power from SMES enables the StatCom to absorb and inject active and reactive power simultaneously, and thereby offers additional benefits and improvements.

2.5.2 SMES history

The concept of SMES was suggested in France in 1969 to level the diurnal power demand in a utility grid [5]. The basic process was to charge the superconducting magnet during the off-peak time and to release the energy during the peak time. Feasibility studies were conducted in the 1970s to consider large scale SMES as a replacement for pumped hydro [9, 61]. The technical feasibility of large scale SMES for load levelling was demonstrated, but the cryogenic system for LTS SMES was too expensive and the cooling down process usually took a long time, making it very impractical.

Los Alamos and Bonneville Power Administration proposed a different application for SMES in 1976. They aimed to stabilize a power grid using a 30 MJ/10 MW superconducting magnet. Following this project, Japan and US conducted some other projects. To the end of the 1980s, research efforts and business development were started on medium and small scale SMES devices, such as compensation of load fluctuation for factories and military application. These efforts verified the effectiveness of the SMES systems at several sites.

Since the discovery of HTS in 1987, intensive research has been conducted to design and build HTS SMES. The advantage of HTS SMES is the operating temperature above that of liquid helium, which simplifies the cryogenic system and lowers the construction cost. Another advantage is that at 20 K and a field above 10 T the critical current density of HTS is much higher than that of LTS. At the same time, the mechanical strength of HTS is greater than those of LTS wires, since they are enhanced by the alloyed substrate materials. As a result, a compact coil with a high field operated at 20 K can be made using HTS [59].

As early as 1993, a conceptual design of HTS SMES was proposed in the U.S. A Bismuth-based superconductor – BSCCO – was used in the design, and the energy stored ranged from 7.2 GJ to 720 GJ [62]. This paper analysed feasible configurations for the critical current density, cost, magnetic field and strain distribution, which were the key consideration for the SMES design. It concluded that, for practical applications, the critical current should be improved, the prices of conductors should be lowered, higher field operation was required, strength should be enhanced, and AC loss needed to be reduced. These conclusions are still viable today.

The first successfully constructed HTS SMES was reported in 1997 by Kalsi [6]. It was a 5 kJ SMES, consisting of a BSCCO-2223 solenoid coil and operating at a temperature of 25 K. This system was designed and built by American Superconductor, which was shipped to Germany to be tested in a scaled grid. The success of this HTS SMES proved the feasibility of using HTS SMES in commercial products. Combined with the commercialisation of BSCCO conductors, this success was followed by many HTS SMES projects around the world, capable of holding energy from the small scale (kJ) to the medium scale (MJ).

Friedman A. and his colleagues designed two SMES systems using BSCCO tapes operating in liquid nitrogen [63]. The second device stored 1.2 kJ and could release 20 kW during the discharging process. The superconducting coils had ferromagnetic cores to enhance the energy density. Using liquid nitrogen in the cooling method offered a good thermal contact between the coolant and the device, thus providing good thermal stability and homogeneity. These projects proved the power conditioning capability of HTS SMES systems, and successfully demonstrated compensation for voltage drops in the electric grid.

The University of Wollongong in Australia constructed a nominally 2.5 kJ prototype HTS SMES using BSCCO 2223 tape, and further work led to a 20 kJ HTS SMES device [8, 64]. This prototype was cooled to 20 K with a gaseous helium cold head cryocooler. The control electronics enabled the coil to discharge energy to a 3-phase AC load to compensate for the voltage sag.

Grenoble University in France funded a project to design and construct a 800 kJ SMES with the rated current of 135A [65, 66]. Nexans conductors, made of Bi-2212 PIT tapes, were used to wind the coils and the coils were soldered in parallel. 26

superposed simple pancakes were wound and bonded with epoxy to sliced copper plates. Cryocoolers were applied to make the cryogenics very friendly and invisible for the SMES users. This project demonstrated the feasibility of industrial SMES application.

Table 2-1 Selected SMES projects with the year developed, stored energy and design purpose

Country	Developer and Year	Material	Energy	Application
U. S.	LANL, 1979	NbTi	30 MJ	Frequency regulation
	University of Florida, 2003	NbTi	100 MJ	Frequency regulation
	AMSC, 2010	NbTi	1–5 MJ	Commercialized
Japan	NIFS, 2006	NbTi	1 MJ	UPS
	Chubu Electric, 2009	NbTi	20 MJ	Voltage sag compensation
	Chubu Electric, 2004	BSCCO	1 MJ	Voltage sag compensation
	Toshiba, 2006	BSCCO, NbTi	6.5 MJ	Laboratory demonstration
Korea	KERI, 2006	NbTi	3 MJ	UPS
	KERI, 2010	BSCCO	2.5 MJ	Grid stability
France	CNRS, 2008	BSCCO	800 kJ	-
Italy	University of Bologna, 2008	NbTi	200 kJ	Enhance power quality
Germany	ACCEL Instruments GmbH, 2003	BSCCO	150kJ	UPS
Australia	University of Wollongong, 2005	BSCCO	2.48kJ	Voltage sag compensation
China	Tsinghua University, 2007	NbTi	300kJ	Voltage sag compensation
	CAS, 2010	BSCCO	2MJ	Enhance power quality
	HUST, 2005	BSCCO	35kJ	Hydro station
Poland	ASL	BSCCO	34.8kJ	UPS

2.5.3 Comparison of SMES with other technologies

Generally speaking, there are four types of energy storage systems that handle the intermittency and uncertainty of renewable energy generators: battery, supercapacitor, flywheel and SMES [67]. However, as shown in Figure 2-12, all energy storage elements cannot simultaneously satisfy both the desired characteristics of high power density and high energy density.

Battery is the most widely used energy storage device [68]. It has considerably high energy densities and it is suitable to support a microgrid. However, it can't release the required energy quickly and their total charging and discharging cycles are quite small.

Flywheel stores energy in the form of the angular momentum with a spinning rotor. Kinetic energy from the flywheel can be transferred into AC power through the use of controls and power conversion systems [69]. The energy of flywheels can be charged and discharged very quickly, with specifically designed electronic interfaces, meaning the power density is high [70]. However, there is a large standby loss due to the mechanical bearing friction, also the energy transformation from mechanical to electrical process can also decrease the efficiency.

Supercapacitors and SMES store energy in electromagnetic fields, absorbing and releasing energy controlled by electronic inverters [71]. Supercapacitors store energy through the separation of electrical charge. They achieve very high capacitance and energy capacity through a high surface area and small charge separation distance. Since there are no chemical variations on the electrodes, supercapacitors have a high power density, high efficiency and a long lifecycle.

SMES systems run persistent current through closed superconducting coils so that magnetic energy can be charged and discharged [72, 73]. Their response time ranges from several milliseconds to several seconds, with an efficiency of greater than 95%. SMES systems have significantly higher power densities and module power ratings, compared to flywheels and supercapacitors. In addition, they have advantages such as solid-state operation and high round-trip efficiencies. Therefore SMES are able to improve the performance of renewable energy system significantly.

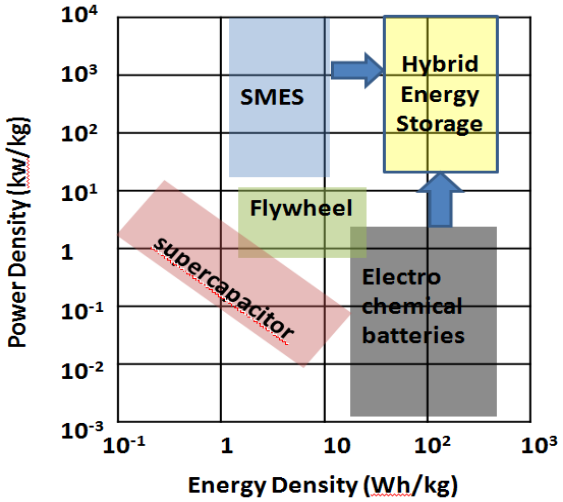

Figure 2-12 Ragone Chart of energy storage systems [74].

2.6 Summary

This chapter reviews the relevant background of the superconducting materials and its application in SMES system. We first introduce the basic properties and theories, focusing on their macro aspects. Special attention is paid to the diamagnetism and *E-J* power law in Type II superconductor. This is followed by the tools for simulating superconductors. The control equations in different methods are described and explained in details. We also compare the different approaches to calculate the AC loss. In addition to the electromagnetism simulation, the previous work on thermal and mechanical simulation are also summarized. In the end, SMES system is introduced from the configuration, application in power system and existed projects.

Chapter 3. Superconducting Tape under Magnetic Field and Impregnation

The ability to maintain a high current-carrying capability is the most important attribute of superconductors, which can be characterized by the critical current. Since the material and configuration are different from conventional LTS and 1G HTS, 2G coated conductors show quite different critical current characteristics. For example, contrary to LTS, the *E-I* curve of a 2G coated conductor is considerably smoother during the superconductor/non-superconductor transition. The columnar structure of a coated conductor and the weak link within the grain boundaries result in high anisotropy and easy degradation, which makes device design complex and challenging. Accordingly, further research into the critical current of 2G HTS conductors is very important, not only for practical applications, but also for understanding the underlying physics.

The external magnetic field is one of the factors that influence the critical current density and cause anisotropy. Although the microscopic image of high temperature superconductivity is unclear at the moment, it is well accepted that the lossless current is related to the current vortex pinned by microscopic defects. The presence of an external field makes the flux flow easily, thus decreasing the critical current. At the same time, the critical current varies when the external field is in a different direction, which is named as anisotropy. As all superconducting devices operate under magnetic fields, whether a self field or an external field, it is of vital importance to understand and quantify the influence of the external magnetic field.

Impregnation with epoxy resin is a necessary process for most superconducting components. Firstly, the impregnated conductor has better mechanical strength [75, 76], which can resist the Lorentz force and keep the superconducting unit stable. Another reason for impregnation is to improve the thermal conductivity [77]. More and more

superconducting components are cooled by cryocoolers. Insufficient thermal conductivity causes a temperature gradient and limits the performance of superconducting components. Filling the void of the superconducting unit can enhance the thermal stability. However, the impregnation process can also bring about degradation to the critical current of the superconductor. This degradation results from the thermal mismatch between the superconducting tape and the resins during the cooling process. In order to control the degradation, careful selection of the impregnation material requires further investigation.

This chapter is dedicated to analysis of the influences of the external magnetic field and different impregnation materials on 2G HTS short samples, in order to pave the way for further application in energy storage design. The chapter is organized as follows. Section 3.1 introduces some concepts related to theoretical modelling. Section 3.2 explains the experimental instrumentation system used to measure the critical current of the superconducting short samples. Section 3.3 continues to measure and discuss the influence of an external DC magnetic field on the critical current and the *n* value. In section 3.4, experiments are performed to study the effectiveness of the impregnation process.

3.1 Theoretical model of tape

3.1.1 Flux pinning and critical current

The critical current of superconductors in most technical applications is largely determined by the properties of the superconducting vortices. These vortices are formed as tubular structures when a type II superconductor is exposed to a magnetic field, as shown in Figure 3-1. Each vortex is surrounded by encircling supercurrent and carries certain magnetic flux, or flux quanta, which acts as small solenoid magnets.

Transporting current through the superconductor under an external magnetic field (for example, the superconducting winding in an electric motor) induces a Lorentz force, F_L, on the vortices, which can be calculated by:

$$F_L = J \times \Phi_0 \qquad \text{Equation 3-1}$$

where J is the applied current density and Φ_0 is the magnetic flux carried by each vortex.

When superconductors contain normal inclusions due to structural defects, vortices can be struck by these "defected" sites, thereby preventing the movement of the vortices. This phenomenon in Type II superconductors, called flux pinning, forms the foundation for all technical superconductors. These vortices experience an attractive force, F_p. When the applied current is large enough that $F_L > F_p$, the vortices move away from the pinning sites. A moving vortex induces a resistance which dissipates energy named as AC loss.

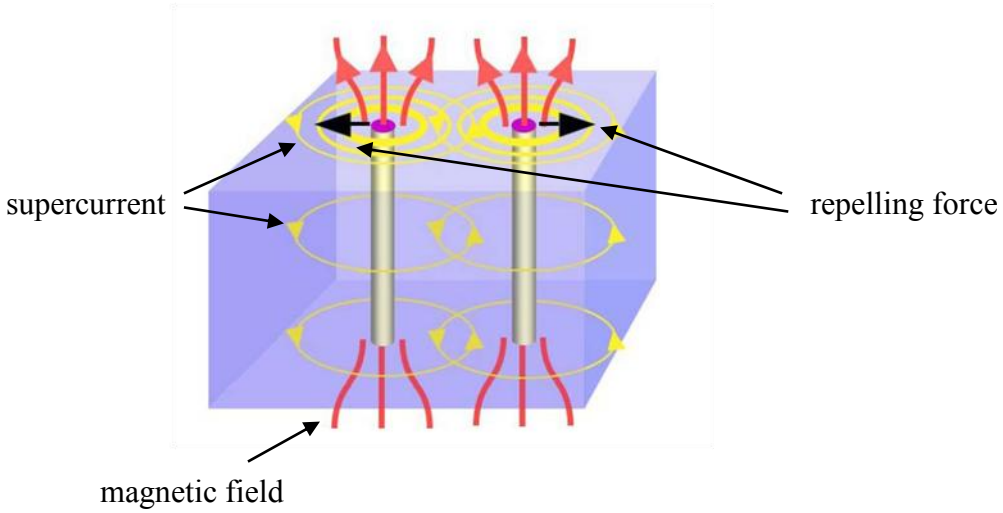

Figure 3-1 Schematic view for two parallel vortices with the presence of an external magnetic field. When two vortices come close to one another, they repel each other.

The current density at which $F_L = F_p$ is the critical current density, J_c, which can be defined as:

$$J_c = \frac{F_p}{B} \qquad \text{Equation 3-2}$$

where F_p denotes the pinning force and B is the applied magnetic field.

Generally, J_c decreases with increasing temperature and magnetic field, and reaches zero when the temperature and magnetic field exceed the critical values. Beyond the critical temperature and critical magnetic field, the superconductor loses its ability to transport loss-free current.

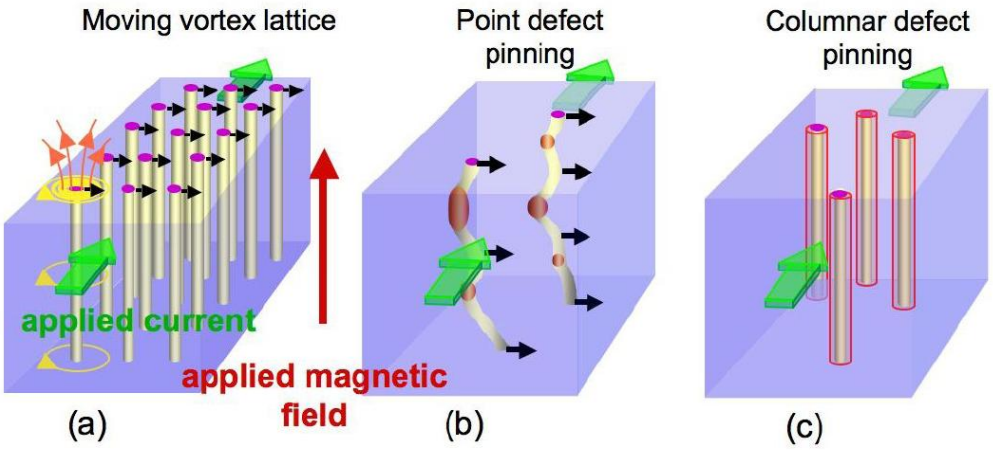

Figure 3-2 (a) Schematic of fluxes moving under a Lorentz force (black arrow) induced by an applied current (green arrow) and an applied magnetic field (red arrow) in a defect-free superconductor; (b) Sections of fluxes pinned by point defects (including oxygen vacancies, precipitates, dislocations or defects induced by irradiation). (c) Entire sections of fluxes are pinned by line defects, such as amorphous columnar tracks induced by high-energy heavy ion irradiation [78].

High temperature superconductors contain a high concentration of natural pinning sites, such as oxygen vacancies, as shown in Figure 3-2(b). To improve the electrical properties of superconductors, one can also manufacture pinning centres artificially, optimizing their shape, size and arrangement. Linear defects, such as columnar defects as shown in Figure 3-2(c), produced by irradiating superconductors with high energy ions and dislocations, have proven to be among the most efficient pinning centres. Columnar defects are more effective in pinning vortices than randomly placed point defects, as they can be geometrically matched to the vortices. However, engineering the pinning sites to match with each superconducting vortex is still an ongoing question being addressed through recent advances in nanotechnology.

3.1.2 The *E-I* relation, critical current and *n*-value

The *V-I* relationship is more commonly used to characterize superconductivity from an engineering perspective. The voltage can be measured by applying a certain current to the superconductor. Figure 3-3 presents a typical *V-I* curve. If the voltage is divided by the distance between the voltage taps, this curve can be easily transformed to the more well-known *E-I* curve.

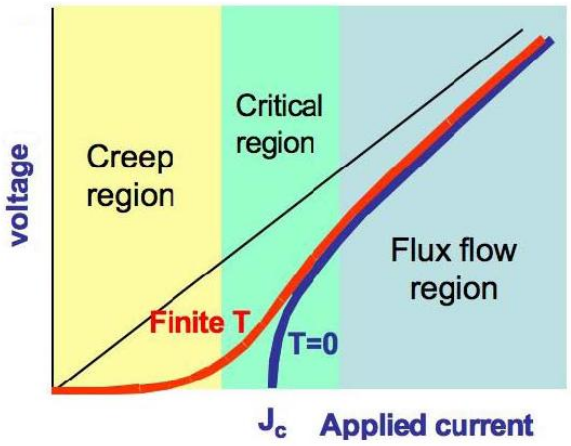

Figure 3-3 Typical curve of *V-I* measurement. Because of flux creep, there is finite resistance even at a current well below J_c at a finite temperature, in contrast to T=0.

There are three different parts to the *V-I* curve: a creep region in the low current range, a flux flow region in the high current range and a critical region bridging the two. The critical current of the superconductor is defined by a certain voltage drop, normally 1 $\mu V/cm$ in the critical region.

This curve can be explained from the view of flux pinning. In the creep region, after applying a finite current to the superconductor there is a finite resistance even at low temperatures. This is because thermal fluctuations can promote vortex jumps between neighbouring pinning sites in a process known as flux creep. Flux creep is enhanced by the fact that the pinning sites are randomly distributed. When the current is further increased to close to the critical current, the voltage enters the transition region. If the current is further increased and the Lorentz force becomes stronger than the pinning force, the flux flow stage begins and the pinning effect no longer works so that the flux flow regime becomes dominated by the Lorentz force [79].

Typical *E-I* curves have a highly non-linear transition process from the flux creep region to the flux flow region, which can be well fitted by a simple power-law relation:

$$\frac{E}{E_c} = \left(\frac{I}{I_c} \right)^n \qquad \text{Equation 3-3}$$

where E and I are the measured voltage and current, E_c is the voltage criterion and I_c is the critical current related to E_c.

According to this equation, if the relation between E_c and I_c is determined, the superconductivity can be characterized by I_c and the n-value, which is very important for numerical models. By varying the n-value from 1 to infinity, this relation can be used to cover most conductors from an ohmic metal to an ideal superconductor in the critical state. When n has some finite values, the flux creep region in Figure 3-3 can be well depicted.

Although *E-I* curves for LTS and HTS are very similar in the formula, the physics behind the formula are different. For conventional LTSs, the *E-I* curve is widely believed to result from the non-uniformity of the critical current density. The transition process in LTS from the flux creep region to the flux flowing region is very swift compared to HTS. In other words, the n-values for LTS are usually much larger than that for HTS.

For hard superconductors, including HTS, the *E-I* transition curve can be explained by the theory of thermally activated flux creep proposed by Anderson and Kim [80]. This theory showed that random thermal fluctuation can promote the vortex to migrate away from its equilibrium position, which has a minimum energy. The escaped vortices tend to move slowly, or creep, in order to relax the pinned energy. This relaxation process can be described by the escaped rate, R, which is related to the Boltzmann factor [81]:

$$R = v_0 e^{-\frac{U_p}{k_B T_n}} \qquad \text{Equation 3-4}$$

where U_p is the pinning potential energy, v_0 is the attempt frequency, k_B is the Boltzmann constant and T_n denotes the temperature.

By extending the standard flux flow model, the *E-J* characteristic in the current condition can be found in Ref [81]:

$$\rho_n = \frac{E}{I} = \frac{v_0 B L_p}{I_c}\left(\frac{I}{I_c}\right)^{-\frac{U_p}{k_B T_n}} \qquad \text{Equation 3-5}$$

where ρ_n is the flux flow resistivity due to flux creep, L_p is the pinning potential range, and v_0 is the attempt frequency of a flux bundle to hop a distance.

Comparing Equation 3-3 to Equation 3-5, we can derive the microscopic explanation of the n value:

$$n \propto -\frac{U_p}{k_B T_n} \propto U_p \qquad \text{Equation 3-6}$$

Equation (3-6) shows that the n value is proportional to the pinning energy, U_p, given a constant temperature.

3.1.3 Anisotropy of 2G HTS conductors

The anisotropy of the 2G HTS conductor refers to the phenomenon in which the critical current not only depends on the magnitude of the external magnetic field, but also on its direction. This anisotropy should be considered when the superconducting component is being designed. Theoretical and experimental research into anisotropy is therefore necessary.

According to the physics of 2G HTS conductors, two factors are influential to anisotropy: the layer structure of the oxide ceramic, and the boundaries between the grains. Since the layer structure is an intrinsic property of the material, more attention has been paid to the study of the effect of the grain boundaries on anisotropy. Meer et al. developed a model to describe the angular dependence of the critical current of a superconducting tape [82]. This model assumed that the Gaussian distribution of the misalignment angles of the grains and the critical current of the tape only depends on the magnetic field perpendicular to the surface. This model can be used to determine the critical current behaviour for all orientations of the magnetic field. Kiss et al. proposed a *E-J* relation based on a statistical analysis of the critical current by random flux pinnings to analyse the critical current dependence on external field angles [83, 84]. A comparison between this model and experiments shows that in a weak field and at small angles, the agreement is pretty good.

Although these studies help us to understand the physics of anisotropy, from an engineering perspective another model, the Kim model, is more popular in dealing with real engineering problems [80]:

$$I_c(B) = \frac{I_{c0}}{1 + B / B_0} \qquad \text{Equation 3-7}$$

where I_{c0} is the self field critical current, $I_c(B)$ is the critical current under a magnetic field B, and B_0 is a fitting parameter. For an isotropy superconductor this equation can be applied directly. But for a superconductor with anisotropy, such as 2G HTS, some

modification is needed to take into account the angular effect. Usually, the critical current is measured under parallel and perpendicular fields, so Equation 3-7 can be extended to parallel and perpendicular fields respectively:

$$I_c(B,\perp) = -\frac{I_c}{1+B/B_{0\perp}} \qquad \text{Equation 3-8}$$

$$I_c(B,\|) = -\frac{I_c}{1+B/B_{0\|}} \qquad \text{Equation 3-9}$$

where $B_{0\perp}$ and $B_{0\|}$ are the fitting parameters under perpendicular and parallel fields similar to B_0.

Equation 3-8 and Equation 3-9 only give us the critical current in the parallel and perpendicular directions. In order to calculate the critical current other directions, we need to use another theory called the effective mass model. According to the effective mass model, an applied magnetic field H is equal to an effective magnetic field $H'_{\perp}$ perpendicular to the ab-plane when the applied magnetic field H is tilted away from the c axis. Under the approximation of $m_a = m_b = m_{ab}$ (m_a and m_b represent the effective mass along the a and b principal axes, respectively), the effective $H'_{\perp}$ obeys [85]:

$$H'_{\perp} = H\left(\sin^2\theta + \frac{1}{\gamma^2}\cos^2\theta\right)^{\frac{1}{2}} \qquad \text{Equation 3-10}$$

where $\gamma = \frac{B_{0\|}}{B_{0\perp}}$ is the parameter characterizing the anisotropy of the high-temperature superconductor (for YBCO, $\gamma = 5-7$, for BSCCO, $\gamma > 10$). θ is the angle between the magnetic field direction and the ab-plane.

Assuming that the grains are well aligned in the HTS tape, and that the critical current of such a tape depends mainly on the component of the magnetic field applied perpendicular to the tape surface (ab-plane), from Equation 3-7 and Equation 3-8, the expression of the critical current for an arbitrary angle will be [85]:

$$I_c(B,\theta) = \frac{I_c}{1+\frac{B}{B_{0\perp}}\left(\sin^2\theta + \frac{1}{\gamma^2}\cos^2\theta\right)^{\frac{1}{2}}} \qquad \text{Equation 3-11}$$

If the critical current of such a tape depends mainly on the component of the magnetic field applied parallel to the tape surface (*ab*-plane), the expression of the critical current based on $B_{0||}$ will be [85]:

$$I_c(B,\theta) = \frac{I_c}{1+\frac{B}{B_{0||}}\left(\sin^2\theta+\frac{1}{\gamma^2}\cos^2\theta\right)^{\frac{1}{2}}} \qquad \text{Equation 3-12}$$

Equation 3-11and Equation 3-12 can be employed to calculate the critical current under a tilted magnetic field. The only unknown parameter, γ, can be determined by measurement of the critical current under parallel and perpendicular magnetic fields.

3.1.4 Impregnation process

Superconducting devices under high mechanical loads such as high field magnets, generators, motors and transformers should be stabilized by filling the voids in the structure so that they can resist the massive Lorentz force. Additionally, the use of cryocoolers requires impregnation of the superconducting tapes and coils to enhance the thermal stability. Many materials have been explored for both low temperature superconducting and high temperature superconducting coils.

Animal wax, such as beeswax, as well as petroleum derived waxes and paraffin were used for a long time with low temperature magnets [75]. They were useful as magnet-coil filling agents to minimize the probability of thermal runaway events that could result from micro fracturing during impregnation of superconducting coils. However, these waxes had high thermal expansion and low thermal conductivity, and cracks emerged and developed quickly if the temperature changed rapidly. Furthermore, due to their weak mechanical properties, the waxes could hardly contribute to the overall mechanical stability of the magnets [55].

Recently intensive research studies have been carried out to apply epoxy resins, such as Stycast 1266, Stycast 2850FT and Araldite as impregnation materials in HTS tapes and coils. These resins are preferred for their higher mechanical strength, good thermal conductivity and relatively small thermal expansion. Barth tested the critical current of short samples and Roebel cable with resin encapsulation [55]. Takematsu and Suzuki measured the critical current of YBCO coil with epoxy impregnation [86]. Their results revealed that the epoxies degrade the critical current of superconducting tapes and coils.

The mechanism for degradation due to impregnation has also been investigated. It is widely believed that this degradation is mainly due to the stress induced by the mismatch in thermal expansion. Petrie listed five basic stress types common to adhesive joints: tensile stress, shear stress, compressive stress, cleavage stress and peel stress [87]. Tensile stress corresponds to the transverse tensile stress. Cleavage occurs when an external force acts to open one edge of the adhesive assembly. Peel is similar to cleavage. In the case of cleavage and peel, the stress is concentrated on a small part of the adhesive bond and therefore their (cleavage and peel) strengths are much lower than the tensile strength. Therefore, both cleavage and peel are undesirable and are usually avoided in the adhesive bond assembly design.

Some methods have been tried in order to remove the degradation, , including adding quartz powder to decrease the thermal expansion [55], depositing polyimide to wrap the tape, and winding the coil with tension [88]. Some other methods have also proposed to discuss the degradation. Zhang used a heat-shrink tube to insulate the HTS tape to prevent delamination due to epoxy impregnation [89]. Her experiment results showed that the insulated coil had no current degradation before or after the epoxy impregnation process.

3.2 Experimental system

3.2.1 Tested superconductors

Samples were tested from several different commercial companies: SuperPower Inc, SuNAM Inc. and SuperOX. Major technical details of the samples are shown in Table 3.1.

Table 3-1 Paramters of the commerical 2G HTS conducotrs

Sample type	**Total thickness** ***mm***	**Width** ***mm***	**Critical current** ***A***	***n*-value**
SuperPower SCS4050 AP	0.2	4	120	27
SuNAM SCN	0.2	4	217	43
SuNAM HCN	0.2	4	217	43

SuperOX	0.14	4	169	34

Samples from SuperPower Inc.

The SCS4050 AP superconducting tape from SuperPower was tested. This wire was manufactured by metal organic chemical vapour deposition (MOCVD) on an ion beam assisted deposition (IBAD) made MgO template. The YBCO layer had a thickness of 1 μm and a width of 4 *mm,* as shown in Figure 3-4(a). The substrate was the non-magnetic alloy Hastelloy, with a thickness of 50 μm. 2 μm silver layers were coated on both sides of the YBCO layer to enhance the electrical contact using the sputtering technique.

Samples from SuNAM Inc

SuNAM tapes were produced by depositing GdBCO coated conductors (CCs) on a $LaMnO_3$ (LMO)-buffered IBAD MgO template, produced by the Reactive Co-Evaporation Deposition & Reaction (RCE-DR) process, as shown in Figure 3-4(b). The thickness of the superconducting layer in SuNAM tapes was 2–3 μm. Both tapes had a width of 4 *mm*. Two types of superconductors from SuNAM Inc were examined: SCN 4050 and HCN 4050. The difference between these two tapes lied in the substrate. SCN employed stainless steel to enhance the mechanical strength, while HCN used copper to stabilize the GdBCO layer.

Sample from SuperOX

SuperOX was a commercial superconductor supplier located in Russia. The MgO template was made using IBAD and pulsed laser deposition was used for depositing the YBCO layer in Figure 3-4(c). The substrate was non-magnetic Hastelloy C276 tapes, which were annealed after cold rolling.

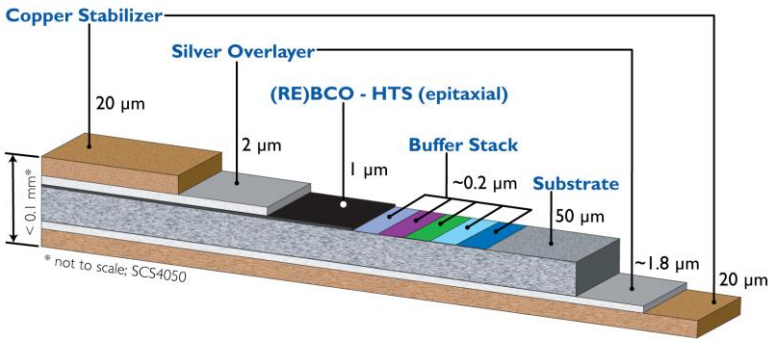

(a)

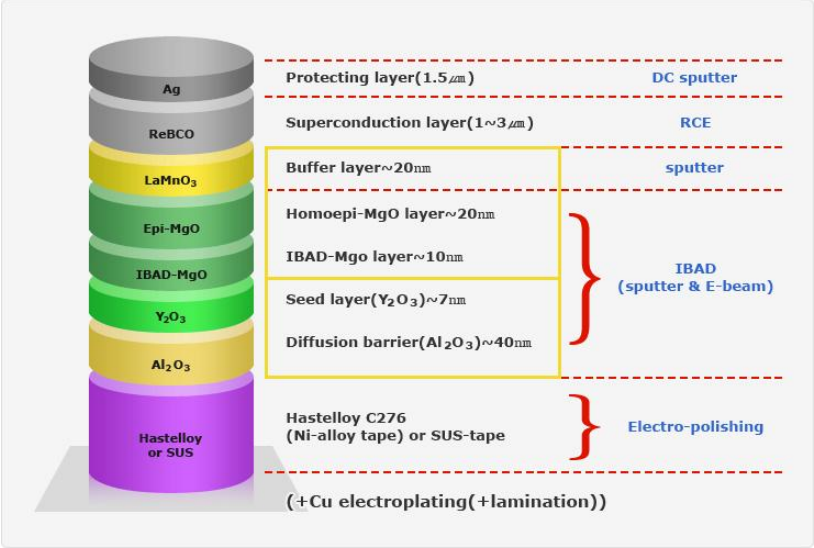

(b)

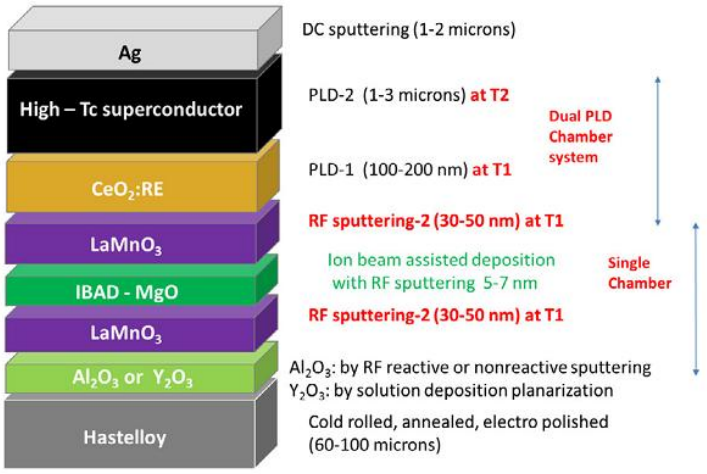

(c)

Figure 3-4 Architecture of three different YBCO tapes: (a) SuperPower [90]; (b) SuNAM [91]; (c) SuperOX [92]

3.2.2 Critical current test system

The critical current is the maximum current that can be transported by the tape or the coil. It is usually defined using the voltage drop of 10^{-4} *V/m* in the *E-I* curve. The resistance of the superconductor is assumed to be negligible when the current is below the critical current. The superconductor is considered to be a normal conductor when the current exceeds the critical current.

The standard method used for determining the *E-I* curve is the four-probe method. This measurement is implemented using LabVIEW with NI hardware to acquire the

physical signals. Figure 3-5 below outlines the measurement process: a DC current is applied to the YBCO tape and the voltage between the voltage taps is measured. This voltage is gauged by NI DAQ hardware and processed before it is sent to the computer. This voltage is divided by the distance between the voltage taps to calculate the electric field *E*. Then, the *E-I* curve is displayed on the screen in real time. The YBCO tape is held by G10 former. The configuration of the sample is shown in Figure 3-6.

A direct current power supply (HP 6681A) with a maximum output voltage of 8 *V* and a maximum current of 580 *A*, is used as a current source. During the critical current tests the power supply operates in a linearly varying current mode. The amplitude and the duration of the current output is controlled either remotely by standard commands to the programmable instruments over an IEEE 4888 bus or locally by an analogue button. The card can be linked to LabVIEW and programmed to acquire or generate voltage signals.

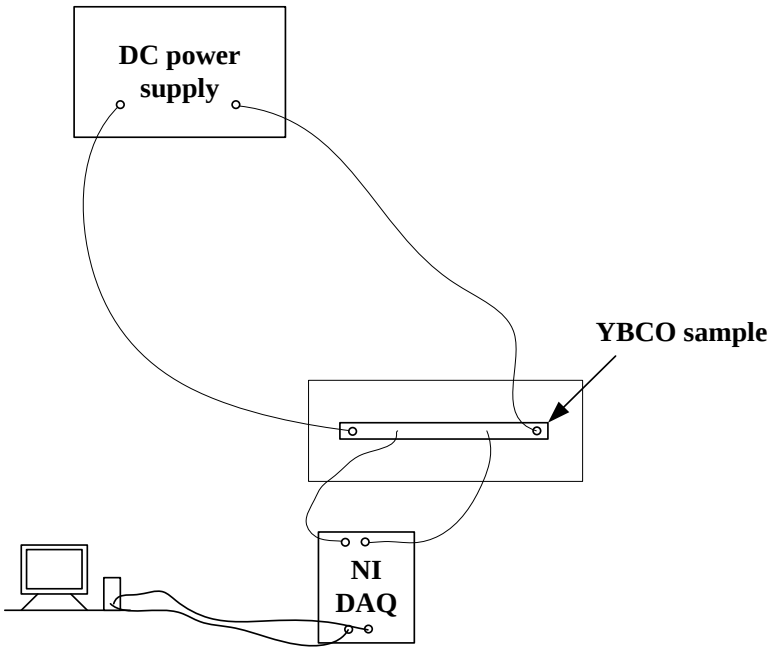

Figure 3-5 The critical current measurement circuit for superconducting tape

In the critical current measurements there are several sources of uncertainties. These uncertainties can be in the determination of the voltage gap distance, in the voltage signal and in the calibration of the shunt resistance. In order to improve the precision of the measurement, the voltage taps are carefully soldered by minimising the size of the joints. Before the measurements, the voltage range is selected to match the measured

signal. The current measured using the shunt resistance is compared with other techniques so as to verify the accuracy.

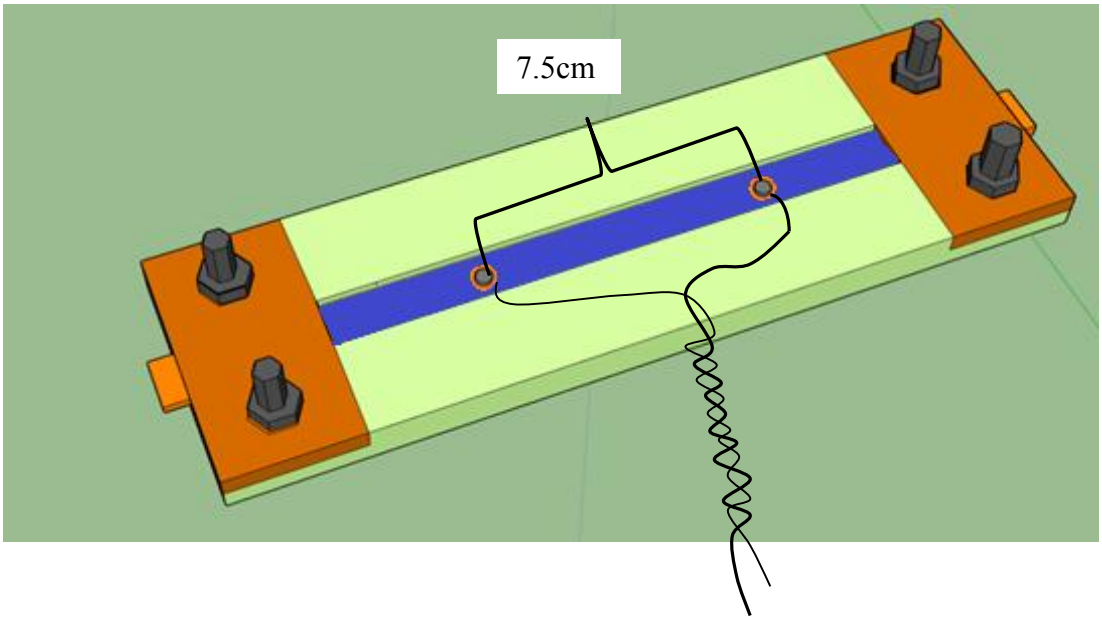

Figure 3-6 The superconducting tape impregnated with resin. The blue part represents the filled resin. Two voltage taps are soldered onto the tape before impregnation.

3.2.3 AC loss test system

The AC losses of the coils are measured after the I_c characterization [93]. Figure 3-7 shows the circuit diagram of the transport AC loss measurement using the electrical method with the high accuracy data acquisition (DAQ) system. The superconducting samples are supplied with an AC current using a power amplifier controlled by a signal generator. The voltage loss signal between the terminals of the coil is superposed with the inductive component, which can be eliminated using a cancellation coil. The voltage signal of the pancake coil after compensation is amplified and filtered to remove the harmonic components using a high accuracy DAQ measurement system with the LabVIEW program. The transporting AC loss of the pancake coil per cycle is given as:

$$Q = \frac{V_{rms} I_{rms}}{f} \qquad \text{Equation 3-13}$$

where f is the frequency, and I_{rms} and V_{rms} are the in-phase current and the voltage, respectively.

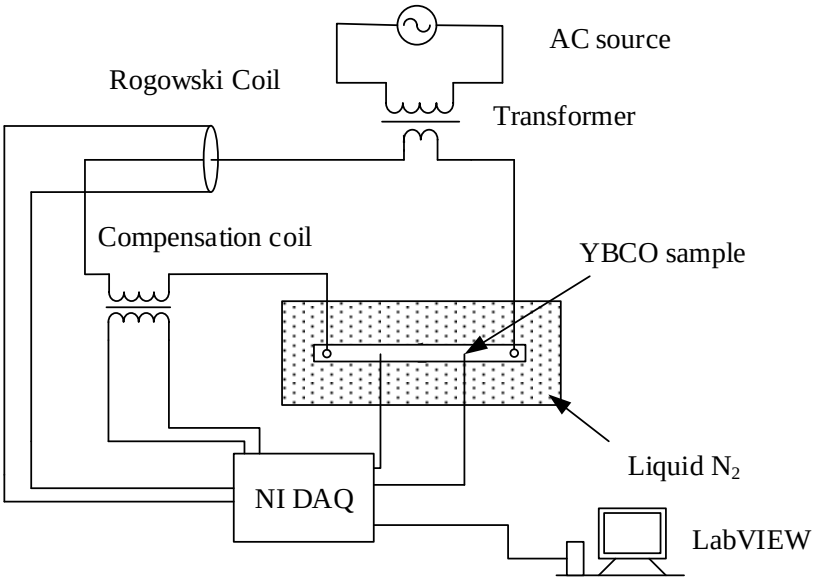

Figure 3-7 AC loss measurement circuit for tape sample.

3.2.4 External magnetic generator

The magnetic field dependency of the superconducting tape can be studied using a DXDP 6300 DC magnetic field generator. The superconducting samples are mounted on a G10 holder positioned in the centre of the poles of the DXDP 6300, using a liquid nitrogen bath. The DXDP 6300 has a maximum current of 28 *A*, which can generate a magnetic field of 1.5 *T*. A DC power supply is used to power the electromagnetic generator in the experiment. The current and voltage of the DC power supply are controlled by the programmable front panel. A DXAC5600B-R22 cooling water circulating machine is used to automatically cool the electromagnet. A Gauss meter is employed to calibrate the magnetic field and the applied current. This is a full-digital high-precision teslameter which provides a wide-range measurement.

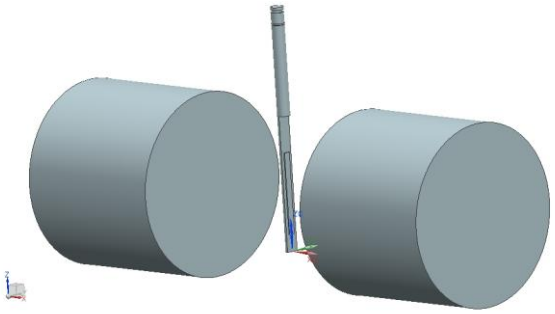

Figure 3-8 Schematic view of experimental set-up in which the cylinders represent the magnet poles. The tape is fixed by a non-magnetic block in the centre of the two magnet poles.

3.2.5 Impregnation process

Three epoxies, Stycast 2850FT, Stycast 1266 , Araldite, and commercial liquid metal Galinstan were selected to impregnate the superconducting tape, due to their superior performance in cryogenic environments. These three resins were chosen as they had been well studied and had many reliable physical parameters. All the epoxies were two component resins. They were prepared according to the instructions provided in the manuals. Table 3-2 below shows the mixture ratios and cure conditions. Galinstan was supplied by German company Geratherm Medical AG, which had the melting temperature of -19 °C.

Table 3-2 The curing methods for three resins during the impregnation process

Resin		Ratio in weight	Cure condition
Stycast Black	Stycast 2085 FT	100	24h
	Catalyst 9	4	
Stycast 1266	Stycast 1266 Part A	100	16h
	Stycast 1266 Part B	28	
Araldite DBF	Araldite DBF	100	48h
	Hardener HY951	10	

All the superconducting tape samples are prepared using identical methods. The tapes were first cleaned with Acetone and Ethanol. Then they were encapsulated into a U-shape former made of glass-fibre-reinforced-plastics (G10) using the glue or resin mixture. Two pieces of copper plate were fixed to the holder at both ends and were connected to the current lead. The liquid metal or resin mixture was distributed homogeneously and the resin was curing under vacuum conditions. The schematic graph and final entity were shown in Figure 3-6. Voltage tapes were soldered to the tapes on the upper surface leaving a 10 cm gap. The critical current was measured in a liquid nitrogen bath at 77 K in a self-field condition. The critical current of the sample was defined by a critical electrical field E_c of $1\mu V/cm$.

3.3 Experimental results under an external field

3.3.1 Field dependency

In order to analyse the relationship between the critical current of the tape and the angle between the external field and the tape, *E-I* curves of a single tape were measured under a DC magnetic field. Figure 3-9 presents the *E-I* curves of the superconducting tapes from SuperPower, and Figure 3-10 shows SuNAM tapes under different magnetic fields. All the *E-I* curves were in power law shapes, as shown in Figure 2-1. According to the 1 $\mu V/cm$ criterion, the SuNAM tape has a critical current of 217 A in a self field, while the SuperPower tape has a critical current of 120 A. In the rest of this paper, the perpendicular field was referred as $B_{\perp}$, which was perpendicular to the surface of the conductor. Similarly, the parallel field was denoted as $B_{\parallel}$.

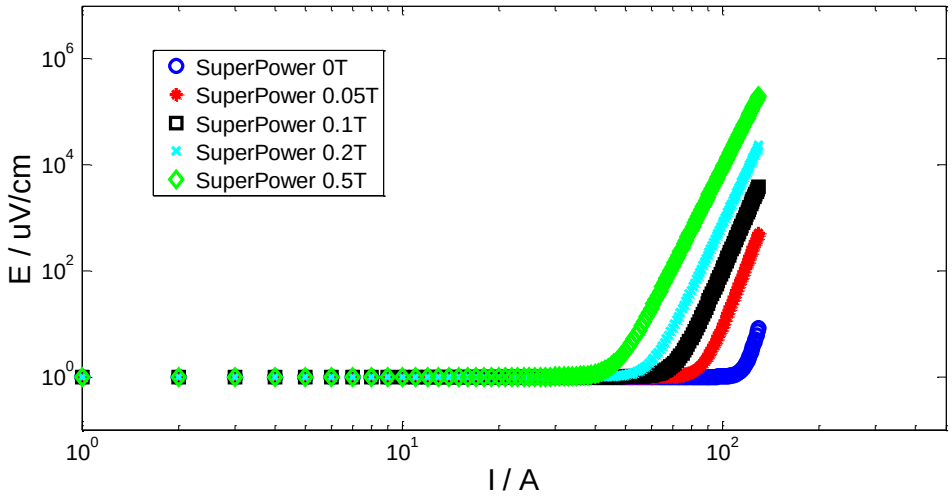

Figure 3-9 *E-I* curve of SuperPower tape under different external fields in the parallel direction

Figure 3-11 shows measured field dependency for SuNAM tape and SuperPower tape.These two graphs reveal that the SuperPower tape behaves quite differently from the SuNAM tape in a magnetic field, where the critical current of the SuperPower tape in a parallel field is smaller than the critical current under a perpendicular field, whereas the other tapes have a smaller critical current under a perpendicular field, like the SuNAM tape.

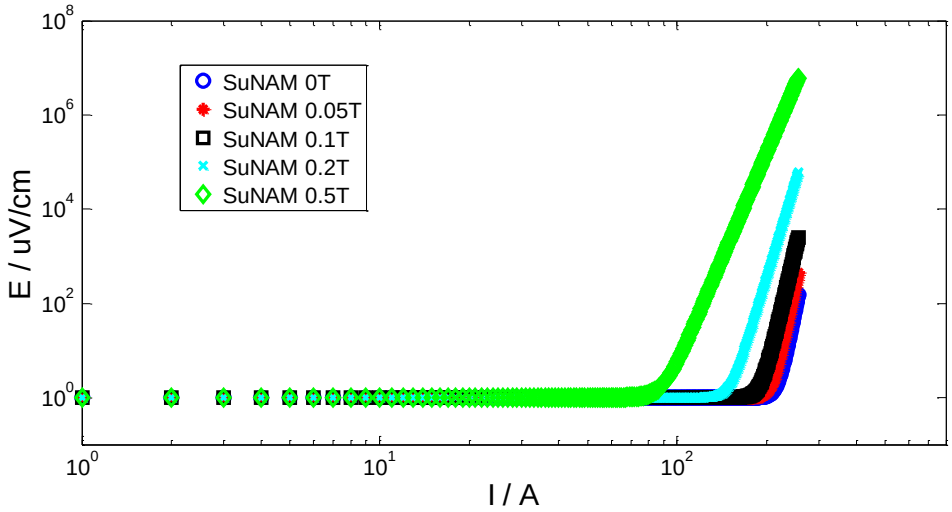

Figure 3-10 *E-I* curve of SuNAM tape under different external fields in the perpendicular direction

New progress has recently been made to YBCO tape fabrication by SuperPower, which shows a different magnetic field dependency. This wire is an AP (Advanced Pinning) type which has zirconium doping that forms $BaZrO_3$ nanocolumnar particles in the film. These $BaZrO_3$ nanocolumns are aligned in parallel to the c-axis of REBCO. The result is the flux pinning for $H//c$ is greatly enhanced. When the pinning from the nanocolumns is strong enough, the $I_c(H//c)$ becomes higher than the $I_c(H//ab)$.

Anisotropy of the YBCO tape under an external magnetic field would greatly influence the current and magnetic field distribution inside the coil. We used a modified Kim model to consider anisotropy of YBCO tapes in the simulation. This method avoids the complicated optimization process of determining variables. The modified Kim model is:

$$J_c\left(B_1, B_2\right) = \frac{J_{c0} B_{10}}{B_{10} + \sqrt{\left(\left(B_1\right)^2 + \left(kB_2\right)\right)^2}} \qquad \text{Equation 3-14}$$

where B_1 is the lower curve of each tape in Figure 3-11 and B_2 is the higher curve. B_{10} is the field when the current is half of the critical current on the B_1 curve, and similarly B_{20} is the corresponding field on the B_2 curve. k is the ratio between B_{10} and B_{20}, which describes the anisotropy of B_1 and B_2. The data used was based on the measured parameters of the SuNAM tape and the SuperPower tape at 77 K. Table 3-3 summarizes the derived values from the measured data.

Having discussed the critical current dependency of on the magnitude of external field, the next step is to analyse the *n* value dependency on the external field. Figure 3-12 presents a comparison of the normalized critical current and normalized n-value under magnetic fields for the SuNAM and SuperPower tapes. Here the SuNAM tape is under a perpendicular field, while SuperPower tape is under a parallel field.

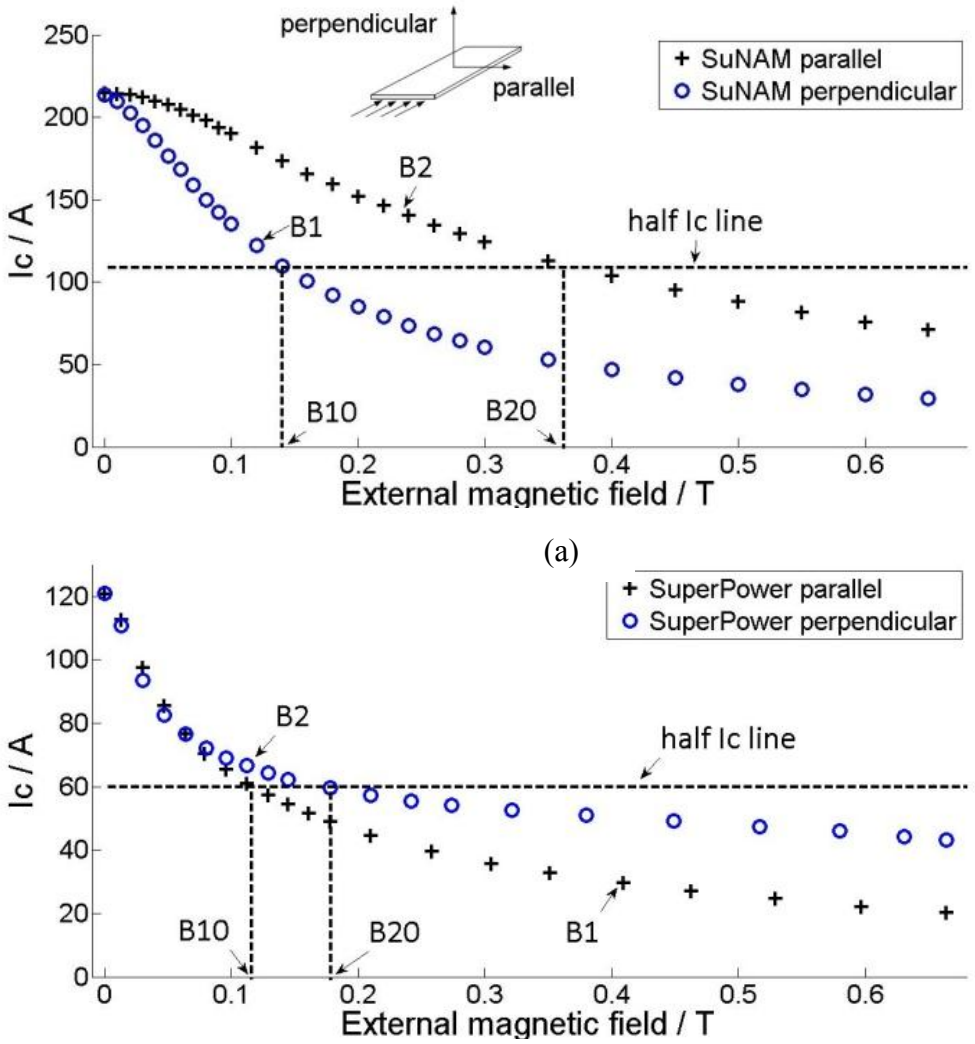

Figure 3-11 Measured field dependency fo tape and SuperPower tape. B_1 represents the lower curve, and B_{10} is the field when the current is equal to half of the critical current on the B_1 curve. B_2 represents the upper curve, and B_{20} is the field when the current is equal to half of the critical current on the B_2 curve.

According to the Anderson flux creep theory, the pinned flux, which transports macroscopic current, is only in the metastable state when the temperature $T > 0$ K. Thermal fluctuation causes the flux to move slowly and randomly, which breaks the balance between the pinning force, F_p, and the Lorentz force, F_L. Here, the pinning force

prevents the migration of the vortex and therefore acts as an energy barrier. This barrier, U_p, is proportional to the critical current:

$$J_c \propto U_p \qquad \text{Equation 3-15}$$

Comparing Equation 3-6 and Equation 3-15, both critical current I_c and the n value are expected to be proportional to U_p, which can be verified by Figure 3-12. Figure 3-12 shows that the critical current and the n value have very similar relationships with the external field, decreasing continuously when the external field increases. For the SuperPower tape, the n-value is a bit larger than the normalized I_c, probably because the enhanced pinning in c-axis increases the n-value.

Table 3-3 Field dependency parameters for SuNAM and SuperPower tapes. These values are derived from Figure 3-11

Type of tapes	SuNAM	SuperPower
B_1	Perpendicular	Parallel
B_{10} (T)	0.140	0.115
B_2	Parallel	Perpendicular
B_{20} (mT)	0.360	0.180
k	0.140/0.360	0.115/0.180

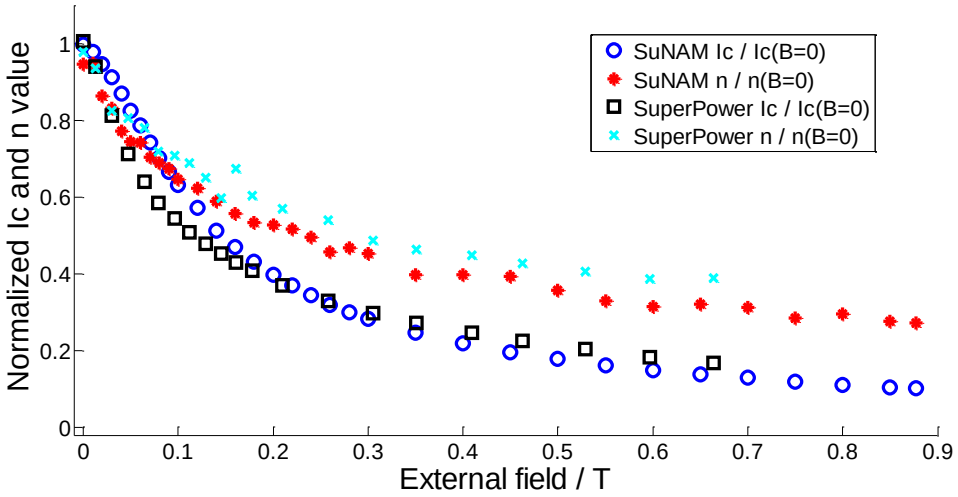

Figure 3-12 Comparison of normalized critical current and normalized n-value under magnetic fields: SuNAM tape is under perpendicular field; SuperPower tape is under parallel field.

3.3.2 Angular dependency

Figure 3-13 present the experimental and calculated critical current of a short SuperPower tape under different magnetic fields. The critical current curves are normalized by the critical current values obtained under parallel external magnetic field ($\theta = 0$). $B_{0||}$ and $B_{0\perp}$ are determined by the *E-I* curves under the parallel and perpendicular fields, as shown in Figure 3-11. The ratio between $B_{0||}$ and $B_{0\perp}$ is equal to γ . With these values, the critical current under an arbitrary angle and the magnitude of external field can be calculated using Equation 3-11 and Equation 3-12.

From Figure 3-13, we can find that under a weak magnetic field, the angular dependency of critical current with the tape surface is small. When the external field reaches a certain value (i.e. 0.2 T), the critical current decreases sharply as the angle increases from 0° to 40°. When the angle is between 50° and 130°, the critical current vary less dramaticaly. For a single tape under a magnetic field, the measured critical currents show good agreement with the calculated results, when the external field is small. However, the difference between the experimental and theoretical results becomes quite obvious when the external field is large. This is because the Kim model has a greater error under a strong field, while a weak external field can be well fitted by the Kim model. It also means that Kim model is suitable to apply in numerical modelling when the magnetic field is small. When the magnetic field is larger than 0.2T, for example in Figure 3-13 Comparison of normalized critical current under different DC magnetic fields and different angles.Figure 3-13, other field dependency model is preferred [127].

Figure 3-14 shows a comparison of the normalized experimental *n* value under different DC magnetic fields and different angles. Generally speaking, the angular dependency of *n* value is quite similar to the angular dependency of the critical current, which can also be partially explained by Equation 3-6 and Equation 3-15, because this pattern is quite similar to the critical current trend shown in Figure 3-13 (a). When the external field reaches a certain value (i.e. 0.2 T), the *n* value decreases sharply as the angle increases from 0°to 40°. When the angle is between 50° and 130°, the critical current remains almost constant.

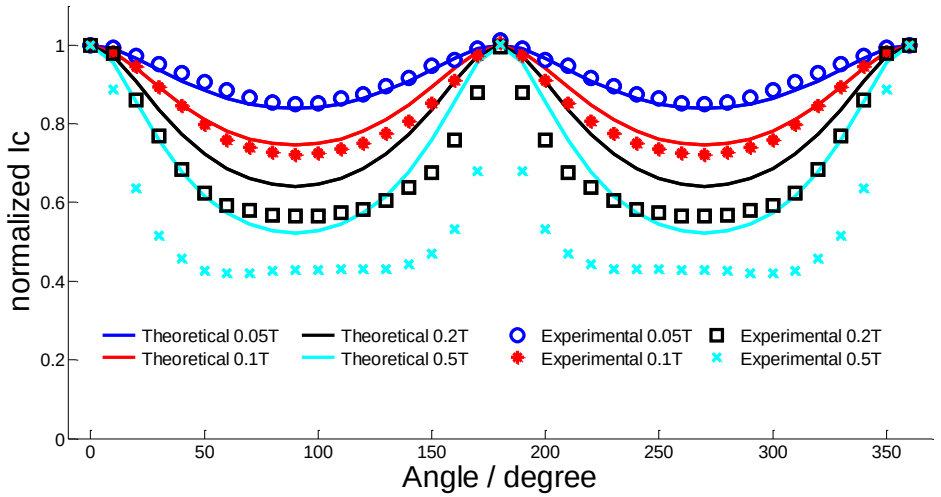

Figure 3-13 Comparison of normalized critical current under different DC magnetic fields and different angles.

3.4 Experimental results with impregnation process

3.4.1 Critical current

Different impregnation materials have different I_c and n value degradation effects for SuperPower's 0.1 *mm* tape. Figure 3-15(a) shows the *E-I* curves of samples with Gallinstan impregnation. The critical currents and n values are almost the same as the unimpregnated sample, which means that Gallinstan hardly degrades the YBCO tape. There are two possible reasons for this. The first reason is that the thermal mismatch is not big enough to induce cracks on the YBCO layer. In order to support this argument, further research is needed to determine the thermal expansion coefficient. The second reason may be the wettability of Gallinstan with copper is not very high [94], which will reduce the bonding between the Gallinstan and the tape, thus reducing the tension in the tape.

Unlike Gallinstan, other resins show degradation at different levels. Among the three samples in the group of Stycast Black (Figure 3-15(b)), one shows no degradation, while the other two show decrease critical currents from 107 *A* to about 80 *A*. The degraded tapes have different n values. The n value of one degraded tape is 86, even larger than the original n value of 31. The other tape has an n value of 21. In the group of Stycast 1266 (Figure 3-15(c)), two of the samples degrade to less than 30 *A*. For Araldite (Figure 3-15(d)), the samples degrade to critical currents of 32 A, 45 *A* and 76 *A*. In conclusion,

that Stycast Black decreases the I_c slightly, however, Stycast 1266 and Araldite degrade the critical current substantially.

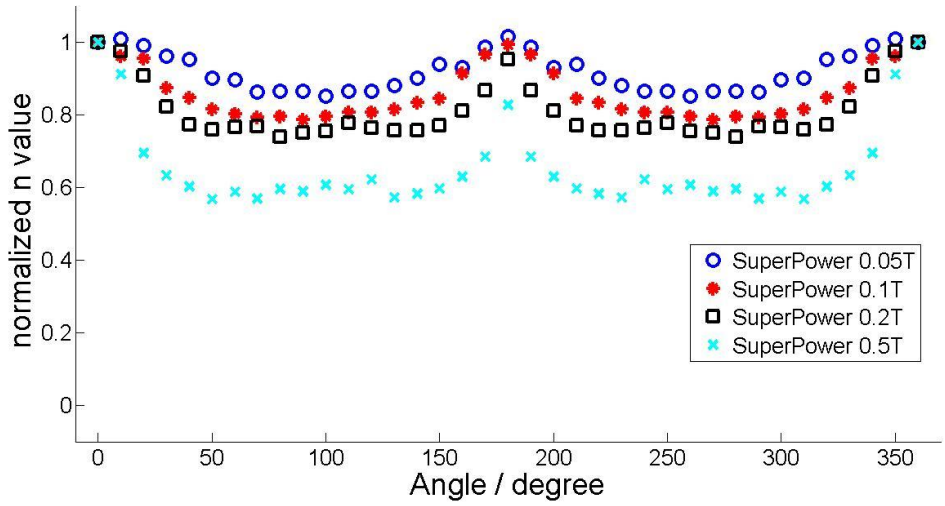

Figure 3-14 Comparison of normalized n value under different DC magnetic fields and different angles by experiment.

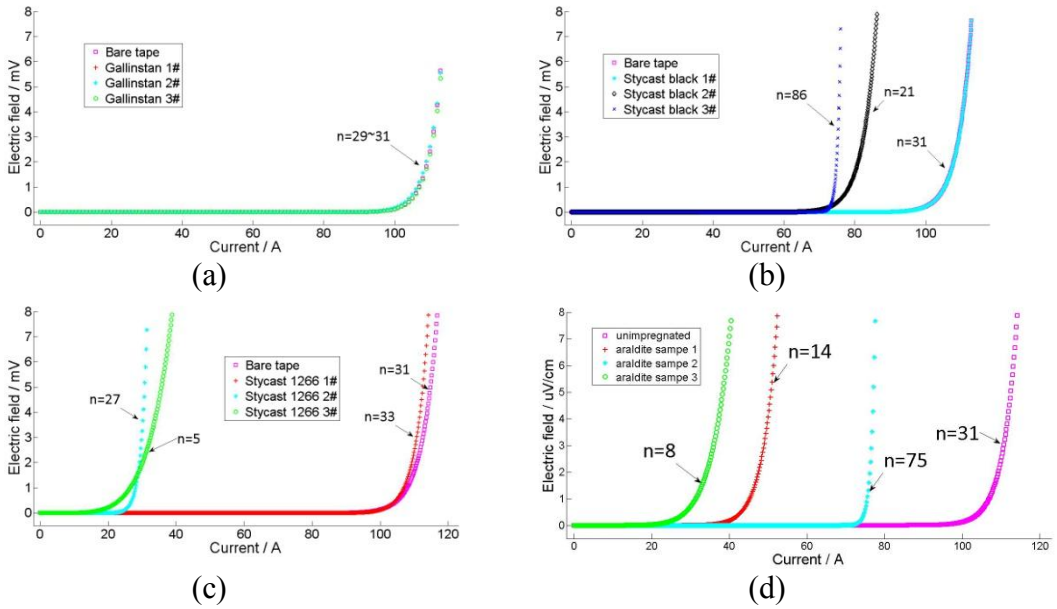

Figure 3-15 *E-I* curves of SuperPower SCS4050 tape with different material impregnation: a) Gallinstan; b) Stycast Black; c) Stycast 1266; d) Araldite

Degradation is due to the thermal expansion coefficient. According to the literature, the thermal contractions from room temperature to 77 K are 0.45% for Stycast Black [95], about 0.9% for Stycast 1266 [96], and 1.2% for Araldite [96]. However, the thermal shrinkage for the YBCO stabilizer, copper, is about 0.26%. Thus, the thermal mismatch

between the resins and stabilizer induces strain within the superconductor tape, and thus degrades the I_c. This degradation is related to the degree of thermal mismatch. The larger the mismatch is, the more degradation occurs. Stycast Black slightly degrades the tape, while Stycast 1266 and Araldite degrade more seriously. According to these tests, Stycast Black and Gallinstan are relatively preferable for the purpose of impregnating the coil, in terms of critical current degradation.

Table 3-4 Critical currents and n values of SuperPower SCS 4050 tape samples under different impregnation materials. These values are derived from Figure 3-15

Material	Gallinstan		Stycast Black		Stycast 1266		Araldite	
	I_c	n	I_c	n	I_c	n	I_c	n
Sample 1	106.2	29	105.9	29	105.3	33	45	14
Sample 2	106.7	31	78	21	28	27	76	75
Sample 3	106.4	31	75	86	27	5	32	8
Bare sample	106.8	31	106.8	31	106.8	31	106.8	31

The degradation was further studied using different configurations of the superconductor tapes. Two kinds of SuperPower tapes were selected to implement the impregnation process. One tape had a thickness of 0.1 mm, with a copper stabilizer of 20 μm thickness on both sides. The other had a thickness of 0.18 mm, with a copper stabilizer of 60 μm thickness on both sides. A comparison of Figure 3-15(b) and Figure 3-16 shows that the first tape degraded obviously, not only in I_c but also in n value. However, the second tape showed hardly any degradation. The *E-I* curves of the 0.18 mm tape are almost the same as those of the unimpregnated tape. This is because the thicker copper stabilizer can protect the YBCO layer and reduce the strain imposed on the superconducting layer.

In order to test the influence of thermal cycle, the *E-I* curves of the 0.18 mm tape were compared to those of a tape with Stycast Black impregnation. Here one thermal cycle means that the sampled was quickly submerged into liquid nitrogen and held under for 10 minutes, and then taken out and warmed up to room temperature. Figure 3-16 and Figure 3-17 show that after five thermal cycles one of the samples degraded in critical

current and *n* value. This means that the resin may crack during thermal cycles and degrade the tape.

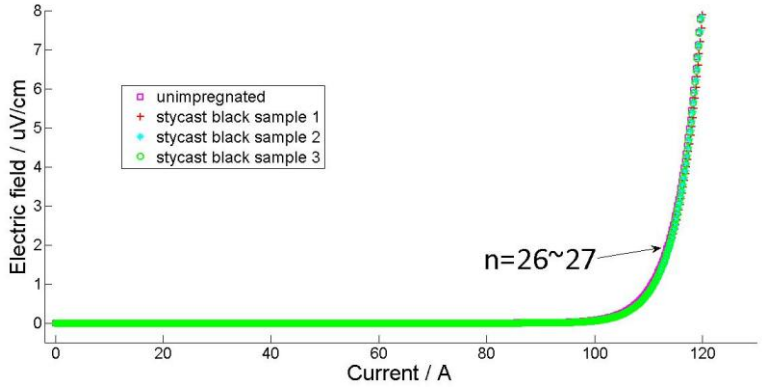

Figure 3-16 *E-I* curve of SuperPower 0.18 mm tape with Stycast Black impregnation

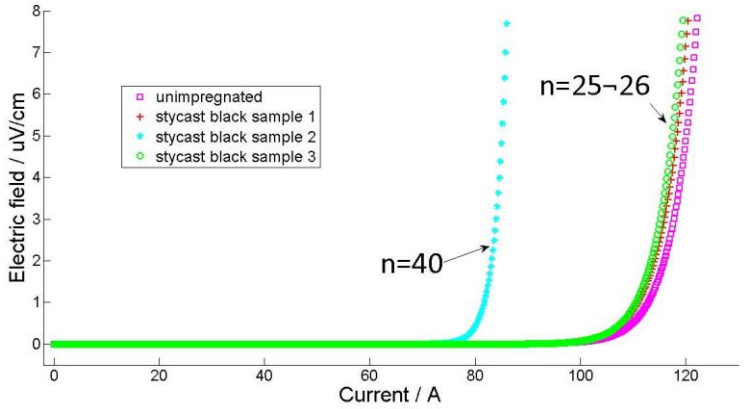

Figure 3-17 The *E-I* curve of SuperPower 0.18 mm tape with Stycast Black impregnation after five thermal cycles.

In our experiments, two *E-I* curve patterns are observed, as shown in Figure 3-18. The first one is pattern 1 in the graph. This pattern features in the resistivity transformation during the ramping up process. Resistivity begins to appear when the tape ramps above 20 A. The voltage increases continuously as the current increases, until the current approaches the critical current, shown by the vertical dashed line. This is a resistive pattern. The second pattern has a very swift superconducting transition. Before the tape reaches I_c = 118 A, the voltage curve rockets up at 84 A. This transition happens within 0.1 s, the electric field increasing from 0 to several thousand *V/m*. This is a skyrocketing pattern.

Different ramp rates were tested using SuperOX tape, as shown in Figure 3-19. The critical currents varies with different current ramping rates in the same sample. The

rocketing up current increases considerably as the ramp rates increase. When the ramp rate was 2 A/s the critical current was about 138 A, however this critical current increased to 158 A at 10 A/s.

Based on this ramp rate dependency, we infer that this transition is related to the thermal phenomenon. When the current reaches the transition current, the sample quickly quenches and the temperature quickly rises beyond the critical temperature, and the sample shows a swift transition. The quicker the ramp rate, the slower the heat generated by the disturbance, and the higher the transition current. Similar results were reported by Yaginasiwa [97]. The heat probably has two sources and the first one is the cracks due to the resin shrinkage between the voltage taps. The cracked region reaches quench quickly and initializes the whole quench. The second source could be the current lead as the impregnation material insult the tape from liquid nitrogen and hinder the process of heat transfer, finally cause the tape to quench. Further research is needed and is beyond the context of this thesis.

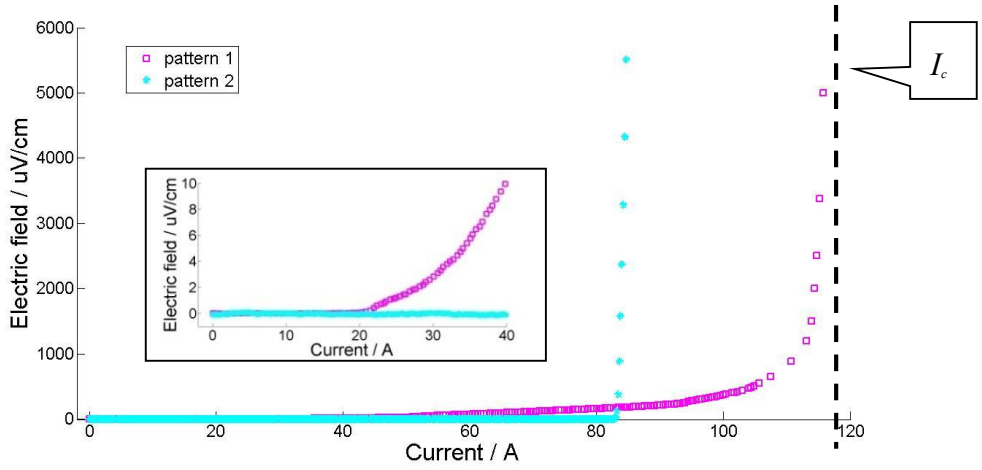

Figure 3-18 Two types of degradation patterns in the *E-I* curve: pattern 1 is a resistive pattern, and pattern 2 is a skyrocketing pattern. These patterns are based on SuperPower tape with a current ramp rate of 2 A/s.

In order to verify the influence of Stycast Black on coil impregnation, we wound two coils with the same geometry and number of turns. One was impregnated using Stycast Black, and the other was not. Each coil had 13 turns with an inner diameter of 56 mm. The tapes were non-insulated by SuperPower, which has a thickness of 0.18 mm. The two coils had almost the same *E-I* curve, as shown in Figure 3-20. The critical current

was 65 A and the *n* value was 18. This experiment confirms that degradation can be minimized by using a thicker tape with Stycast Black impregnation.

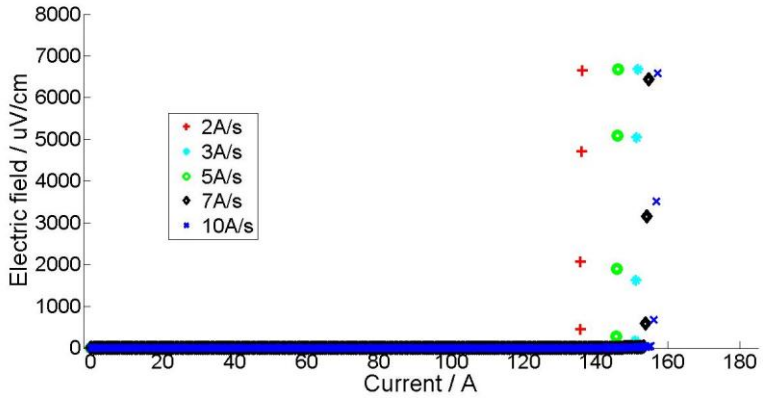

Figure 3-19 SuperOX tape with different current ramp rates. As the ramp rates increase, the rocketing up current increases.

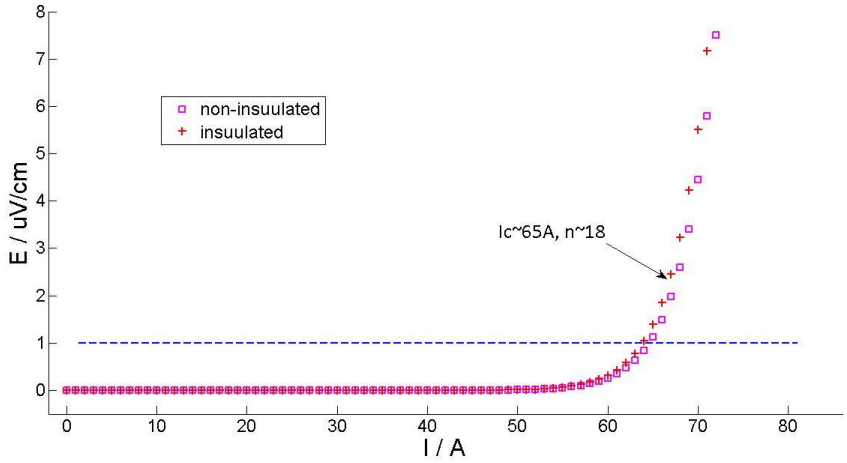

Figure 3-20 Tests on two 13-turn coils with Stycast Black using non-insulated tape and insulated tape. The critical current and *n* value show similar results.

3.4.2 AC loss

The results of transporting current loss measurements in a self field are presented for unit length by dividing the distance between the voltage taps. The measured values were compared to predictions from the Norris equation for an infinite-slab [28]. This equation calculates the loss in isolated wires of rectangular cross-section. The AC losses measured for a single bare tape is shown in Figure 3-21 as a function of the magnetic-field amplitude. Each series of symbols with a different style corresponds to a different

frequency. The tape has a critical current of 110 A in a self field. Figure 3-21 shows that the measurement results correspond fairly accurately to the model description.

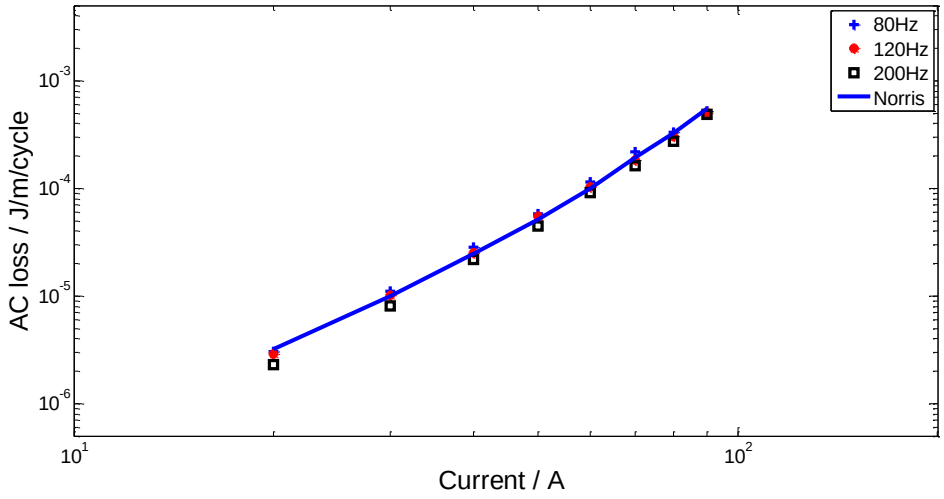

Figure 3-21 AC losses with non-insulated tape compared to the Norris equation

AC loss measurement results obtained using Gallinstan impregnation are displayed as symbols in Figure 3-22, compared to bare tape with the same parameters as before. For impregnated tape, at high frequencies there were clear differences between the different applied frequencies, from 80 Hz to 600 Hz. The measured AC loss increased non-linearly with the applied current frequency. This increase is explained by the induced eddy current in the Gallinstan.

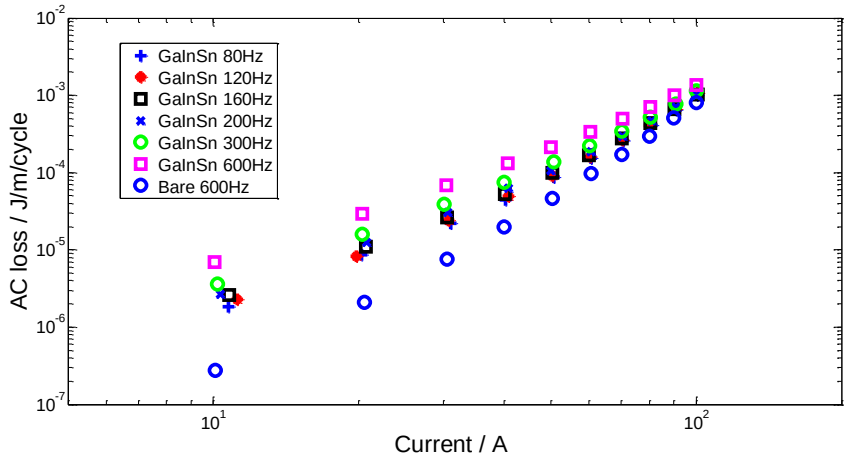

Figure 3-22 AC losses with Gallinstan impregnated tapes compared to non-insulated tape

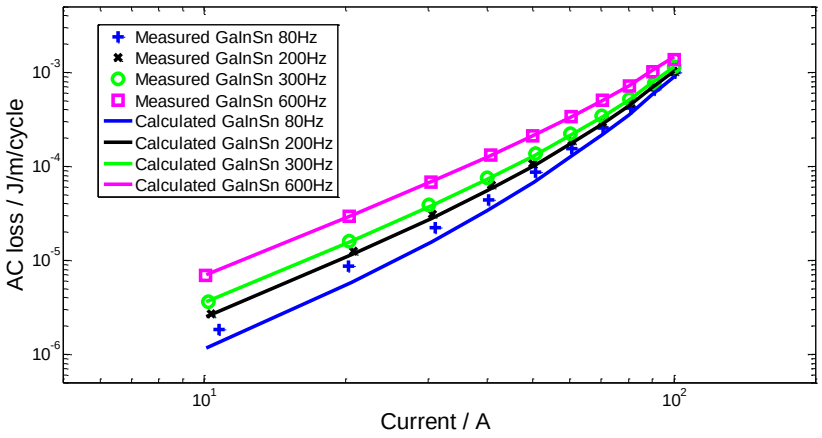

Figure 3-23 Measured AC losses with Gallinstan impregnated tapes compared to calculated losses

Figure 3-24 shows the comparison between measured AC losses and the calculated AC losses. The calculated AC losses consist of two parts: the hysteresis loss and eddy loss

$$Q_{means} = Q_e f + Q_h \qquad \text{Equation 3-16}$$

where Q_e is eddy loss, f is frequency, Q_h is hysteresis loss which can be calculated by Norris eqation. Eddy loss can be calculated as [142]

$$Q_e = \frac{\left(\mu_0 I_p\right)^2}{2\rho}\frac{d^3}{L} \qquad \text{Equation 3-17}$$

where I_p is the applied current, ρ is the reisistivity, which is , d is the thickness of the GaInSn and L is the perimeter of the GaInSn crosssection.

We further measured the AC losses of degraded tape by resin impregnation in Figure 3-25, where two groups are compared. All the samples were prepared using the same HTS tape, and the losses were measured using a transporting current with the same magnitude and frequencies. The first group had a critical current of 80 A and the second group has a critical current of 40 A. They were compared to the theoretical results from the Norris equation. For a single sample, the loss curves show quite good agreement under different frequencies, meaning that the loss is frequency independent. However, the samples with the same degraded current showed obvious discrepancies in the losses, which cannot be well predicted by the Norris equation. This suggests that the Norris equation can't be directly applied to calculate the degraded tape. The reason for this may

be that the degraded tape is no longer homogenous, which contradicts with the assumption in the Norris equation.

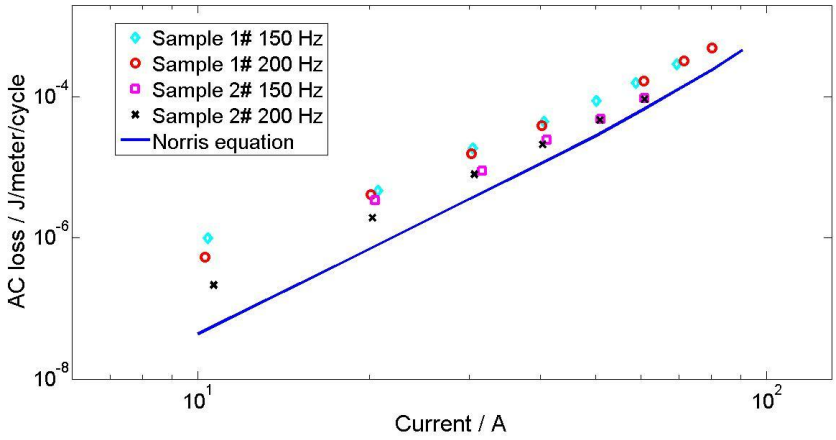

(a)

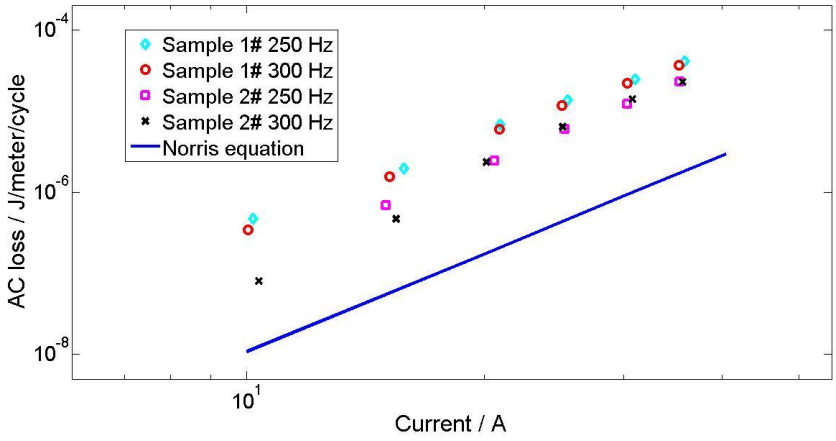

(b)

Figure 3-25 AC loss measurement for degraded tapes a) I_c=80A; b) I_c=40A

3.5 Summary

This chapter studied the tapes which are used to fabricate superconducting coils. The properties of the tape are the key factors in superconducting magnet design. Firstly, the critical currents of different tapes under external magnetic fields were measured and these data were fitted using the Kim model, which showed good agreement. Two field dependencies were found according to the experimental results. YBCO tapes from SuNAM shows a normal pattern which exhibits a larger critical current decrease in a perpendicular field than a parallel field. However, the latest SuperPower tapes behave differently, showing a greater decrease in the parallel direction. The field dependency of the *n*-value was also discussed, and it was found that the *n*-value decreases when the

external magnetic field increases, similar to the magnitude of the critical current. This similarity was discussed based on the flux flow theory.

The second part of Chapter 3 experimentally compared the influence of different impregnation materials on coated conductors. These impregnation materials included one liquid metal, Gallinstan, and three epoxy resins: Stycast Black, Stycast 1266 and Araldite. The experimental results showed that Gallinstan hardly degrades the tape, while resins result in different degrees of degradation. Comparatively, Stycast Black caused slight degradation in the tape, however, the other two resins degraded the tapes substantially. The degradation was closely related to the mismatch in thermal expansion. We further discussed the factors that affect the degradation. A thicker stabilizer can reduce the degradation, but thermal cycles may decrease the critical current. Two *E-I* curve patterns were observed: one behaves like a resistive transition, and the other like a skyrocketing transition. When the current reaches the transition current, the sample quench quickly and the temperature quickly rises beyond the critical temperature, so the sample shows a swift transition. Finally, the AC losses after impregnation were discussed. The Gallinstan impregnation experiments showed that AC losses are frequency dependent, due to the eddy loss within the Gallinstan. The AC losses with degraded tape were also measured, which showed that they cannot be predicted by the Norris equation. This is because the degraded tapes are no longer homogenous, which is the prerequisite of Norris equation.

Chapter 4. Modelling and Experiments of Single Superconducting Coils

It is well recognized that the superconductor is capable of transporting high current losslessly. Nowadays, many electrical devices and high magnetic field devices are developed to take advantage of the superior properties of superconductors. 2G HTS is the state-of-the-art conductor, for their high operating current and good behaviour under external magnetic field. Therefore, they attract intensive research.

2G HTS coils are the primary units for many applications. There are two types of coils in real applications: pancake coil (Figure 4-1 (a)) and racetrack coil (Figure 4-1 (b)). The pancake coil is parallel wound in a flat circular shape. This is the ideal configuration for homogeneous magnet, such as NMR, MRI and SMES magnets.

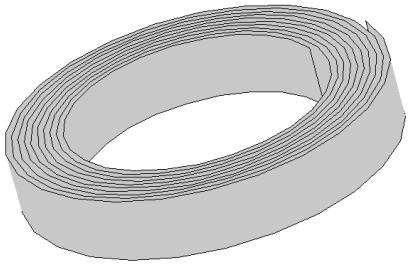

(a)

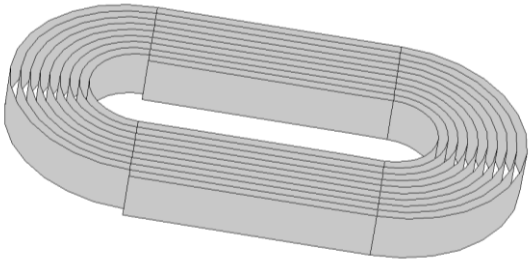

(b)

Figure 4-1 Two types of typical 2G HTS coil: (a) pancake coil; (b) racetrack coil

This chapter studies pancake superconducting coils both experimentally and numerically. First, a short introduction summarizes existing research in single pancake coils. Then the critical current and AC loss of several single-pancake coils are measured, and compared to simulation results based on minimization of the magnetic energy. The superconducting coil is further investigated under a DC magnetic field to simulate the critical current.

4.1 Introduction

The efficient operation of superconducting devices is highly related to the critical current and AC losses in the coils. Most superconducting coils involve a high self field or high external magnetic field. However the critical current in the coils is constrained by the intrinsic anisotropy of the magnetic field. The AC loss calculation plays an important role in the cryogenic design, and they can be calculated through current and magnetic field distribution. Therefore understanding the electromagnetic behaviour of single coil is essential for optimizing the designs of superconducting devices.

Analytical and numerical studies have been carried out and many numerical methods have been developed to simulate the electromagnetic fields of superconducting coils. Clem et al. proposed a model by dividing the superconducting region into two parts with a straight line and numerically calculating the current distribution where the magnetic field in subcritical region is minimum[43]. Once the stable state is reached, the AC loss and magnetic field cab be computed. This method was further extended by Yuan as a parabolic line was introduced to separate the critical region and the subcritical region in both infinite stacks and cylindrical coils. The critical state was reached by minimizing the magnetic field in the subcritical region.

Another method was applying the finite element method coupled with a smooth *E-J* relationship to solve the electromagnetic field of superconducting coils. Grilli compared the measured transport AC losses in YBCO coils with the *H* formula results [39]. Nguyen implemented the *H* formula to calculate AC losses for a YBCO coil with different background AC magnetic fields [98]. Zhang analysed the magnetic substrate and intrinsic anisotropy in YBCO coil behaviours, paying special attention to the determination of critical current and voltage measurement [40, 41, 99]. The third approach was established by Prigozhin who proposed an efficient method to solve the

current distribution across the superconducting region using the variation method [49, 100]. This method was considered to be efficient and fast because only the superconducting regions are computed during the process and this will reduce the mesh number. However, the prediction of critical currents and AC loss was especially difficult when taking into account the field dependency of the critical current density in the presence of external magnetic fields.

Some experimental studies have also been performed to validate the modelling methods. The research of superconducting coils using coated conductors started as early as 2006, when Polak measured the magnetic field and AC loss of a YBCO coil [101]. The following year, H. Fukushima et al. fabricated four GdBCO coils and measured the critical current in a self field [102]. Their experiments showed that the critical current is determined by the magnetic field with 45° to c-axis of GdBCO layer in the middle of the coil edge. In 2009, J Souc et al. measured the critical current of a YBCO coil under a self field with different numbers of turns, with these measurements showing good agreement with the numerical results [103, 104]. M Chudy rotated a racetrack coil under a DC field and analysed the critical current at different angles [105]. Recently, D Hu et al. characterized an epoxy-impregnated, triangle-shaped superconducting coil [106]. Although intensive research has been done on the critical current of 2G HTS coils, little attention has been paid to considering the influence of an external DC field.

4.2 Experiments

4.2.1 Critical current and AC loss under self field experiment

The coils were wound on a G10 tube with an outer diameter of 89 mm using a winding machine under constant tension, as shown in Figure 4-2. During the winding process, 4 voltage taps were soldered on the tape surface with 10-turn gaps. The voltage taps were denoted as V_0, V_3, V_4 and V_5. V_0 represented the innermost turn voltage, while V_5 denoted the voltage on the outermost turn. Figure 4-3 demonstrates the voltage tap configuration. The total length of the tape is 15.9 m.

2G HTS coated conductors (Or 2G HTS tapes) show better performance in a magnetic field, and are more cost-effective compared to their first generation counterparts. Table 4-1 summarizes the specification of the YBCO tapes used for self-field tests.

Table 4-1 Specification of a superconducting coil using SuperPower SCS4050 tape

Parameter	**Value**
I_c in self field	120A
Thickness	0.21mm
Inner diameter	89mm
Turns	50
Width	4mm

A short 20 cm piece of tape was stripped off to measure the self-field critical current before winding the pancake coil. The short sample was mounted on a G10 holder. The holder with the YBCO short sample was then placed between the two poles of an external magnetic field in a liquid nitrogen bath, as shown in Figure 3-8. The magnetic field was adjusted by controlling the current and voltage of the mangeic field generator. The magnetic field ranged from 0 T to 0.7 T. Figure 4-4 presents the critical current curve of the short sample under external magnetic field.

The critical current of the coil was measured using a control program developed based on LabVIEW and the NI data acquisition module [107]. The DC power supply was controlled by a LabVIEW interface panel, and the ramp rate of the applied current was set at 2 A/s. The upper limit voltage across the HTS coil, beyond which the ramping current would be stopped, was set at 10 times the critical voltage, so as to prevent damage to the HTS samples.

The AC losses of the coils were measured after characterization of the I_c [93]. Figure 4-5 shows the circuit diagram of the transporting AC loss measurement using the electrical method with a high accuracy data acquisition (DAQ) system. The pancake coil was supplied with an AC current using a power amplifier controlled by a signal generator. The voltage loss signal between the terminals of the coil was imposed with an inductive component that was eliminated using a cancellation coil. The voltage signal of the pancake coil after compensation was amplified and filtered to remove the noise using a high accuracy DAQ measurement system in the LabVIEW program. The transport AC loss of the pancake coil per cycle was given as:

$$Q = \frac{V_{rms} I_{rms}}{f} \qquad \text{Equation 4-1}$$

where f is the frequency, and I_{rms} and V_{rms} are the in-phase current and voltage, respectively.

Figure 4-2 The 50-turn coil with SuperPower tape for self field experiments. The inner diameter of the coil is 89 mm and the outer diameter is 110 mm.

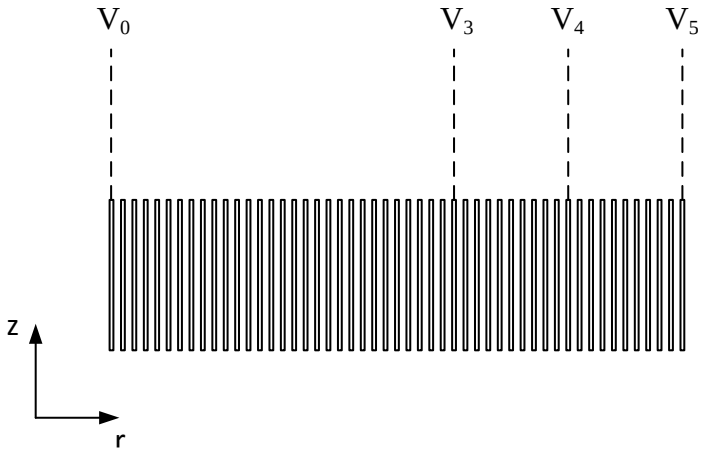

Figure 4-3 Configuration of the voltage taps. V_0 stands for the voltage on the innermost turn, while V_5 denotes the voltage on the outermost turn. Section V_0–V_3 is 8.98 m, Section V_3–V_4 is 3.25 m and Section V_4–V_5 is 3.38 m.

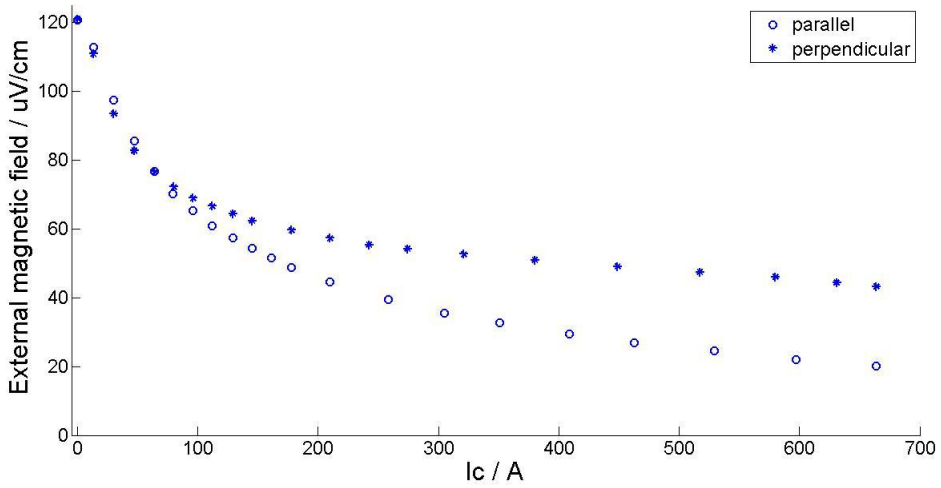

Figure 4-4 Measured critical current of the Superpower YBCO tape under an external field in the parallel and perpendicular directions.

After performing the critical current measurement and measuring the AC loss measurement of a pancake coil with 50 turns, the outer 10 turns were removed to obtain a new pancake coil with 40 turns. All the tests for critical current and AC loss characterization were repeated. Another 10 turns were then removed to produce a 30-turn pancake coil.

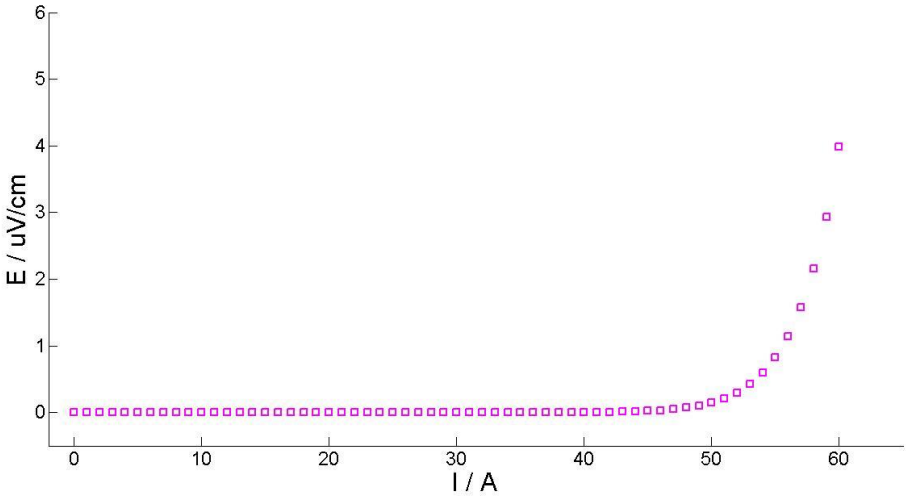

Figure 4-5 Measured *E-I* curve of the 50-turn coil.

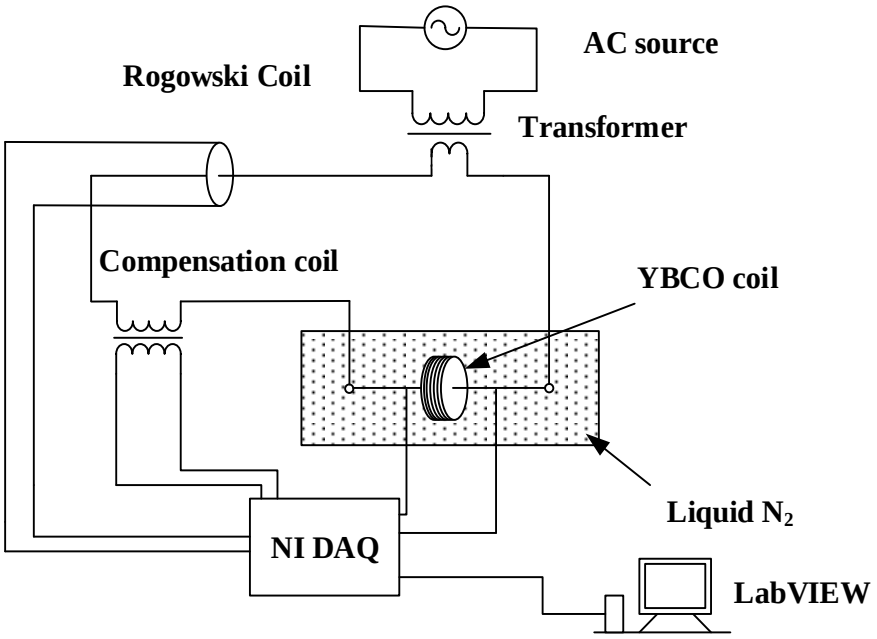

Figure 4-6 AC loss measurement circuit for the YBCO coil.

4.2.2 Critical current under external field experiment

In this part, another two pancake coils with 20 turns was prepared, as shown in Figure 4-7. One coil was made from HCN4045 coated conductors from SuNAM [91]. The other coil was wound with SCS4050 tape from SuperPower [90]. Both coils had the same geometry and winding method. The coils were wound on a G10 tube with diameter of 56 mm using a winding machine under constant tension. Two small voltage taps were soldered on both ends of the coil to measure the voltage drop along the whole coil. This *E-I* curve was used to determine the critical current of the coil. Another two voltage taps were soldered on the 5th turn and 15th turn respectively to measure the voltage drop of the inner 5 turns and the outer 5 turns. A detailed list of parameters for the coils is shown in Table 4-2.

The schematic of the magnetic field experimental set-up is presented in Figure 4-8. The pancake coil was fixed in the gap between two poles of the external magnet. The coil and the rod were connected by non-magnetic nuts. The axis of the coil was along the direction of the magnetic field, thus the coil was parallel to the external parallel field. It was challenging to ensure a homogeneous field in the rather large gap between the poles of the magnet. For this purpose, the position of the coil was carefully aligned to the axis of the cylindrical poles. Furthermore, the circumferential fields along the coil were calibrated before the experiments to make sure that the field distribution

difference was within 5%. This result was sufficiently uniform for our experiments. Given that the maximum permissible current of the electromagnet of 28 A, a maximum field of 0.54 T could be generated with only an 18 cm gap between the poles.

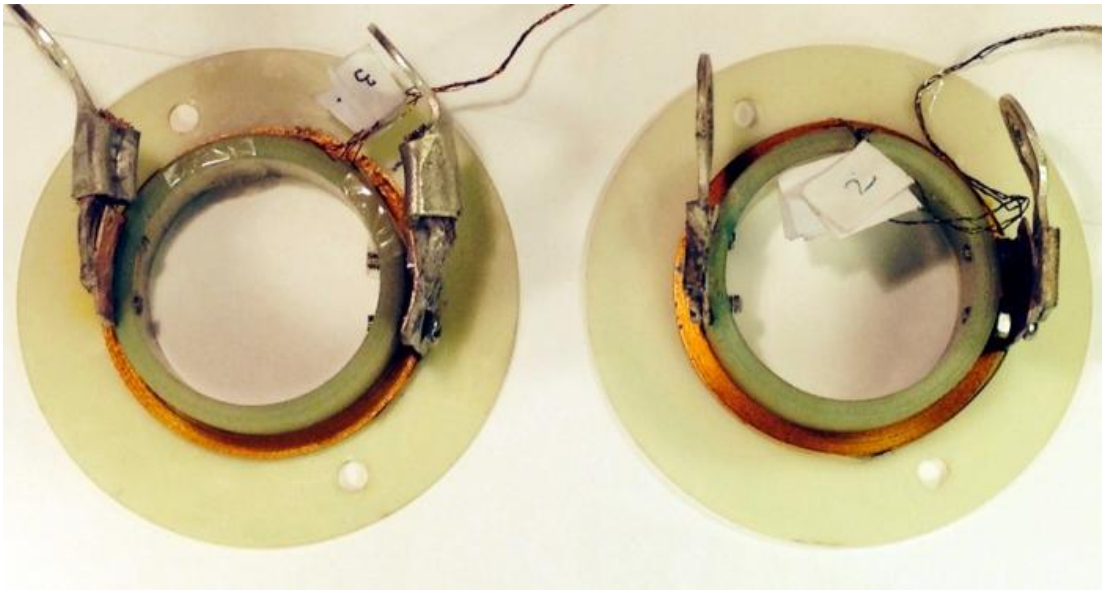

Figure 4-7 The 20-turn coils: (Left) SuNAM coil; (Right) SuperPower coil.

Table 4-2. Specification of the SuNAM and SuperPower coils.

Parameter	**SuNAM**	**SuperPower**
Tape I_c	217 A	120 A
Tape thickness	0.20 mm	0.20 mm
Inner diameter	56 mm	56 mm
Total turns	20	20
Tape width	4 mm	4 mm
Insulation	Kapton tape	Kapton tape

A liquid nitrogen bath, in which the coils were immersed, was placed between the magnet poles. The simple four-point method was used to measure the critical current of the coil with two voltage taps on both ends. A TDK-Lambda DC power supplier was used as a current source, and the voltages were acquired by an NI SCXI 1328 card. The measurement set-up was controlled by the LabVIEW program [107]. Figure 4-9 shows

the *E-I* curves of both coils under different fields. The field dependencies of these two tapes are presented in Figure 3-11.

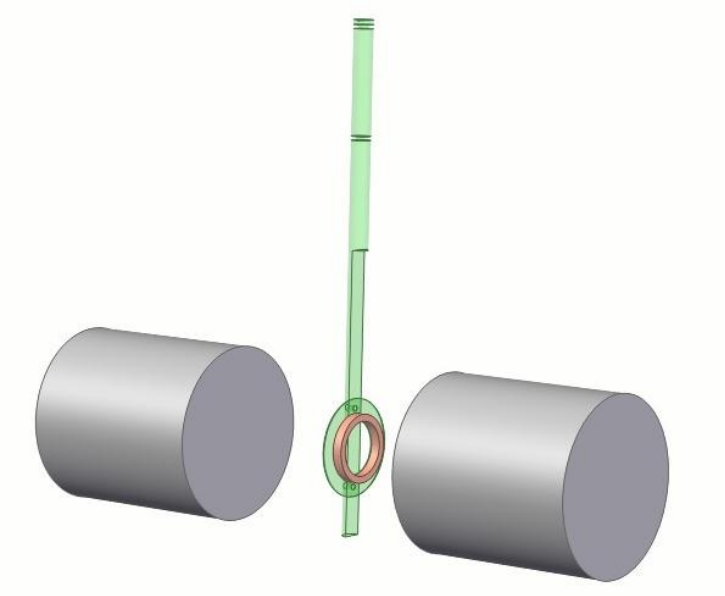

Figure 4-8 Schematic view of experimental set-up in which the cylinders represent magnet poles. The coil is fixed by non-magnetic nuts in the centre between the two magnet poles.

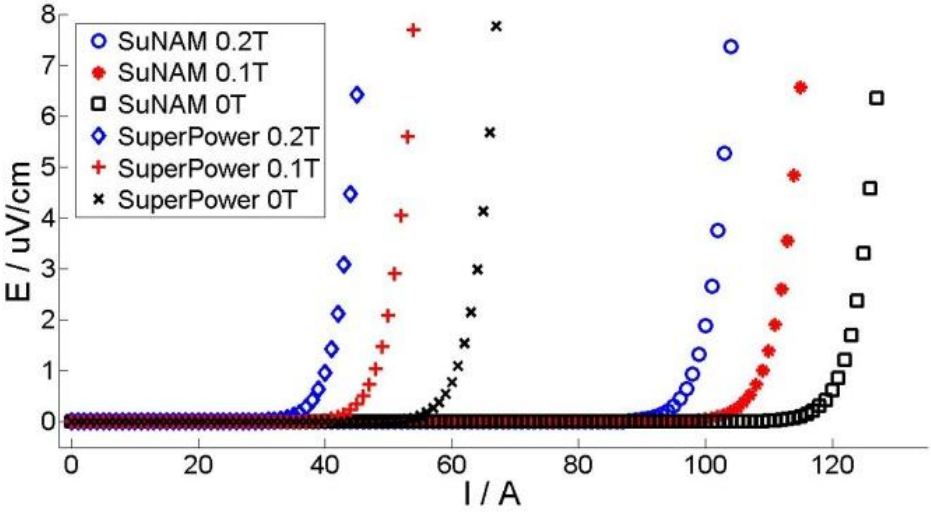

Figure 4-9 *E-I* curves under DC fields of 0.2 T, 0.1 T and 0 T for SuNAM and SuperPower coils.

4.3 Numerical model of single coils

4.3.1 Assumptions

Most commercial 2G HTS tapes has the width of 4mm and the thickness of 1 μm. This special geometry brings huge difficulty in numerical modelling using FEM. Because accurate FEM modelling requires the meshes have equal sizes in all directions. The small size in thickness means the mesh size in width is very small, increasing the mesh number greatly. Within such a narrow space of 4 *mm* by 1 μm, the current distribution can vary in the scale of 8 orders of magnitude (the current density ranging from -1e8 A/m^2 to 1e+8 A/m^2). Figure 4-10 shows the cross-section of a stack of coated tapes. The thin superconducting YBCO layers are represented by the line in the centre. This approximation refers to the sheet current model, which integrates the current across the thickness as:

$$J(z) = \int_{-\frac{w}{2}}^{\frac{w}{2}} J(r,z)\,dr \qquad \text{Equation 4-2}$$

The width of the tape is *w*. The sheet current model is especially suitable for large coil configurations for its avoidance of the 2D element in superconducting region during the simulation. This approach assumes the current in the thickness is evenly distributed, which is reasonable since the thickness is extremely small. These tapes are all separated from each other by a copper layer for simplicity, and all carry the same current, I_{app}. The thickness of the insulation is *t*.

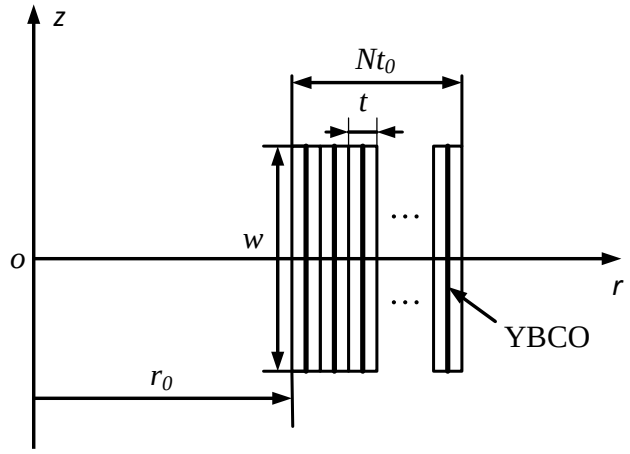

Figure 4-10 A coil of N length tapes with a width of *w* and a thickness of *t*.

This section extends Prigozhin's model from stacks of superconduting tape to cylindrical geometry and multiphysics. This model is based on Bean's critical state model, which can be used to deduce to these three conclusions:

(1) The sheet current in each tape cannot exceed the critical value, that is, $J(z,t) \leq J_c$.

(2) The electric field E_θ is equal to zero until the critical state is reached.

(3) E_θ has the same direction as J, when E_θ is not equal to zero.

Prigozhin proposed the variational method in 1997 to calculate the current distribution in bulk superconductor [48]. This method introduced the minimization of energy within superconductor to simulate the current density distribution. In 2011 Prigozhin extended this model to stacks of 2G superconducting tapes using the sheet current model and gained good results.

This model has many advantages compared to other differential models. Firstly, the sheet current model exploits the variational method to transform a complicated physical problem into a mathematical problem that is simple and easy to solve. Secondly, since it uses the sheet element to replace the extremely small elements in the *H*-formula, the sheet current model speeds up the calculation dramatically. Finally, when compared to other homogenous models, the sheet current model can be easily extended to simulate the multiphysics coupled field.

4.3.2 Implementation of single coil modelling

Based on these hypothesis, in each tape we have [49]:

$$\int E_\theta \left(J' - J \right) \leq 0 \qquad \text{Equation 4-3}$$

where J' is the testing current function.

According to Maxwell theory, the electric field E and magnetic vector A can be calculated:

$$E_\theta = -\frac{dA}{dt} - \nabla V \qquad \text{Equation 4-4}$$

$$A(r',z') = \frac{\mu_0 J(r,z) S}{\pi k}\left(\frac{r}{r'}\right)^{\frac{1}{2}}\left[\left(1-\frac{k^2}{2}\right)K - E\right] \qquad \text{Equation 4-5}$$

$$k^2 = \frac{4rr'}{d^2+(r+r')^2}$$

where r is the distance between two points, S is the element area, $d = z - z'$, and K and E are complete elliptic integrals of the first and second kind.

Bring Equation 4-4 and Equation 4-5 to Equation 4-3 and apply the variational process, we can reach this equation:

$$\min \sum_{i\in\Omega}\left(\frac{1}{2}A_i^m + f_i^m + \tau C_j\right)J_i S$$

$$\text{for each tape: } \int_{-w/2}^{w/2} J_i dz = I_{app} \qquad \text{Equation 4-6}$$

$$\text{for all the elements: } J_i \le J_c(B_r, B_z, T, \varepsilon)$$

where M is the mutual inductance matrix derived from the Green integral function [108, 109], Ω is the set of all elements, A_i and J_i are the vector potential and current in the circumferential direction in the ith element, $f_i^m = -A_i^{m-1}$, C_j is the voltage due to the source in the jth tape, and $J_c(B_r, T, \varepsilon)$ is the critical current density with field dependencies. This equation can be optimized by iterations and is implemented using the constrained quadratic minimization function in MATLAB [110].

The critical current density of superconducting tape is highly dependent on the surrounding multiphysics fields. This field dependency plays an important role in the current transporting abilities of the tape. These models are incorporated in the calculation:

Magnetic field dependency model at 77K:

$$J_c(B_r, B_z) = \frac{J_{c0} B_0}{B_0 + \sqrt{\left((B_r)^2 + (kB_z)\right)^2}} \qquad \text{Equation 4-7}$$

Thermal dependency model:

$$J_c\left(B_r,B_z,T\right)=\begin{cases} J_c\left(B_r,B_z,T_{ref}\right)\dfrac{\left(T_c-T\right)^{\alpha}}{\left(T_c-T_{ref}\right)^{\alpha}}, & if\ T_{ref}<T<T_c \\ 0, & if\quad T_c<T \end{cases} \qquad \text{Equation 4-8}$$

where T_c=88 K, and T_{ref}=77 K, which is the operating temperature, and α = 1.5 [111].

Strain dependency model:

$$J_c\left(B_r,B_z,T,\varepsilon\right)=J_c\left(B_r,B_z,T\right)\left(1-ac\left|\varepsilon\right|^b\right) \qquad \text{Equation 4-9}$$

for a YBCO tape under tension at 77 K, $\varepsilon \ll 1$, ac=3397, and b=1.9 [112].

After the current density distribution is calculated, the electric field E in each tape can also be calculated:

$$E_i=-\frac{dA_i}{dt}-C_j \qquad \text{Equation 4-10}$$

where E_i is the electric field in circumferential direction for the ith element.

Then the AC loss in the coil can be integrated:

$$Q=2\pi S\sum_t\sum_i E_{i,t}J_{i,t}r_i\Delta t \qquad \text{Equation 4-11}$$

where $E_{i,t}$ and $J_{i,t}$ are the electrical field and the current density for the ith element at the time of t, r_i is the radius of the ith element, and Δt is the time taken for one step.

The above model provides the current distribution in the superconducting region, which is the central issue in simulating superconductivity. However, a finite element analysis (FEA) is still required to calculate the electromagnetic, thermal and mechanical fields. The FEA can be considered to be an approximation to the real fields. The error between the FEA approximation and the real field distribution can be safely ignored. There are five typical steps in a FEA simulation. Firstly, the whole space should be meshed into small elements. Then a trying field function should be specified for each element, followed by derivation of the shape function for all elements. In our simulation, the linear element was chosen as the trying field function. That means in each element, the field can be represented by:

$$u = \begin{bmatrix} N_i & N_j & N_k \end{bmatrix} \begin{bmatrix} u_i \\ u_j \\ u_k \end{bmatrix} \quad \text{Equation 4-12}$$

where u is the field variable, N_i, N_j, N_k is the shape function of the certain point, and u_i, u_j, u_k is the field parameter. Thus the stiffness matrix can be yielded for every element from the control PDEs. The PDEs for each element can be transformed to the matrix format:

$$ku = f \quad \text{Equation 4-13}$$

where k is the element stiffness matrix, and *f* is the external source or external force. Through variational methods, *k* can be expressed by:

$$k_{ij} = \int \nabla N_i \cdot \nabla N_j dxdy \quad \text{Equation 4-14}$$

Assembling all the k_{ij} and *f* variables according to their positions produces the global stiffness matrix, and the control PDE can be represented as:

$$KU = F \quad \text{Equation 4-15}$$

where K, *U* and *F* stand for the global stiffness, global field vector and global force vector. Finally, the field variable can be found by matrix operations:

$$U = K \backslash F \quad \text{Equation 4-16}$$

This is the general process for FEM modelling. Different fields have different control partial differential equations and different state variables. For a 2D electromagnetic field, the control equation is related to Ampere's law:

$$\nabla^2 A = \mu_0 J \quad \text{Equation 4-17}$$

The magnetization flux density *B* can then be calculated by curl of magnetic vector potential:

$$\nabla \times A = B \quad \text{Equation 4-18}$$

The thermal field of the coil under operation is of significant importance for quench protection. The governing equation for heat transfer in 2D is the Fourier equation [11]:

$$C \frac{\partial T}{\partial t} = k_1 \nabla^2 T + E_\theta \cdot J \quad \text{Equation 4-19}$$

where *T* is the temperature, *C* is the heat capacity, k_1 is thermal conductivity, and $E_z \cdot J$ represents the AC loss during the varying current process.

The Lorentz force can be analysed to ensure the mechanical stability of the magnet. The mechanical force field, due to the electromagnetic field, is calculated using FEM. Similarly, for a mechanical field, the control PDE has the shape:

$$-\nabla \cdot \sigma = J \times B \qquad \text{Equation 4-20}$$

where σ is the stress tenor in the coil, J is the current density in the section area, and B is the local magnetic flux density.

The whole calculation process is presented in Figure 4-11. During the multiphysics modelling, the first step is to calculate the current distribution along the tapes. Then the results are applied in FEM to simulate the magnetization flux across the substrate section. Finally, the thermal and mechanical fields are calculated with the solved current and magnetization flux distribution, respectively.

Considering the boundary condition, it is assumed that the outer air boundary of the area is magnetically insulated. The applied current is in the shape of sine wave. For thermal and mechanical simulation, the field value on the boundary of the coil is fixed, which means that the temperature of the boundary is fixed and the axial and radial displacements are equal to zero. The stabilizer is assumed to be copper, for which the specific heat capacity and thermal conductivity are 6.23e5 *J/(m^{3}K)* and 1100 *W/(mK)*, respectively [113].

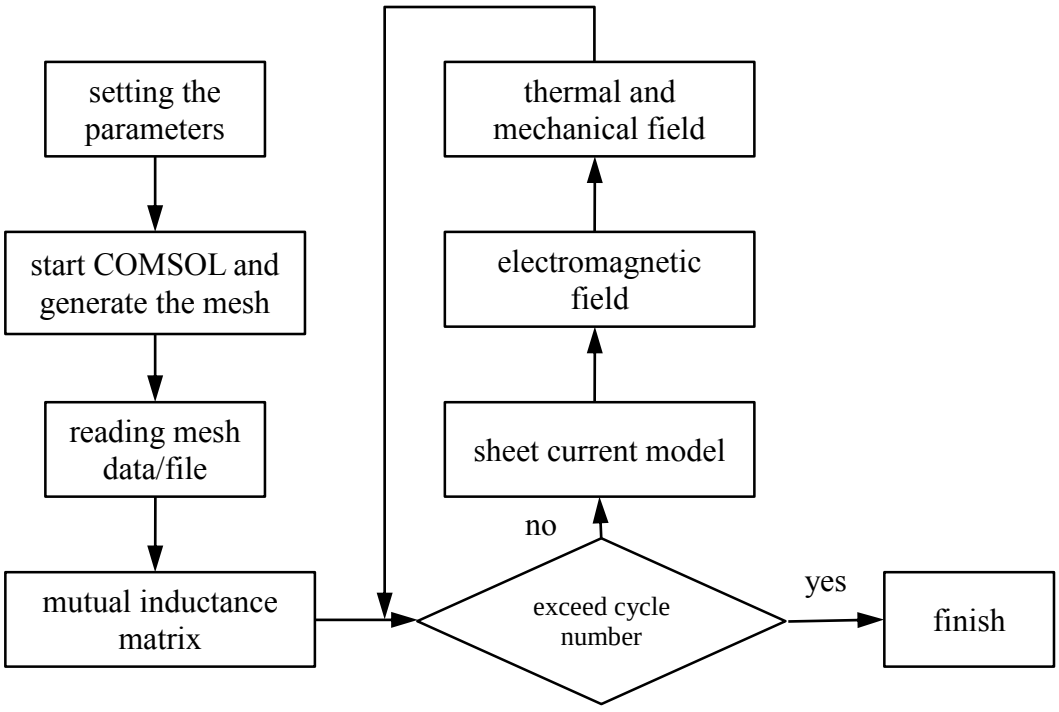

Figure 4-11 Flow chart of direct-coupled multiphysics modelling based on the sheet current model.

4.4 Results analysis under self field

We compared the numerical results with experimental measurements to verify the model. This verification includes two parts. First, the critical current of the coils with different turns are discussed, followed by the discussion of AC losses.

4.4.1 Critical current

Similar to a superconducting tape, we can measure the electric field across the superconductor when continually ramping up the current, commonly known as the *E-I* curve, as shown in Figure 4-5. The critical current is usually defined before the voltage reaches a certain value, such as 1 $\mu V/cm$, *0.5* $\mu V/cm$ and *0.1* $\mu V/cm$ [114].

In our simulation, we applied a linearly increasing current in each tape, and checked the current distribution in each turn step by step. When one of the tapes was fully penetrated with a certain applied current, the calculation was stopped and this applied current was considered to be the critical current of the coil, as shown in Figure 4-12 (b).

Table 4-3 compares the modelling results with the experimental measurements. The simulations provided a good estimate for the critical current of the superconducting coils. The simulations taking the value of J_c from Equation 3-14 showed excellent agreement with the criterion of 0.5 $\mu V/cm$. The maximum discrepancy between the experimental results and simulated critical current was 2.7% when the coil had 30 turns.

The popular criterion for experimental I_c determination is 1 $\mu V/cm$. The simulated I_c tended to estimate a lower the critical current than the more accepted criterion of 1 $\mu V/cm$. However, it has been reported that 1 $\mu V/cm$ is a too high criterion to define the coil critical current for long term safe operation [99]. Our simulation technique is conservative and hence safer estimation of the critical current for coils.

To further understand the behaviour of the coils during the ramping up process, we took a 50-turn coil as an example. A varying current with a sine shape was applied to the coil with a peak amplitude of 50 *A*. The frequency of the applied current was 1 *Hz*. Figure 4-13 shows the current distribution within the coil for four time steps: 15 *A*, peak current 50 *A*, -15 *A* and 0 *A*. Each line represents one tape and the *z* axis is the magnitude of the current density for the thickness of 1 μm.

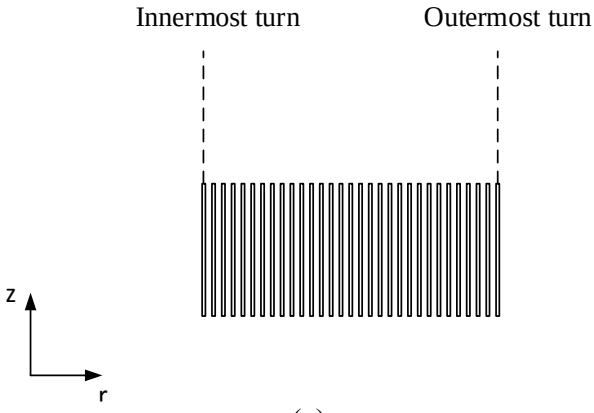

(a)

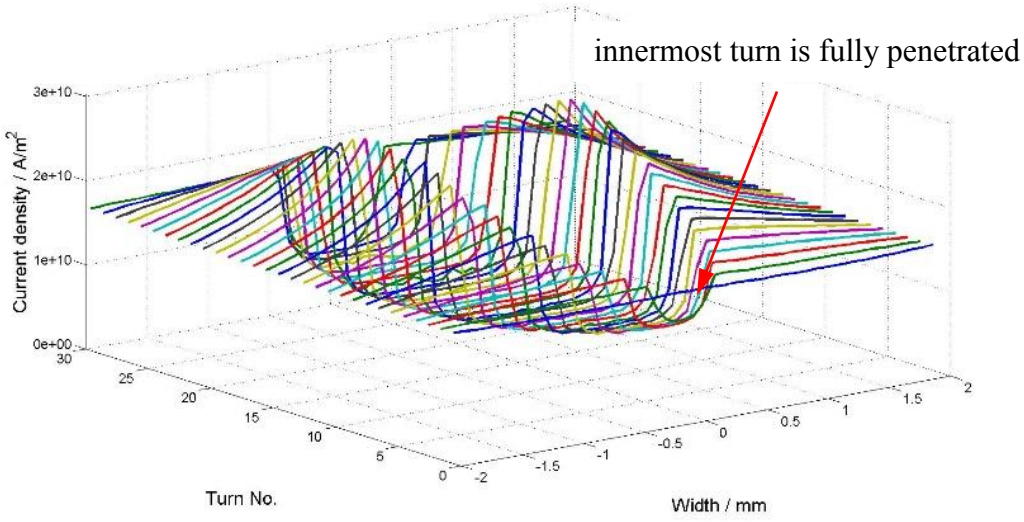

(b)

Figure 4-12 (a) The cross section of the 30-turn coil; (b) When the applied current is 59.0 *A* in the 30-turn coil, the innermost turn is fully penetrated. The critical current of the coil is thus defined as 59.0 *A*.

Table 4-3 The critical current of different coils by experiment and calculation

Turns	50	40	30
Experimental (0.5 $\mu V/cm$) (A)	53.5	54.8	58
Simulated (A)	53.1	55.0	59.0
Experimental (1 $\mu V/cm$) (A)	55.6	57.3	60.3
Load line calculated (A)	53	56	59

Figure 4-13(b) clearly shows two regions in the superconducting parts: the penetrated region and the unpenetrated region. These are also denoted as the critical region and the subcritical region, consistent with the assumptions made by Clem [43]. The penetration region extends from both ends into the central region. In the penetrated region, the

current density is bounded by the critical current density. As previously mentioned, the critical current decreases in external field, and showing as a clear slope of current density in the penetrated region. In Figure 4-13(d), the total applied current in each tape is zero, however, the current density is not homogenously zero as there is both positive and negative current within the region. This shows the hysteretic nature of the superconductivity after magnetization.

To clearly show the field dependency on the magnetic field, the magnetic field and flux line of the same time step are presented in Figure 4-14. The colour represents the magnitude of the magnetic flux density, while the contours show the isolines of vector potential. According to the magnetic field contours and directions, the strong magnetic field locates in the innermost turn, called the weak turn. This explains that the innermost turn is the first tape to be fully penetrated, as shown in Figure 4-12, and the innermost turn determines the critical current of the coil. Also, we can find that the innermost turn and the outermost turn are more penetrated and this makes the separation between the critical region and subcritical region as a parabola, which is the assumption of Yuan's paper [44]. From Figure 4-14, we can also find that the magnetic field is smaller than 0.15T, thus, Kim model can well fit the field dependency as shown in Figure 3-13.

From Figure 4-14 shows that only B_z exists in the subcritical region (the magnetic field is parallel to the tape width direction). This is due to the intrinsic property of a superconductor, which expels the magnetic field. This is consistent with Yuan's paper which solves the electromagnetic field by minimization of $(B_r)^2$ across the subcritical region [44].

4.4.2 AC loss

First we measured the transporting losses of different coils at two frequencies. We limited the maximum current to 50 A for safety considerations, and decreased the current in steps to 5 A. These measurements were done at the frequencies of 30 Hz and 40 Hz. Figure 4-15 shows the losses measured with the voltage contacts soldered at both ends of the coils. For certain coils, we found that different frequencies have similar AC losses per cycle, confirming the hysteretic nature of the loss. Figure 4-16 compares the losses between measured results and simulated results. The simulated results using a Kim-law model show good agreement with the experimental results.

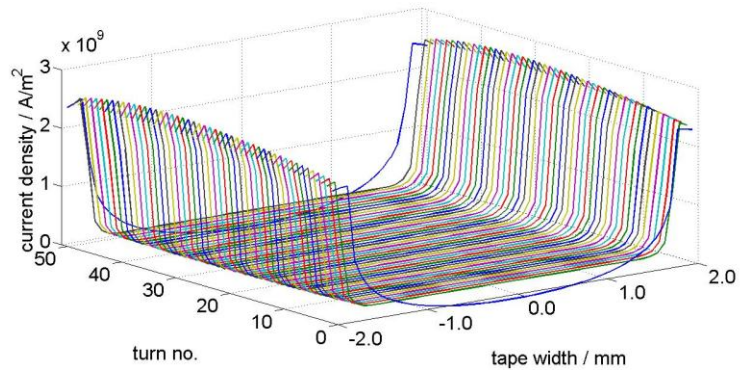

(a)

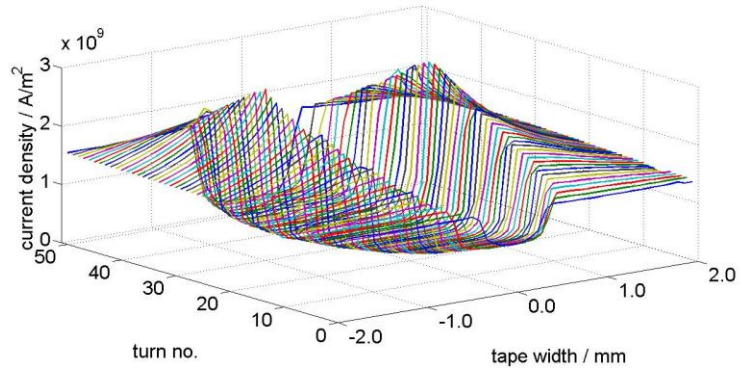

(b)

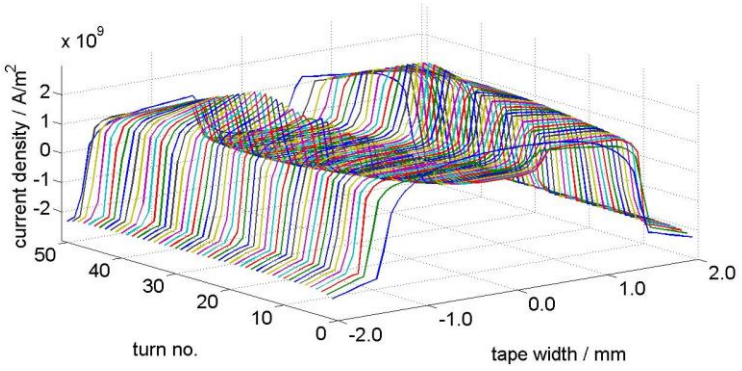

(c)

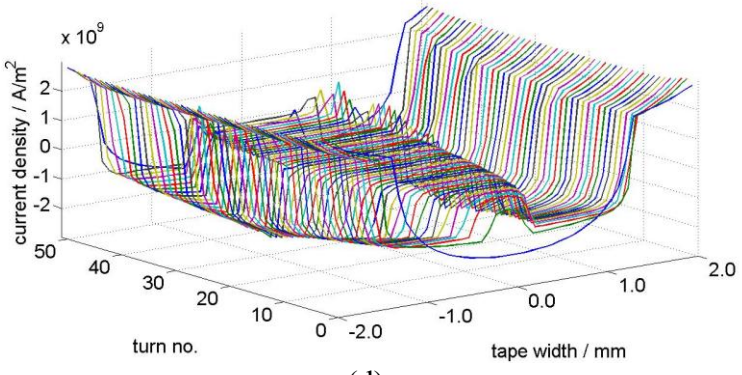

(d)

Figure 4-13 Current distribution for 50 turns at: (a) ramping up to 15 A; (b) ramping up to 50 A; (c) ramping down to 15 A; (d) ramping down to 0 A.

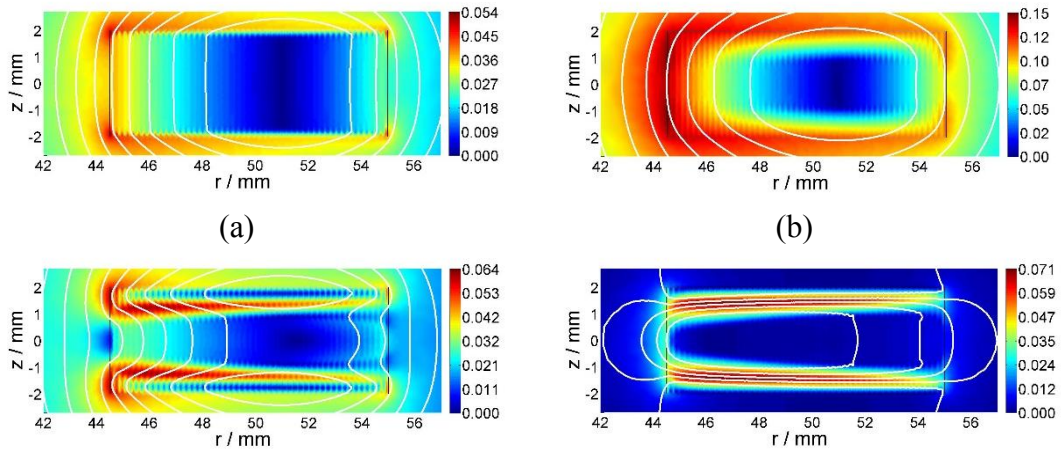

Figure 4-14 Magnetic field distribution and flux line plot of a 50-turn coil at: (a) ramping up to 15 A; (b) ramping up to 50 A; (c) ramping down to 15 A; (d) ramping down to 0 A. The rectangle with the black line represents the region occupied by superconductors. (unit: T)

Figure 4-17 presents the transporting loss per unit length in the coil, compared to the analytical results by Norris. The losses increased continuously when the number of turns in the coils increased. These results confirm the fact that the more the turns, the larger the magnetic field, and thus the larger the magnetization loss. The losses increased almost linearly with the applied current and the curves show a similar power exponent in log-log scale plot and the slopes are between 2.8 to 3.1 in a wider range of measured peak current, near a cubic behavour. These curve slopes indicate a good agreement with the loss curve of a superconducting strip predicted by the Norris equation [28].

Although we can measure the total AC loss of the coils by soldering the voltage tap in both ends, it is very difficult to understand further details about the AC loss in different turns. The simulation technique is a powerful tool to explore the behaviour of different turns. This is very important for thermal design, as greater cooling power is required in the region with higher AC loss density which can lead to high risk of a quench.

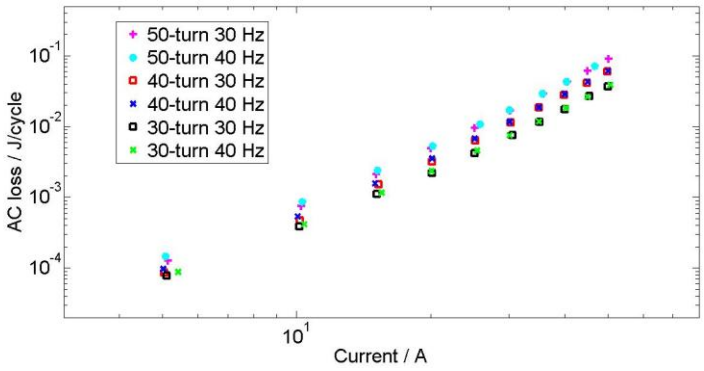

Figure 4-15 Measured AC losses of three different coils under 30 Hz and 40 Hz transporting current.

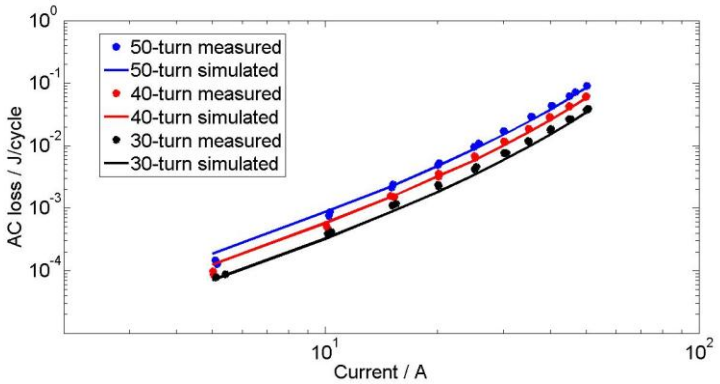

Figure 4-16 Measured and calculated AC losses of three different coils.

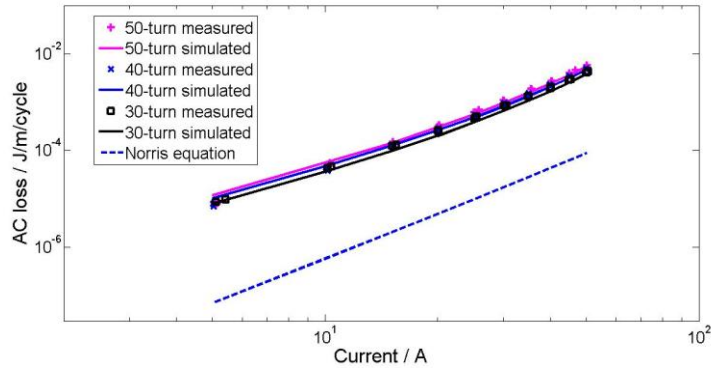

Figure 4-17 Comparison of measured, simulated and calculated AC loss per unit length.

We applied different currents to a 50-turn coil and plotted the AC loss for each turn as shown in Figure 4-18. It can be observed that for the same geometry, different currents have different loss distributions. Although the transporting current is the same in each tape, the total loss is quite different, meaning the magnetisation loss plays the major part. As the magnetic field across the section is quite different, this will lead to different loss distribution. When the applied current is small (below 20 A), the turns at

the boundaries have higher losses and the turn with the smallest loss is located in the middle region. This is because when current is small, the innermost and outermost turns are more penetrated and have more losses. When the applied current increases to 35 A, the loss tends to decrease linearly from the innermost turn to the outermost turn. In this situation, the magnetic field in the middle region increase more quickly than the outermost turn, leading to higher losses in the middle turns than the outermost turn. When the current increases further, the losses increase initially and then decrease from turn 1 to turn 50, as shown in Figure 4-18(d). When the innermost turn is further penetrated, the magnetic field will decrease the current and decease the losses. Thus the tape with highest loss moves to the tapes in the middle region.

Figure 4-19 presents the AC losses for a unit length of each turn. The loss distribution is very similar to that shown in Figure 4-18 with different transporting currents. The turns with the highest loss and lowest loss vary. The highest loss turn changes from the innermost turn to the middle turn, while the smallest turn moves from the middle region to the outermost turn. A comparison of Figure 4-18(d) and Figure 4-19(d) show that the turn with the highest loss differs slightly. In the first graph, turn 8 is the peak turn, whereas in the second picture, turn 7 is the peak turn.

In order to analyse the influence of geometry on the peak loss turn location, Table 4-4 presents the peak loss turn with coils ranging from 10 turns to 50 turns. When the applied current is 50 A, for the 10 turn and the 20 turn coil the innermost turn is the peak loss turn, while for the 30 turn, 40 turn and 50 turn coil, the peak loss turn is turn 5, turn 7 and turn 8, respectively. The peak loss turn changes when considering tape length.

Figure 4-20 shows the instantaneous AC losses varying with time during two AC cycles. At the beginning the instantaneous loss power is zero, and then the loss goes up as the current increases. However, the loss reaches its first peak before the current peaks. This is because when the current peaks its derivation with time is zero and means electric field minimizes. So the product of current density and electric field, which is defined as the loss, reaches maximum before the current peaks. After the first loss peak, the second loss peak of loss appears in the second half of the cycle. The second peak of the loss is larger than the first peak. This is because the first peak

begins from the virgin state while the second peak begins with the reversed current as shown in Figure 4-13(d).

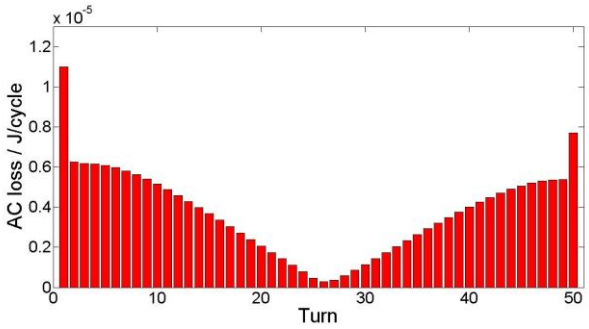

(a) Transporting current is 5A

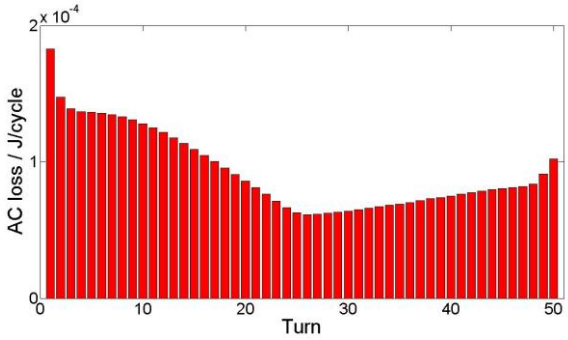

(b) Transporting current is 20A

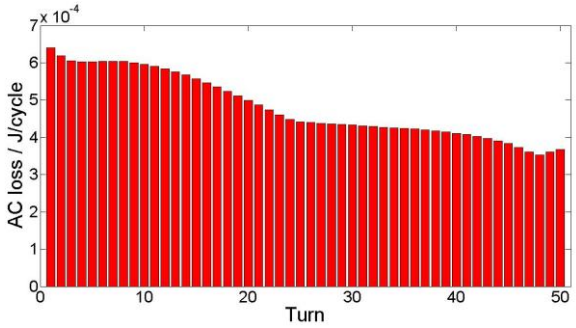

(c) Transporting current is 35A

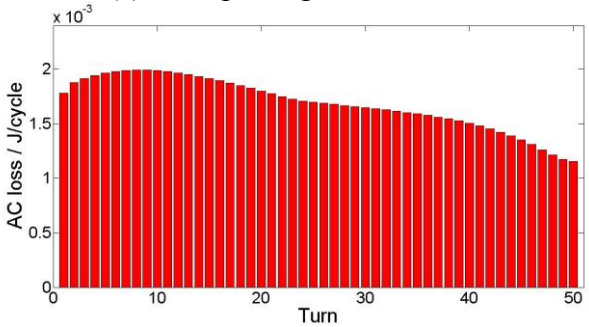

(d) Transporting current is 50A

Figure 4-18 AC losses for each turn in a 50-turn coil during one cycle with different applied currents: (a) 5 A; (b) 20 A; (c) 35 A; (d) 50 A. Turn 1 denotes the innermost turn and Turn 50 is the outermost turn.

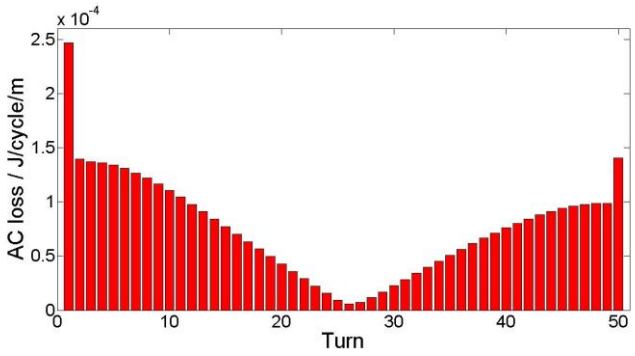

(a) Transporting current is 5 A

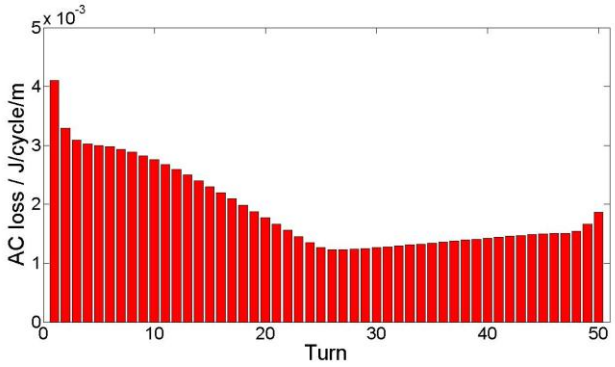

(b) Transporting current is 20 A

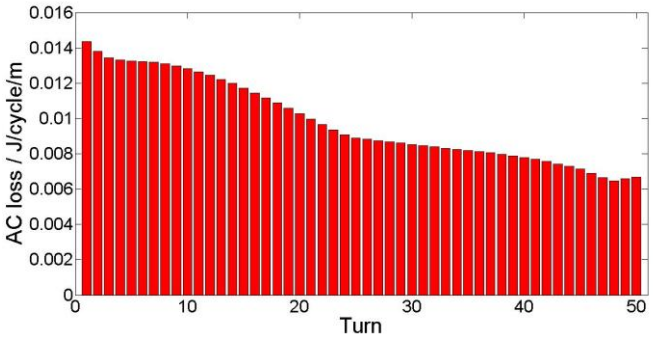

(c) Transporting current is 35 A

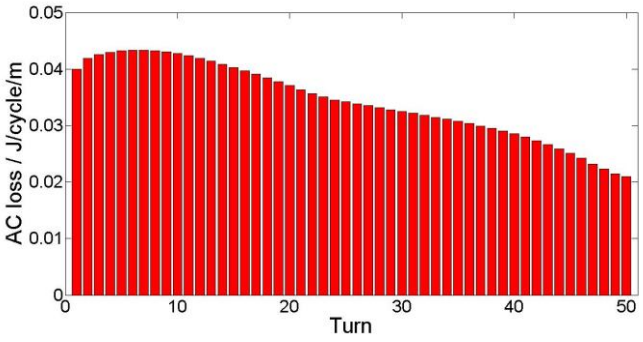

(d) Transporting current is 50 A

Figure 4-19 AC losses per turn per metre in a 50-turn coil during one cycle with different applied currents: (a) 5 A; (b) 20 A; (c) 35 A; (d) 50 A. Turn 1 denotes the innermost turn and Turn 50 is the outermost turn.

Table 4-4 The turn number with peak loss in different geometries.

Coil geometry	Turn number with peak loss	Turn number with peak loss per length
10 turn	1	1
20 turn	1	1
30 turn	5	2
40 turn	7	6
50 turn	8	7

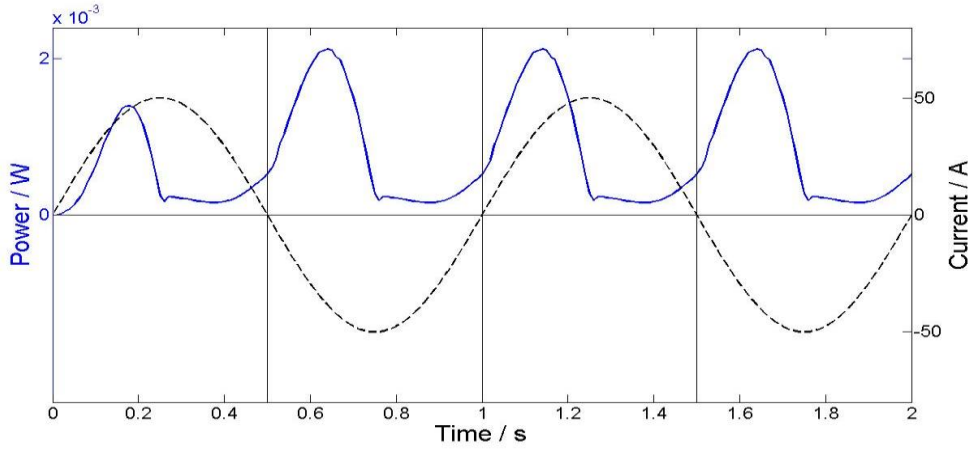

Figure 4-20 Instantaneous AC losses during the first two cycles.

4.4.3 Temperature and stress distribution

Figure 4-13 shows that the current density in the tape is very uneven. The outside region reaches the critical state quickly and generates an AC loss while the middle region remains subcritical until it is penetrated. This is the mechanism of heat generation in the coil during charging and discharging, which can be evaluated by considering the distribution of current density.

Figure 4-21 presents the thermal source and the temperature distribution along the cross-section. From Figure 4-21 (a), the heat is generated along the tape in the critical state region while no heat is generated in the subcritical region, which can be confirmed

by Figure 4-13. Figure 4-21 (b) presents the temperature distribution in the coil section after 100 cycles' charging and discharging. The contours of the temperature have a hyperbolic shape because the temperature of the node on the boundary is fixed at 77 K, and the heat exists at the outside end of the tape.

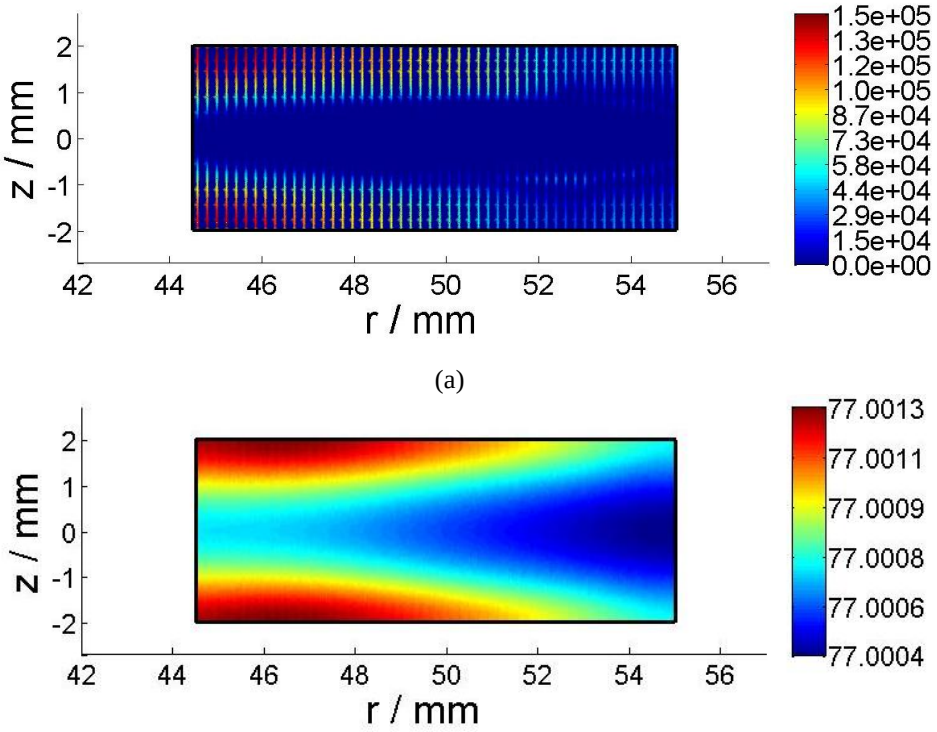

Figure 4-21 Thermal source across the superconductor section when the current peaks at 50A (the unit is W/m^3) (b) Temperature distribution across the superconductor section after 100 cycles' charging and discharging (the unit is K).

The mechanical stress in the coil is mainly due to Lorentz force. Figure 4-22 presents the von Mises stress distribution along the cross-section when the current is at peak value of 50 A. The strongest axial direction field component in the middle of coil produces a maximum outward radial force on the conductors, which causes a maximum radial and circumferential hoop stress in the HTS wire. Evaluation of the maximum stress during charging and discharging process is especially important in order to prevent the destruction of the HTS wire.

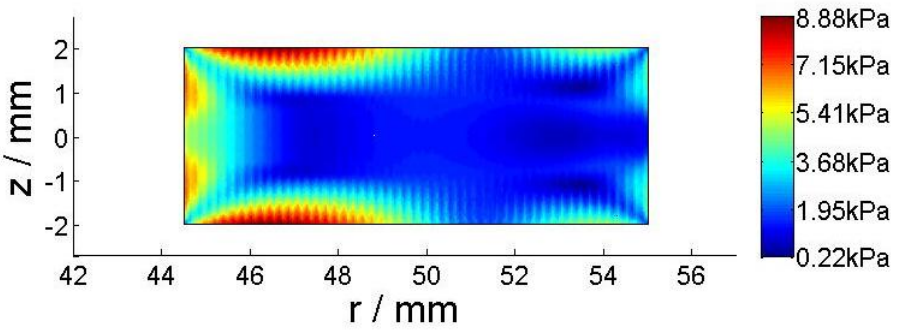

Figure 4-22 von Mises stress distribution across the superconducting section when the current peaks.

4.5 Results analysis under an external field

4.5.1 Critical current validation

Figure 4-8 presents the setup of external magnetic field. In this section, only the influence of a parallel field, H_z, on the coil critical current is studied. There are two types of external magnetic field. The in-phase field is defined while the background field is in the same direction as the self-field of the HTS pancakes as shown in Figure 4-23(a), and the anti-phase field H_z has the opposite direction to the self-field inside the pancakes as shown in Figure 4-23(b). Here we selected the criterion of 0.5 $\mu V/cm$ to define the critical current of the coils, as shown in Figure 4-24. The results shows that the simulations provide a good estimation of the critical current of the superconducting coils.

Both the experiment and simulation showed that the coil critical current decreased linearly when the in-phase external field increased in Figure 4-24. This is because the background field combined with the self field reduces the critical current of the innermost turn. However, the situation is quite different for an anti-phase external field. While the magnitude of anti-phase external field is increasing from 0, the critical current of the coil is initially increased and then decreased. This is because the self-field produced by the coil is cancelled by the external field, thus the total field is lower compared to in a same magnitude of the in-phase field. If the magnitude of the anti-phase external field increases further, the critical current begins to decrease, because the overall field starts to increase again.

The existence of the external field also changes the current penetration pattern. The results from the simulation showed that under the in-phase field, the critical current is determined by the innermost turn, which is the first to be fully penetrated as shown in Figure 4-26. On the other side, the anti-phase external field shifts the weak turn position from the innermost to the outermost turn when the magnitude of the external field exceeds 0.04 T. This shifting can also been verified by measuring the *E-I* curve. Figure 4-27 presents the measured voltages on different sections under an external field of -0.2 T. The voltage within the inner 5 turns rises earlier than the outer 5 turns under an in-phase field, while voltage of the outer 5-turns rises earlier under an anti-phase field. This coincides with the simulation results.

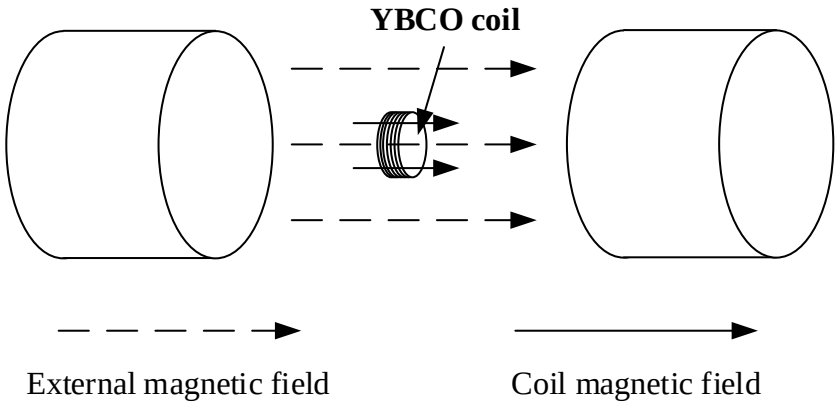

(a)

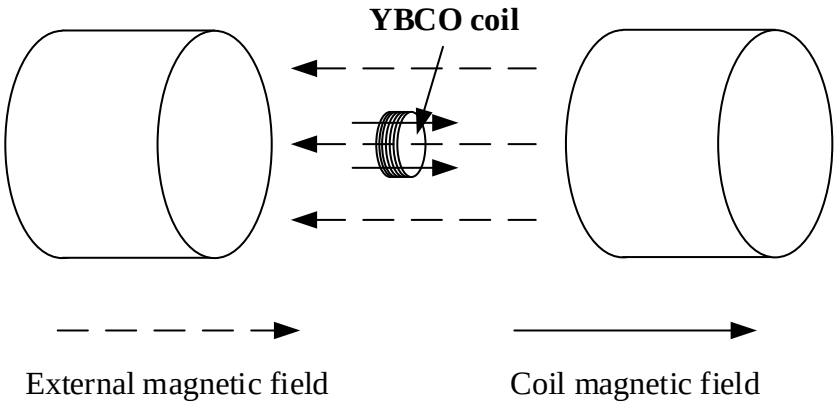

(b)

Figure 4-23 Definition of external magnetic field: (a) in-phase (b) anti-phase [99].

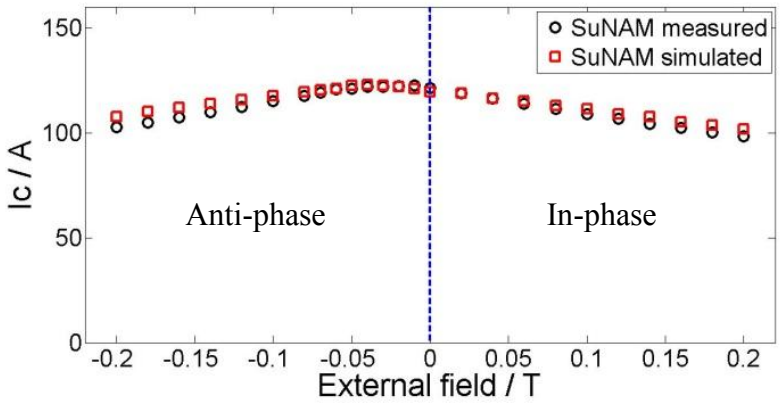

(a)

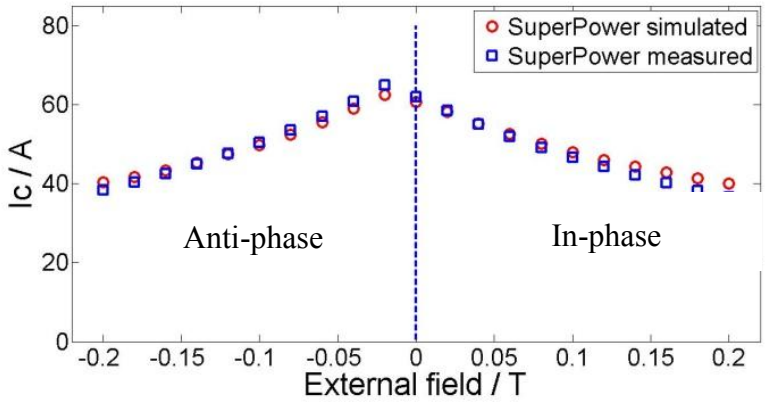

(b)

Figure 4-24 Comparison between measured and simulated critical current for (a) SuNAM and (b) SuperPower coils with 20 turns in different external fields. The measured critical currents are defined by 0.5 μV/cm in the *E-I* curves.

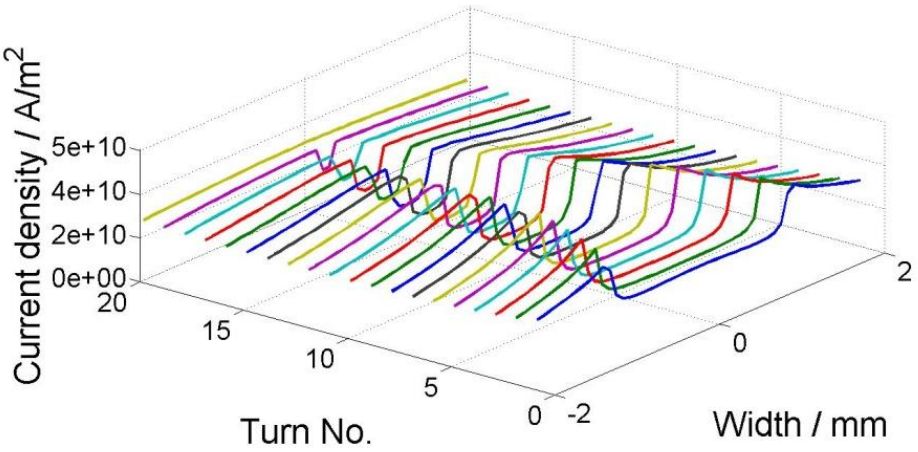

Figure 4-25 When the applied current was 107.5 A, and the external field was anti-phase 0.2 T, the outmost turn of the SuNAM coil, turn 20, was fully penetrated. This current was defined as the critical current of the coil. This method is referred to as the penetration method in the following section.

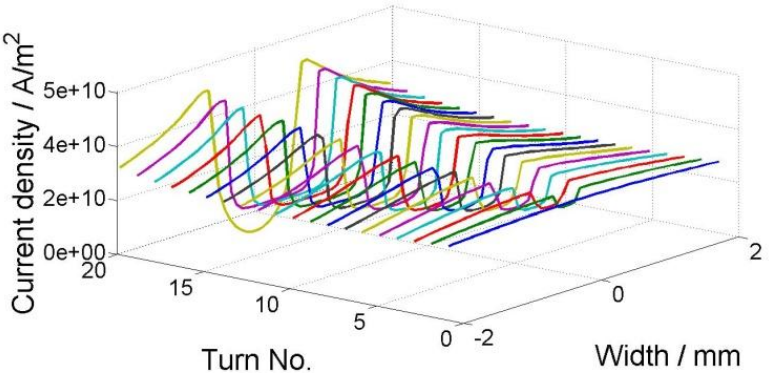

Figure 4-26 When the applied current is 101 A and the external field is in-phase 0.2 T, the inner turn of the SuNAM 20-turn coil is fully penetrated.

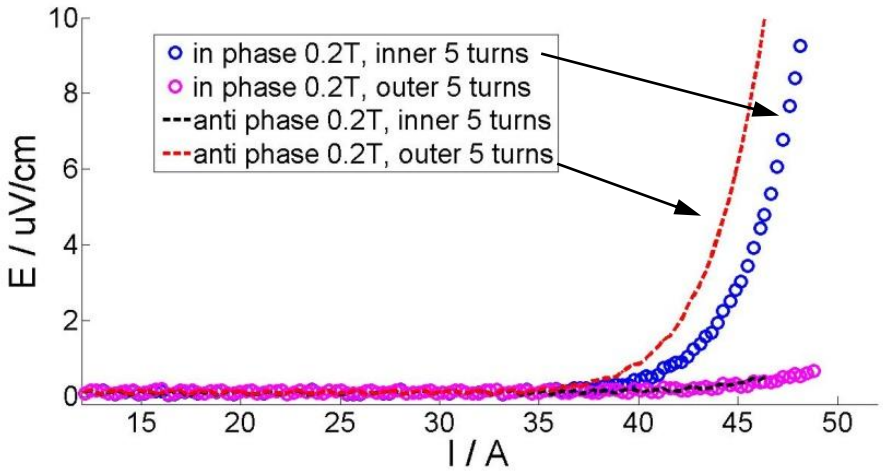

Figure 4-27 *E-I* curves of different sections of the SuNAM coil with in-phase and anti-phase 0.2 T magnetic fields.

4.5.2 Comparison of two coils with different tapes

Recently, SuperPower has made progress on YBCO tape fabrication, which shows a different magnetic field dependency. The old tape has a smaller critical current when the external field is perpendicular to the field than that when the same amount of field is parallel to the tape. However, this new tape has an opposite dependency, meaning that the perpendicular field has a larger critical current, as shown in Figure 3-11. This wire is an AP (Advanced Pinning) type which has zirconium doping to form $BaZrO_3$ nanocolumnar particles in the film. These $BaZrO_3$ nanocolumns are aligned in parallel to the c-axis of REBCO with the result that the flux pinning for H//c is greatly enhanced. When the pinning from the nanocolumns is strong enough, the I_c(H//c) becomes higher than the I_c(H//ab).

It is, therefore, of practical interest to analyse the difference when this new SuperPower tape is used in pancake applications under a DC magnetic field compared to tape with a normal magnetic field dependency, such as SuNAM tape. This field dependency is approximated by a modified Kim model which is shown in Equation 3-14.

This new tape was incorporated into the numerical model and compared to the critical current under a DC field with the SuNAM coil as presented in Figure 4-24(a). In order to compare the performance of coils consisting of different tapes, both models had the same geometry, and the critical current of the tapes was normalized by the critical current under a self field. Figure 4-28 shows the simulated critical current under a DC field. A similar trend was seen for the critical current with an external field. That is, the anti-phase field increased the critical current first.

However, the difference in the critical current is also obvious, that is, the SuperPower coil has a lower critical current. Under a self field, the critical current difference for these two coils is 14%, while this difference increases to 18% when the external field is 0.2 T. The reason for this is that the weak turns for these two coils are either innermost turn or outermost turn, which have a large parallel field. As SuperPower is more sensitive to a parallel field, the critical current is smaller than the tapes which are less influenced by a parallel field, such as a SuNAM coil. Figure 4-29 presents the perpendicular and parallel components of the self field of a coil with an applied current of 100 A. This graph verifies that the average parallel field is larger than the perpendicular field where a weak turn appears. The existence of a parallel external field decreases the critical current further for a SuperPower coil, which may not be good for applications such as insert coils in high magnetic field devices.

4.5.3 Extension of load line

The performance of a coil winding with a low temperature superconductor is usually characterized by means of a diagram like that shown in Figure 4-30 [75], which is called the load line method. This method is employed in magnet design for its simple implementation and straightforward physical image. The straight line, usually known as the “load line”, represents the peak field as a function of the transporting current. The intersection point between this load line and the in-field critical current line of the superconductor is thus the expected critical current of the coil.

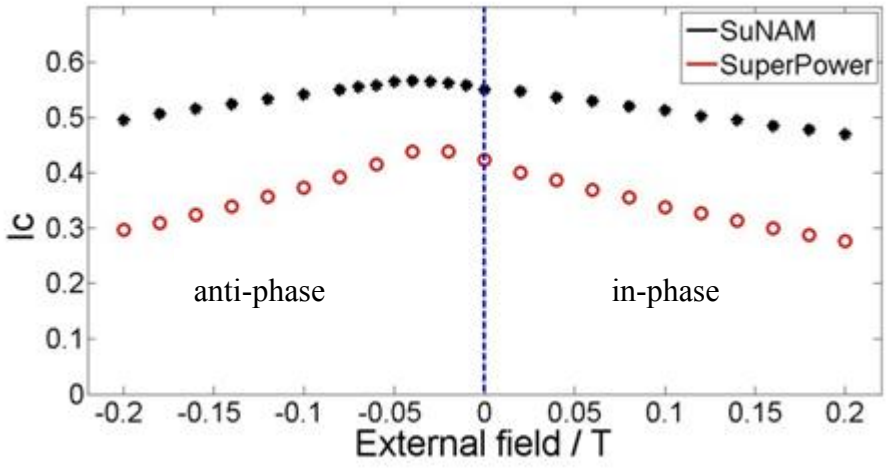

Figure 4-28 Simulated critical currents of coils after normalization with self-field tape I_c. The coils are wound with SuNAM and SuperPower tapes, which have different field dependencies. The SuNAM field dependency is presented in Figure 3-11(a) and the SuperPower field dependency is presented in Figure 3-11(b).

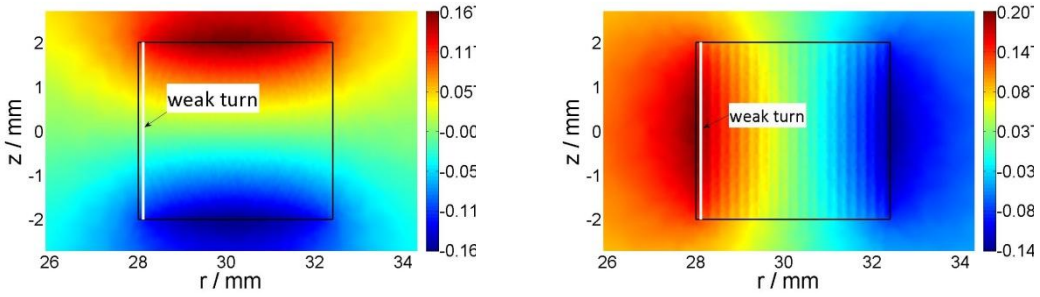

a) B_r b) B_z

Figure 4-29 Perpendicular field and parallel field distribution for a 20-turn coil. This coil has a uniform current distribution and each tape transports a current of 100 A. (unit is T.)

The same idea can be extended to HTS coils, which can be found in [115]. However, the HTS situation is a bit more complex, owing to the intrinsic anisotropy of the critical current. For one thing, the critical current under parallel and perpendicular external fields is quite different, as shown in Figure 3-11. So, for HTS, the in-field critical current line has two options, the parallel curve and the perpendicular curve. In the literature, for BSCCO and some YBCO conductors, the critical current line is often chosen as the perpendicular curve, since the perpendicular curve is lower than the parallel curve given a magnetic field with the same magnitude for normal HTS conductors. There is also another ambiguous point, being how to select the magnetic field to define the load line.

The load line usually stems from the maximum axial field at the inner turns. Some other literature adds a second load line representing the radial field at the coil end [116]. All these methods define the load line by the local peak field.

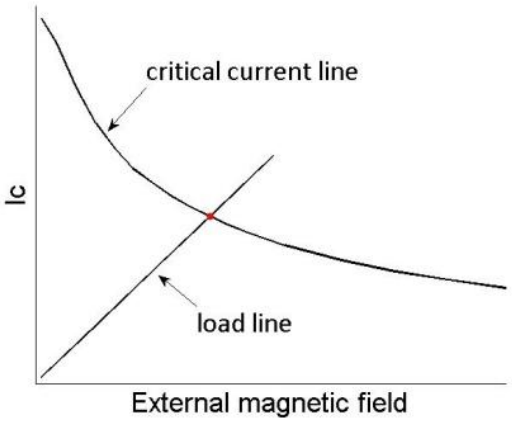

Figure 4-30 Schematic diagram for the load line method. The critical current line is usually based on measurement of a short sample under an external field. The load line represents the peak field as a function of the transporting current.

We built an equivalent model of Figure 4-10, only replacing the YBCO conductor with copper whilst keeping the geometry and mesh the same. Figure 4-29 presents the magnetic field in both the parallel and perpendicular directions. The load line of the local maximum B_z consists of two parts: the self field and the external field, so this curve has this equation:

$$I_c\left(B_z\right) = kB_z + B_e \qquad \text{Equation 4-21}$$

The current is assumed to be uniform across the section, so that the maximum of self field B_z and the applied current is linearly related, and k is the linear coefficient, as defined in Equation 3-14. B_e is the external field along z axis, which is -0.08T for Figure 4-31.

Figure 4-32 shows the I_c with different external fields by the load line method with local maximum B_z. Generally speaking, the calculated results based on the load line showed a similar trend, varying with the applied external field. However, some differences still existed when the external field ranged from -0.1 T to 0 T. This difference mainly results from the fact that the influence of the perpendicular field was ignored. Based on the measured field dependency of the critical current, the perpendicular field plays a non-trivial role. Additionally, only the local field was

employed to define the load line, which unavoidably introduces errors, as the magnetic field is not uniform along the weak turn, as shown in Figure 4-29.

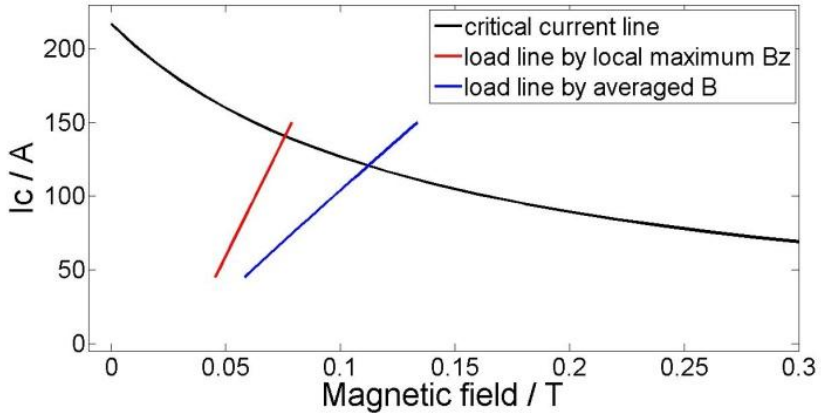

Figure 4-31 Two load curves for the SuNAM coil under a -0.08T external field. The cross points between the load lines and the critical current line represent the estimated critical currents. The critical current of the tape is 217 A. The predicted critical currents are 140 A (B_z) and 120 A (averaged B).

In order to improve the accuracy, a new method is proposed to define the load line. Rather than utilizing the maximum field in the weak turn, the new load line is defined by the normalized field in the weak turn. This averaged field takes into account both the parallel and perpendicular fields, normalized by Kim model:

$$B_{normalized} = \sqrt{\left(B_r\right)^2 + k^2\left(B_z + B_e\right)^2} \qquad \text{Equation 4-22}$$

we used the averaged $B_{\text{normalized}}$ to replace the maximum local B_z in Equation 4-21. Figure 4-31 shows the new load line. Figure 4-33 shows that the modified load line method has a much improved I_c calculation among the whole range of external fields. This agreement confirms the necessity of considering B_r when using the load line method to estimate the critical current of a conductor with anisotropy.

4.6 Summary

Chapter 4 investigated a single YBCO coil to determine the critical current and AC losses. The first part of the chapter was devoted to study of the coil under a self field. Starting from Progozhin's model dealing with stacks of superconducting strips with infinite length, this chapter gave a more detailed model for 2G HTS coils, adapted it for transport current, and then calculated the critical current and AC loss taking into account

the measured variation of J_c with magnetic field dependency. The calculated results were consistent with the experiments, and also offered some other insights into the transporting current of HTS coils. Our model predicted critical currents for coils with different numbers of turns within a 2.7% discrepancy with the measured critical current, if the criterion was selected as 0.5 μV/cm. Compared to the critical current defined by 1 μV/cm, our model gave a conservative estimation of the critical current for superconducting coils. Regarding the measurement of AC losses, this model showed very good agreements for different coils, not only verified by the total loss in the coil, but also from the good agreement with experimental results for the innermost 10 turns. This demonstrated that our model was a powerful tool for simulating AC losses of the transporting current. We presented the load line and critical current line of a parallel magnetic field in the same graph and received very good I_c predictions. Finally, we discussed the instantaneous AC losses within the coil and presented the AC losses for different turns of the coil.

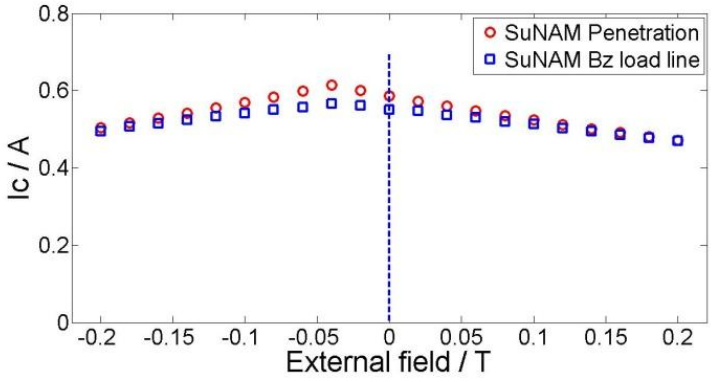

(a)

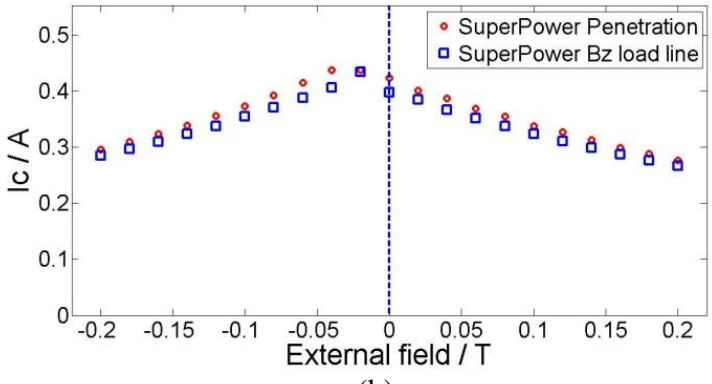

(b)

Figure 4-32 Comparison of the critical current predicted by the penetration method and the B_z load line method with different external magnetic fields ranging from -0.2 T to

0.2 T. The critical current is normalized by the critical current of the tape. (a) SuNAM 20-turn coil; (b) SuperPower 20-turn coil.

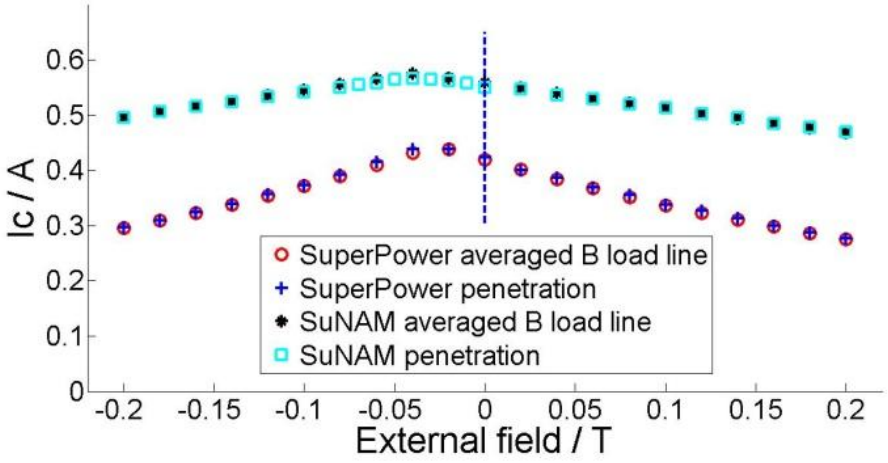

Figure 4-33 Comparison of the critical current of the coils predicted by the penetration method and the average *B* load line method with different external magnetic fields ranging from -0.2 T to 0.2 T. The critical current is normalized by the critical current of the tape.

The second part of Chapter 4 continued to study the coil under an external field. Two types of commercial superconductor were used to wind the coils. Both tapes could be approximated by the modified Kim model. We investigated the critical current of the coils under different magnetic fields both experimentally and numerically. It was found that the in-phase external field decreased the critical current of the coils due to the enhancement of the magnetic field of the weakest turn, thus reducing the critical current. However, the anti-phase field at first increased the critical current of the coils before driving it down. The initial increase was because the external field initially canceled the magnetic field. We also found that the existence of the external field may change the position of the weak turns. When the anti-phase field exceeded a certain limit, the outermost turn was the weakest turn, rather than the innermost. This can also be confirmed by measurement of the voltage in the corresponding sections. With the help of the numerical model, we further compared the tapes with different field dependencies of critical current for application in coils. Our results showed that the parallel field played a more important role in determining the critical current. This was because the parallel field was a bit larger than the perpendicular field, and even more so on the weakest turn. Thus, the tape that was less

sensitive to a parallel field was more attractive for application in coils. This was especially true for a small diameter coil. Finally, the load line method for calculating the critical current of a coil was extended to the consideration of HTS. We first employed the local maximum B_z field to define the load line. The errors under certain fields were quite large, showing the necessity of considering B_r We therefore used the averaged normalized magnetic field to define the load line, and this new method gave very good critical current estimation.

Chapter 5. Modelling of Superconducting Coil Stacks

Superconducting coils with thousands of turns using REBCO coated conductors have been the object of extensive investigation in recent years [117-119]. HTS magnets begin to be used as insert magnets for their high current density under extreme high magnetic fields [120, 121]. They are also used in energy storage and transformers [115, 122, 123]. All these applications share a same key component: a stack of superconducting pancake coils. Thus, a thorough understanding of the electromagnetic fields involved is of vital importance for designing and evaluating their performance, especially estimating of AC losses. Although there is no AC electromagnetic field during normal operation for some devices, the charging/discharging process and other transient conditions could also produce AC losses, which will determine the cryogenic design and normal operating parameters.

However, AC loss calculation is still a challenging problem for superconducting devices with large numbers of turns due to the high aspect ratio and non-linearity in the electromagnetic relation [124]. Modelling and simulation of superconducting coil stack has already been tried by assuming a constant current distribution in the turns [125] and using a homogenized bulk equivalent to approximate the coils [43, 44, 49].

Although H formula is widely accepted in superconducting simulation, the huge meshes and high non-linearity makes it very unefficient in real superconducting coil simulation. Chapter 4 solves the modelling of single coil, however, for stack of coils, this model is still not efficient enough. Following the model of minimisation of magnetic energy in previous chapter, we develop a new efficient model to calculate the current distribution and AC losses for multi pancakes using the line front track approximation in this chapter.

The structure of this chapter is as follows: the second section introduces the model, in which the geometry, assumption and model establishment process are introduced in detail. This model is validated using a COMSOL model, taking a 1200-turn magnet as an example. Section 5.3 discusses the design of a 2 kJ superconducting pancake coil currently under construction in our laboratory.

5.1 Numerical modelling

5.1.1 Assumptions

Figure 5-1 shows the cross-sectional view of a stack of pancakes. Before we go to the details of the model, three assumptions are made at the beginning.

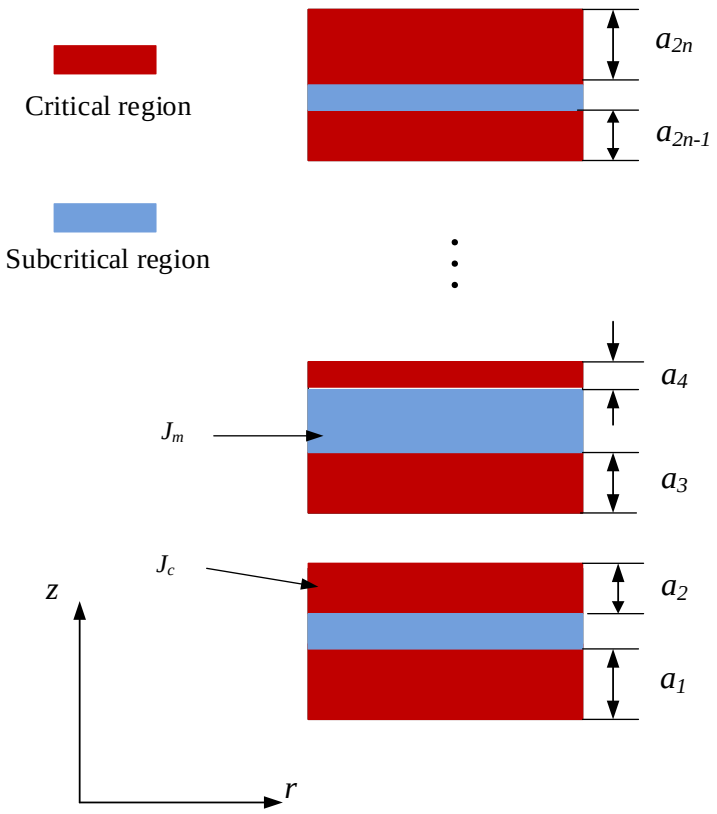

Figure 5-1 The cross-section view of a stack of pancakes with line front track for the critical region. The red parts stand for the critical region which has a current density of J_c and the middle parts are the subcritical regions with a current density of J_m. The superconducting regions are meshed by the lines. The parameters a_1, a_2,.. a_{2n} are the critical region widths.

Firstly, the penetration front boundary of the critical region is considered to be a straight line in all pancakes. When the critical regions emerge within the superconducting section, the widths are noted by a_1, a_2,…, a_{2n}, respectively, as shown in Figure 5-1.

Secondly, the critical state model is used to allocate the current in different regions, i.e. the critical region has a current density of J_c and the subcritical region current density is marked by J_m. In this chapter, J_c is considered to be independent of the field and remains constant along the critical region. Since the magnetic field can't penetrate the superconductor in subcritical region, we can derive the $B_z = 0$. As $\nabla \cdot B = 0$, we can find that $\frac{\partial B_x}{x} + \frac{\partial B_z}{z} = 0$, thus $\frac{\partial B_x}{x} = 0$, that is B_x is constant along x axis. Also Ampere's law tells that $\mu_0 J_m = \frac{\partial B_x}{z} - \frac{\partial B_z}{x}$, therefore, J_m is constant along x axis. Then, J_m can be calculated when each tape carries a fixed current, as shown in the following section.

The third assumption is that the critical state equilibrium condition is reached by minimizing the magnetic energy in the superconducting regions. This process can be realized by minimizing the integration of $A \cdot J$ across the whole region, as we do in Chapter 4.

5.1.2 Implementation of coil stacks

The line front track method is different from other approaches [34, 103] in that it predefines the current distribution field before optimization. This will decrease the variables during optimisation. This makes the field calculation easier and saves computer memory, as fewer meshes and inductance matrices are stored during the simulation. Additionally, the loss is calculated based on the peak time field distribution, rather than on sequential steps from the beginning to the end of one cycle. This makes the AC loss calculation much quicker, because we only need to calculate the critical state at peak time directly.

In Figure 5-1, both the penetrated and unpenetrated regions are meshed into elements with a uniform current density. Given that the widths of the penetrated regions are a_1, a_2,…, a_{2n}, the elements belonging to the subcritical regions have a current density:

$$J_m^i = \frac{I - J_c^{2i-1} a^{2i-1} t - J_c^{2i} a^{2i} t}{(w - a^{2i-1} - a^{2i})t} \qquad \text{Equation 5-1}$$

where J_m^i is the subcritical region current density of the *i*th pancake, J_c^{2i-1} and a^{2i-1} are the current density and the region width of the bottom critical region of the *i*th pancake, J_c^{2i} and a^{2i} are the current density and the region width of the up side critical region, *w* is the width of tape width, and t is the thickness of the tape.

Each element can be considered as a ring conductor along the *z*-axis, According to the Maxwell theory, the potential and magnetic fields can be integrated with the current distribution, that is:

$$A^k = \sum_i M_i^k I_i \qquad \text{Equation 5-2}$$

where A^k is the magnetic vector potential for the *k*th element, M_i^k is the mutual inductance matrix, and I_i is the current in the *i*th element. The detailed equations for mutual inductance are found in [44]:

$$A(r',z') = \frac{\mu_0 I}{2\pi r_1}\left(\frac{r}{r'}\right)^{\frac{1}{2}}\left[\left(1-\frac{k^2}{2}\right)K - E\right]$$

$$B_z(r',z') = \frac{\mu_0 I}{2\pi r_1}\frac{z-z'}{\left((z-z')^2+(r+r')^2\right)^{\frac{1}{2}}}\left[-K + \frac{r^2+r'^2+(z-z')^2}{(r-r')^2+(z-z')^2}E\right]$$

$$k^2 = \frac{4rr'}{d^2 + (r+r')^2}$$

where where *K* and *E* are complete elliptic integrals of the first and second kind.

According to the third assumption, the object function can be defined by potential *A* and *J*:

$$f_1 = \sum_{k\in\Omega} A^k I^k \qquad \text{Equation 5-3}$$

where *Ω* contains all the elements in the superconductor. The condition with the minimum value of f_1 represents the real current distribution. With the help of MATLAB optimization tool, the optimized width of critical region can be calculated. We can get the magnetic field and potential across the superconductor section after the current distribution is available.

AC loss calculation is a key question for superconductor simulation. There are several approaches to calculate the AC loss for a given field distribution. A common method is to sum the instantaneous losses over the whole period, from which the instantaneous loss is the integration of EJ in the conductor area [50]. This approach requires solutions for every time step, which makes the calculation inefficient. Another approach can be implemented by integration of B_z and J_y in the critical region at the peak time:

$$Q = 4 \sum_{i \in \Omega_{critical}} B_r^i I^i d^i \qquad \text{Equation 5-4}$$

where B_r^i is the perpendicular field of the ith element at the peak time, and is solved through FEM, I^i is the current of the ith element at the peak time, and d^i is the flux moving distance when the current increases from zero to the peak. The physical interpretation of Equation 5-4 is the summation of the energy dissipated by vortices as they move a distance d from the edge to their final positions at peak time [43, 126]. The second method is employed in this chapter for its high efficiency and acceptable accuracy.

5.2 Results and analysis

A case study of a 12-pancake coil was calculated using this model and benchmarked against another established model. The benchmarked H formula model, described in Ref. [127], considered a fully featured stack of 12 YBCO pancake coils, in which each pancake contains 100 layers. Geometrical details of the model are presented in Table 5-1. Figure 5-2 compares the AC losses in the coil between two models with different transporting currents, from 10 A to 50 A. This figure shows that the line front track model has quite good agreement with the H formula result for different amplitudes of the applied current during periodical cycles. Small deviations exist when the applied currents are 10 A and 40 A. These deviations have two causes: the first reason is that in real superconductors the separation between the critical region and the subcritical region is not an ideal straight line, and the second reason is that Equation 5-4 may introduce some errors.

Table 5-1 Detailed parameters for the validation model

Parameter	Value
Tape I_c	100 A
Tape width	4 mm
Tape thickness	0.21 mm
Pancake gap	0.57 mm
Coil radius	42 mm

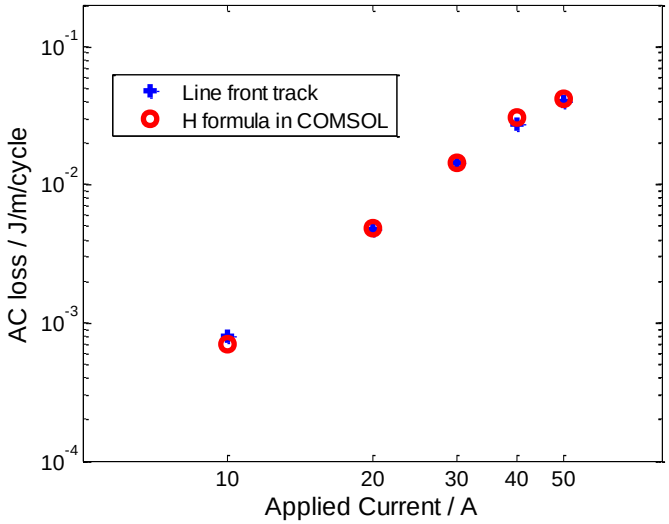

Figure 5-2 AC losses with different applied currents from COMSOL and the line front track model.

After the line front track model was validated by the H formula in COMSOL, we used it to predict the electromagnetic field and current distribution. Figure 5-3 presents the distribution of the axial and radial fields in the coil when the operation current ramped up to the peak value of 50 A. According to Figure 5-3(a), as expected, the coil excited a positive axial field in the central region and negative fields outside the coil. According to Biot-Savart's law and the superposition principle of the magnetic field, the magnitude of the radial fields increase along the z direction from the midplane. Figure 5-3(b) shows that the radial fields peak at the top and bottom pancakes, and can therefore penetrate most of the top and bottom pancake. For this reason, the penetration proportion of a pancake decreases from the top and bottom pancakes to the middle two pancakes. Figure 5-3(c) shows that the contour of B_{normal} is parallel to the tape surface and $\int B_r^2 dr dz$ in the superconducting region is minimized. This is because the magnetic

field can't penetrate the tape, which is the foundation for the Clem [43] and Yuan model [44, 45].

Figure 5-4 shows the current density distributions in the coil when the applied current is 50 A, calculated by H-formula and line front track method. Figure 5-4(a) and Figure 5-4(b) show that the results are quite consistent with each other. The results using the H formula show that the penetration fronts between the critical region and the subcritical region are straight lines, although slight curve tracks can be found in the innermost and outermost turns of the 4th, 5th, 8th and 9th pancakes. These derivations can be attributed to the AC loss differences between our model and the H formula, as shown in Figure 5-2.

We also found that the opposite-direction shielding currents are induced in the coil in order to prevent the radial field from penetrating the pancakes. The penetration fronts in the pancakes are consistent with the radial field fronts in Figure 5-3(b). In the top and bottom pancakes, the shielding currents are obviously due to the high radial field. Figure 5-5 gives the current density profile along the dashed line in Figure 5-4(b), and more clearly shows the shielding current.

The AC losses in each pancake for one whole cycle with a peak current of 50 A are shown in Figure 5-6. The bottom pancake is represented by pancake No. 1 and the top pancake corresponds to pancake No. 12. There is obvious symmetry, and the top and bottom pancakes generate the maximum AC losses. This is because the top and bottom pancakes are penetrated more, which is consistent with Figure 5-5.

Figure 5-7 compares the normalized AC loss distribution for the 12-pancake coil when the applied currents vary from 50 A to 10 A. All the values are normalized by the total AC loss of the coil in the corresponding cycle, to directly show the proportional contribution of each pancake to the total AC loss in the coil. It can be concluded that the bottom three pancakes and the top three pancakes contribute most of the total AC loss: these six pancakes generate more than 90% of the total AC losses. It is known that each pancake transports the same current and that the bottom and top pancakes have a higher magnetic field (shown in Figure 5-3), and therefore we can understand that the magnetisation loss is the dominant factor in the AC loss of the stack of coils in this case.

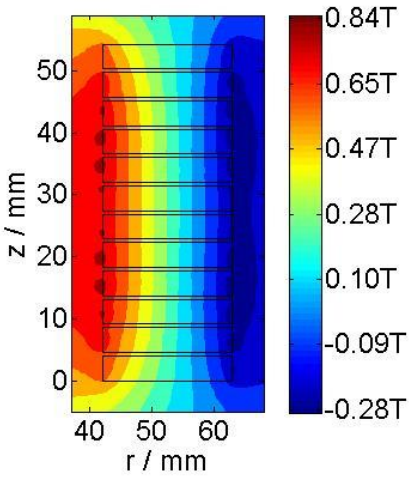

(a)

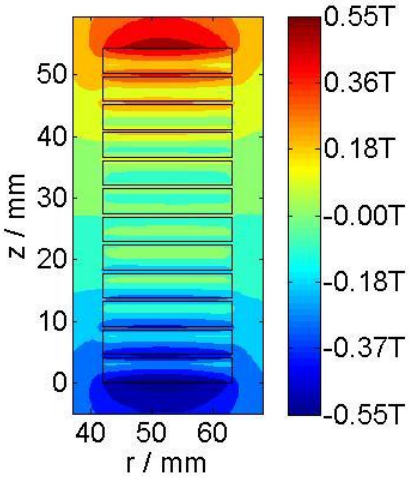

(b)

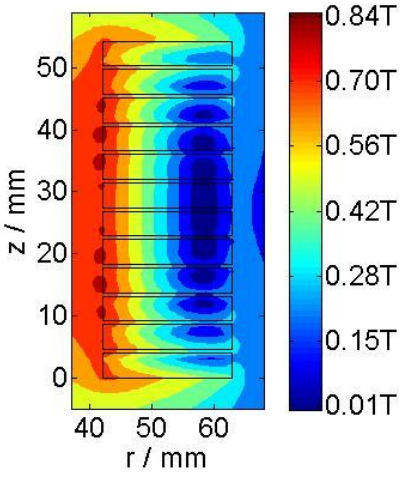

(c)

Figure 5-3 Magnetic field distribution for the 12-pancake coil calculated by the line front track method. Each pancake has 100 turns. The applied current is 50 A. (a) B_z; (b) B_r; (c) B_{normal}

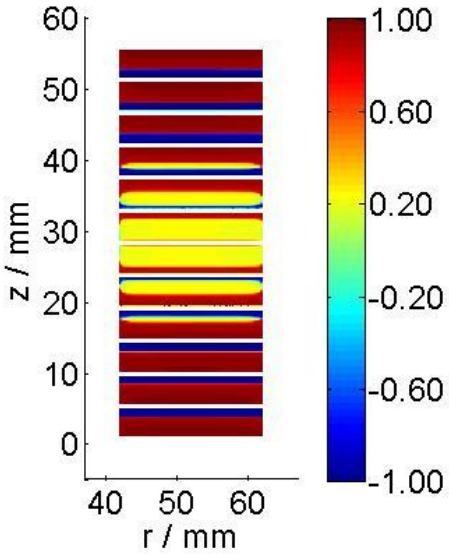

(a)

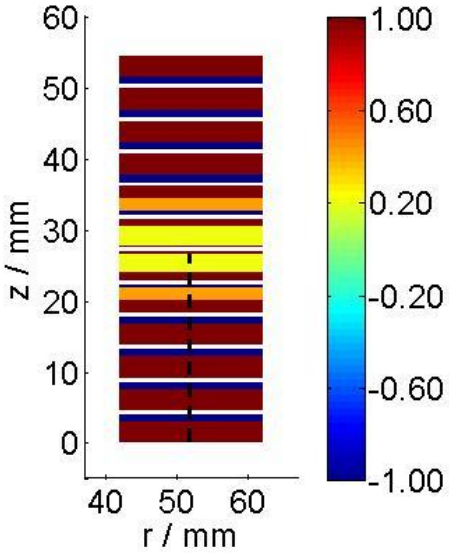

(b)

Figure 5-4 Current distribution of 12-pancake coils. Each coil has 100 turns calculated using the H-formula in COMSOL and the line front track method. The applied current is 50 A. The current distribution is normalized by the local critical current density. These pictures show that the superconducting regions can be categorized into two parts: the critical region and the subcritical region. The penetration front track can be effectively approximated using straight lines.

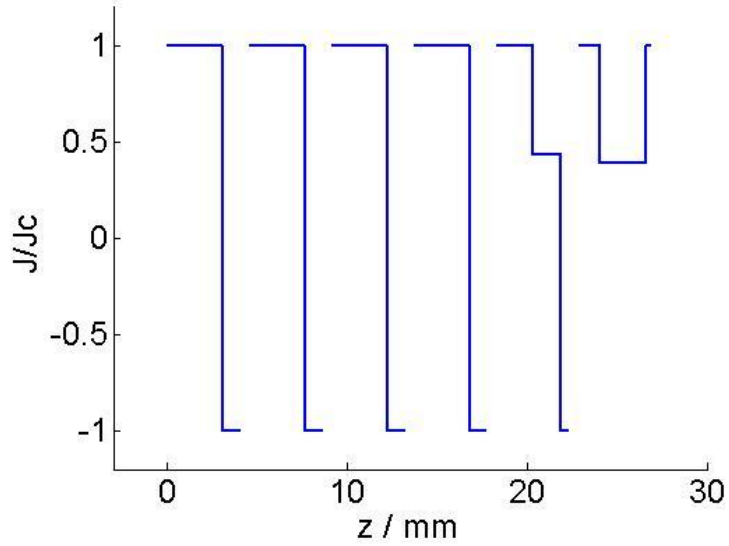

Figure 5-5 The current density profile along the dashed line in Figure 5-4(b).

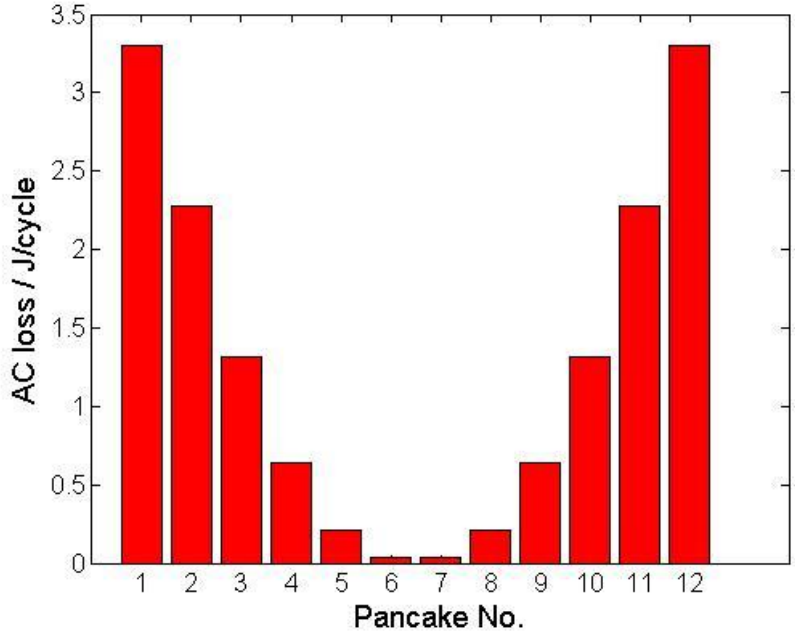

Figure 5-6 AC losses of individual pancakes for the 12-pancake coils. The applied current is 50 A.

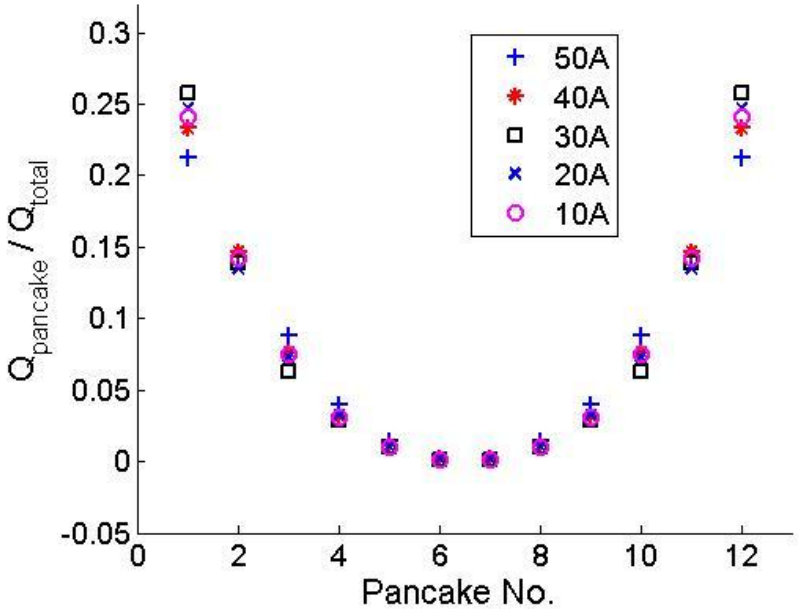

Figure 5-7 The normalized AC loss distribution in the 12-pancake coil with different applied currents. $Q_{pancake}$ denotes the AC loss in each pancake, while Q_{total} represents the total AC loss in the coil.

5.3 Analysis of a 6-pancake coil with different temperature and configuration

At the moment, a 2kJ SMES is under construction in the applied superconductivity lab. As has been demonstrated, the line front track is an efficient method for calculating the electromagnetic field of stacks of coils, and thus this method was further used to optimize the design of ongoing SMES magnet. In this section, some key parameters involving the performance of SMES will be discussed. The object of SMES design is to find the optimal configuration and operating conditions by raising the energy and reducing the AC loss.

Operating temperature is one of the key working parameters, because the total energy of the coils, which is related to the critical current density, is largely determined by the temperature. Additionally, quench protection design also needs to take the temperature in account. However, the temperature is constrained by the cooling power of the cryogenic refrigerator, so the selection of the working temperature should balance these two aspects.

Figure 5-8 shows the critical current with temperature for 4 mm wide tape from the SuperPower product datasheet. The critical current of the tape is closely linked to the temperature. Roughly speaking, when the temperature decreased by 1 K, the corresponding critical current increased by about 20 A, showing that decreasing the working temperature is the one of most efficient approaches to enhance the energy and power capability .

Figure 5-9 shows the AC loss of the coils at different temperatures with a fixed current. In this case, the applied current is 150 A, which enables the coils to hold the energy of 2 kJ. This is the rated current and rated energy for the SMES under design, which will be constructed in the near future. Figure 5-9 shows that raising the operating temperature from 20 K to 65 K could decrease the energy by 8%, however, the AC losses would increase by about 40%. This means that given a constant current, at different temperatures the stored energy is almost constant, however, a lower temperature has much smaller AC loss. This is because high critical current at lower temperature will lead to less penetration.

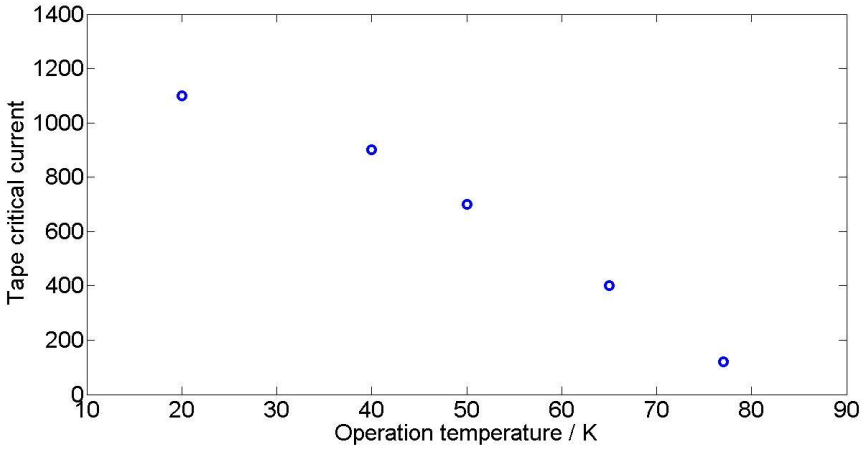

Figure 5-8 The critical current of a 2G HTS conductor under a self field in different operating temperatures [124].

There are two important parameters for geometry design: coil radius and gap between the neighbouring coils. At the moment, the commercially availabe 2G HTS tape is supplied at a fixed length. As for convenicence, the tapes with the length of 50 m is discussed here. For other types of superconductor, the whole process is exactly the same.

This piece of conductor is wound into a pancake coil, so that coils with different radii have different numbers of turns, as shown in Table 5-2.

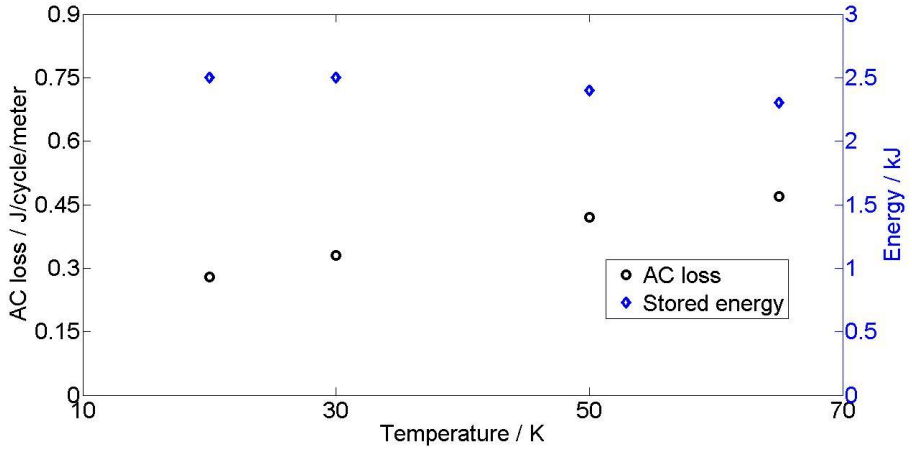

Figure 5-9 AC losses and stored energy in the 2 kJ SMES at different temperatures. Each tape is transporting a current of 150 A.

Table 5-2 The total turns for each pancake with different radii, given a 50 m length of conductor for each pancake

Radius	28mm	35mm	44.5mm	60mm	76mm
Turns	170	150	130	110	90

In order to analyse the influence of the coil radius, it is assumed that each pancake coil had a length of 50 m and that the SMES was assembled by 12 stacked coils. Figure 5-10 presents the stored energy and the AC loss with a transporting current of 150 A at a temperature of 50 K. This graph shows that given the total conductor length, increasing the radius decreases the stored energy as well as the loss. This is because a large radius decreases the magnetic field, which can decrease the energy density, also decrease the magnetisation part of AC losses.

Another geometry parameter is the gap between coils. Figure 5-11 presents the energy and AC loss when the applied current is 150 A at a temperature of 50 K, where the gap varies from 1 mm to 8 mm, showing that the AC loss decreases continuously. This is because the bigger the gap is, the less the magnetization current is induced. Hence reducing the field created by the neighbouring pancakes. This will lead to a smaller penetration depth and smaller loss dissipation. While the energy decreases by

40%, the loss with an 8 mm gap is only 8% of that with a gap of 0.5 mm, showing a reduction of 92%.

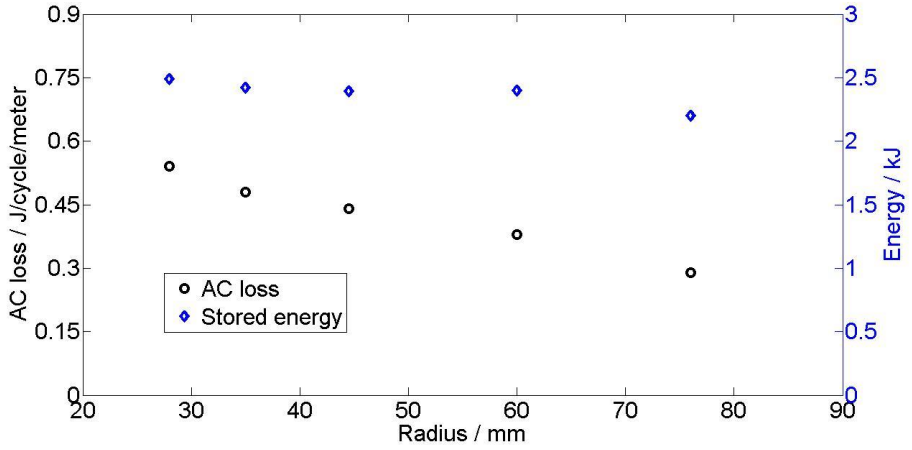

Figure 5-10 AC losses and stored energy in the 2kJ SMES with different radii. Each pancake coil is wound with a piece of 50-m YBCO conductor

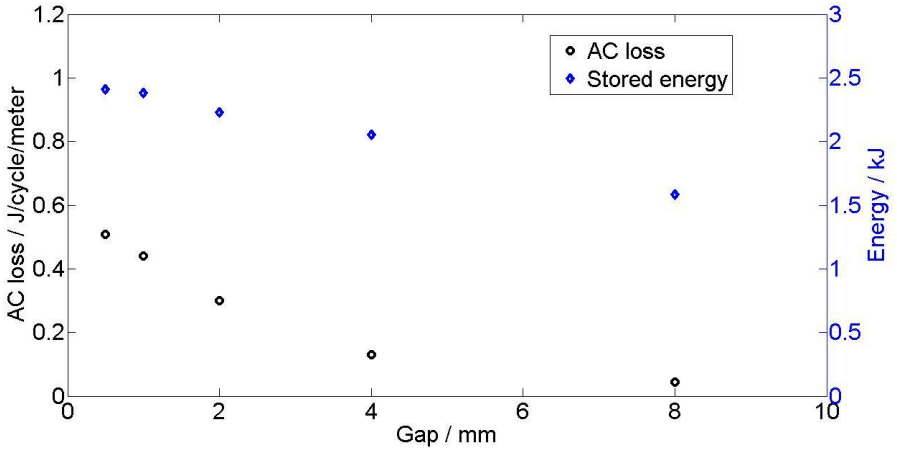

Figure 5-11 AC losses and stored energy in the 2 kJ SMES with different gaps. Each tape is transporting a current of 150 A.

5.4 Summary

Chapter 5 proposed a model for calculating the current distribution and AC loss for superconducting multi pancake coils. The critical state model was applied in the critical region, and each tape was constrained by a fixed current. The critical regions were optimized according to the minimization of the magnetic energy in the superconducting region. To validate the model, comparisons were made between H formula in COMSOL and our new model. The current distribution can be closely approximated by the line

front track method, as shown by the full detailed COMSOL simulation. We also found quite good agreement between the AC loss results.

We further applied this model in the design of 2 kJ SMES which was currently under construction. The AC losses and stored energy were calculated and analysed at different operating temperatures, coil radii and pancake gaps. Some guidelines were suggested for the design of SMES magnets. Key parameters, such as operation temperature, pancake radii, gap between neighbouring pancakes were compared based on the AC losses and stored energy.

Chapter 6. Design, Simulation and Application of SMES System

SMES is able to smooth the fluctuations of renewable energy generation due to its advantage of high power density and fast response. This chapter firstly presents a conceptual design of a 60 kJ SMES for a renewable energy system. The main part of the SMES design involves optimisation of the coil configuration, AC loss estimation, current lead optimization and design of the cooling system. The application of SMES in a hybrid energy system for a wave energy generation system is then demonstrated using Matlab/Simulink model. The extension of the battery extension with the help of SMES is analyzed and quantified. Electronic inverters are proposed to investigate the feasibility of stabilizing frequent power fluctuation. Finally the economic prospects of large scale SMES systems are discussed for solenoid and toroidal configurations.

6.1 Conceptual SMES design for renewable energy generation

As penetration of renewable generation technology increases in the power grid, it is economically and environmentally beneficial to smooth the intermittent power and hence make the best use of local renewable energy sources. Due to the large variation in the load/generation balance of renewable energy sources, an energy storage system with the capability of fast response to power fluctuations over a short time scale of seconds to minutes will have the greatest value for renewable microgrids [128, 129].

Traditionally, batteries are widely used as energy storage systems in renewable energy generation. Their advantages include large energy density, mature technologies and cheap prices. However, the disadvantages of batteries include a small power density and short lifetime. Since the fluctuation of the power output of the renewable energy system is usually swift, batteries usually have too slow a response.

Therefore batteries are not able to address the challenges of balancing frequent power fluctuations over a short time scale of seconds. SMES, supercapacitors and flywheels have large power densities, large duty cycles and fast response speeds. Hybridized with batteries, they are able to compensate for the shortcomings of batteries. Compared to flywheels and supercapacitors, SMES systems have significantly larger power densities and module power ratings. In addition, they have advantages such as high round-trip efficiencies and solid-state operation. Therefore SMES systems are preferred to increase the performance of hybrid energy storage systems.

6.1.1 Requirement of the SMES system for a wave energy converter

Marine wave power is a vast and largely untapped source of energy. Direct Drive Linear Wave Energy Converters (DDLWEC) are one of the most promising technologies that can harness waves for electricity generation. Ocean waves, having periods ranging from 5 to 15 seconds, normally have the feasibility and the potential for driving DDLWECs to generate electricity. SMES has a large power density and fast responding time, which could easily meet the system's requirement in terms of power and speed. The available wave power that can be extracted from the ocean can be predicted from the weathercast over a certain time. Hence, the output power generated from a particular DDLWEC can be evaluated. The energy capacity of an SMES system is calculated to handle the difference between the maximum and average power from a DDLWEC at a specific location over a certain time. Taking the integration of the power difference over time gives the maximum energy that needs to be stored by the SMES. A 60 kJ SMES operating at 65 K is designed to handle the frequent power fluctuation caused by a particular DDLWEC during each wave period. 65 K is the lowest temperature of sub-cooled liquid nitrogen. This cooling temperature is selected to minimize the cooling cost while increasing the energy density.

6.1.2 Superconducting coil design methodology

According to the principle of superconducting energy storage, increasing the operating current of SMES is an efficient way to increase the stored energy. However, as demonstrated in Chapter 3, the critical current density of 2G HTS has anisotropic characteristics under an external magnetic field, thus, the configuration parameters of the coil must be optimized carefully to maximize the energy. The fabrication of an

SMES system must also consider the fabrication cost, cryogenic system design, mechanical stability, current lead design, and magnetic field leakage, etc.

The factors involved in an SMES design process include:

1) Inductance of coils: The inductance of coils can be increased by varying the configuration. Two methods are available to calculate the inductance of the coil. The first is based on the analytical formula, which can only be applied to calculate the coils with simple geometries. The second method is to simulate the electromagnetic field using FEM and then use the field to calculate the inductance. The second method is comparatively more suitable and adaptable to complex geometries, and is applied in the following section.

2) Critical current: The anisotropic properties of the superconducting tape cause the critical current to decrease dramatically under an external magnetic field. The coil design process should take this anisotropy into account and minimize the magnetic field. The load line method can be employed to determine the critical current given the field dependency.

3) Cryogenic system. Superconductivity can only occur when the temperature is extremely low. The cryogenic system plays an important role in the operation of SMES. Liquid nitrogen and cryocooler are the two major cooling methods mostly used. Recently, cryocooler technology has attracted much attention for its advantage at lower temperatures, easier maintenance and better performance. In the following section, the cryocooler selection process is presented.

4) Current lead. Superconducting coils are connected to an external circuit at room temperature via the current lead. The thermal load in the current lead is thus one of the thermal sources in the system. Decreasing the thermal flux through the current load is the objective of the current lead design. Here, we will present the design process of a copper current lead.

5) Mechanical stress. There are two major sources which induce mechanical stress. The first is the Lorentz force, since the current circulating in the coil and the magnetic field is very large. The second is from the cooling process. An impregnation process is commonly used to enhance the coil, however the thermal expansion is different between

the superconducting material and the supporting component. The Lorentz force is analysed in this section.

6) The leakage of magnetic field. According to the theory of electromagnetic compatibility, an external magnetic field with a magnitude of 10^{-3} T will make many electronic devices fail. Thus, proper measurements should be applied to prevent the magnetic flux from straying.

7) Other factors. Real superconducting coils have other factors requiring consideration, such as limitations to installation space, the available length of superconducting wires, constraints on the volume and mass of superconducting coils and the current in different layers.

Since this section focuses on the conceptual design of SMES system, only (1) ~ (5) will be discussed in detail.

6.1.3 Material properties

The 2G HTS YBCO tape SC4050 AP, produced by SuperPower, was used for the design process. The main properties of the tapes are listed in Table 6-1. The tapes have a width of 4 mm and a thickness of 0.1 mm. Figure 6-1 presents the critical current, I_c, in different external magnetic flux densities at 65 K. The critical current of the tape is 400 A without an external magnetic field. The critical current varies widely under external magnetic fields, which should be considered in the magnet model.

Table 6-1 Specification of the SuperPower SCS 4050 AP YBCO tape

Specification	Value
Critical current (77 K, self field)	400 A
Average thickness	0.1 mm
Width	4 mm
Maximum tensile stress	>550 MPa

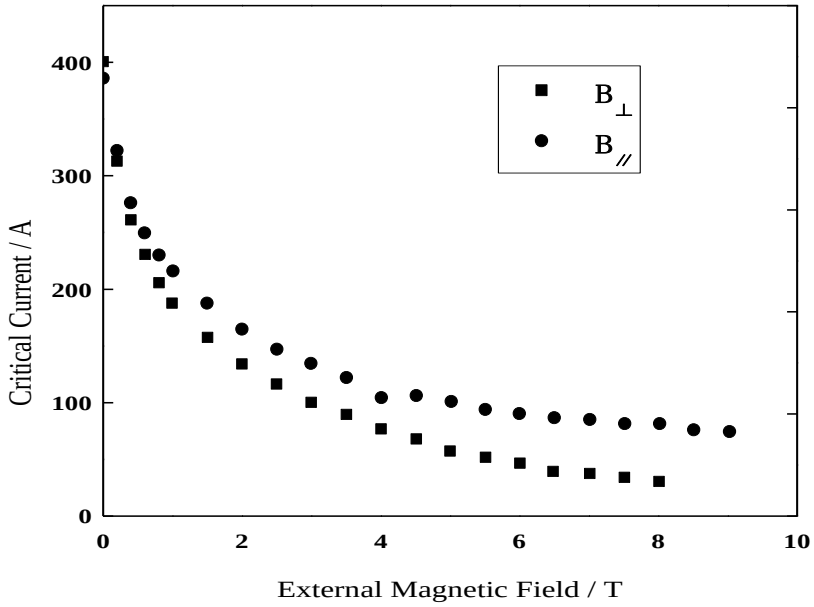

Figure 6-1 The $I_c(B)$ dependence of magnetic density flux in the parallel and perpendicular directions at 65 K [130].

6.1.4 Magnet design

The aim of magnet design is to achieve a stored energy of 60 kJ with the shortest length of tape. Solenoid and toroid are two types of SMES configurations normally used. Solenoid coils are easy to build and have higher energy densities. In our design, a stacked double pancake structure, which is basically a solenoid, was selected.

The energy stored in the coil can be calculated by:

$$E_S = \frac{1}{2} LI^2 \qquad \text{Equation 6-1}$$

where E_S is the energy stored in the coil, L is the inductance of the coil and I stands for the transporting current. It is clear that the inductance and current in the coils determines their stored energy. The inductance of the coils depends on their configuration [75]. At the same time, the critical current is mainly constrained by the maximum magnetic field to which the tapes are subjected, according to Figure 6-1. Thus it is essential to optimize the coil configuration to store the maximum energy and make the full use of the tapes.

A global optimization algorithm was incorporated into the finite element method (FEM) model using the COMSOL Multiphysics package and MATLAB. The flow chart of the algorithm is shown in Figure 6-2. One configuration for the magnet was first

chosen, to include the tape length, the inner radius and the number of pancakes. According to the Maxwell theory:

$$\nabla \times B = \mu_0 J \qquad \text{Equation 6-2}$$

If a certain current density J is applied to the section area, the magnetic flux density B and magnetic field H can be calculated by implementing FEM in COMSOL. The energy stored can be integrated over the section area since:

$$E_S = \int BdH \qquad \text{Equation 6-3}$$

Also, the critical current of this configuration can be determined by the magnetic flux density combined with the data given in Figure 6-1, using the modified load line method introduced in Chapter 4. This process was repeated until the final configuration was calculated. Three optimized configurations of the SMES magnet are shown in Table 6-2.

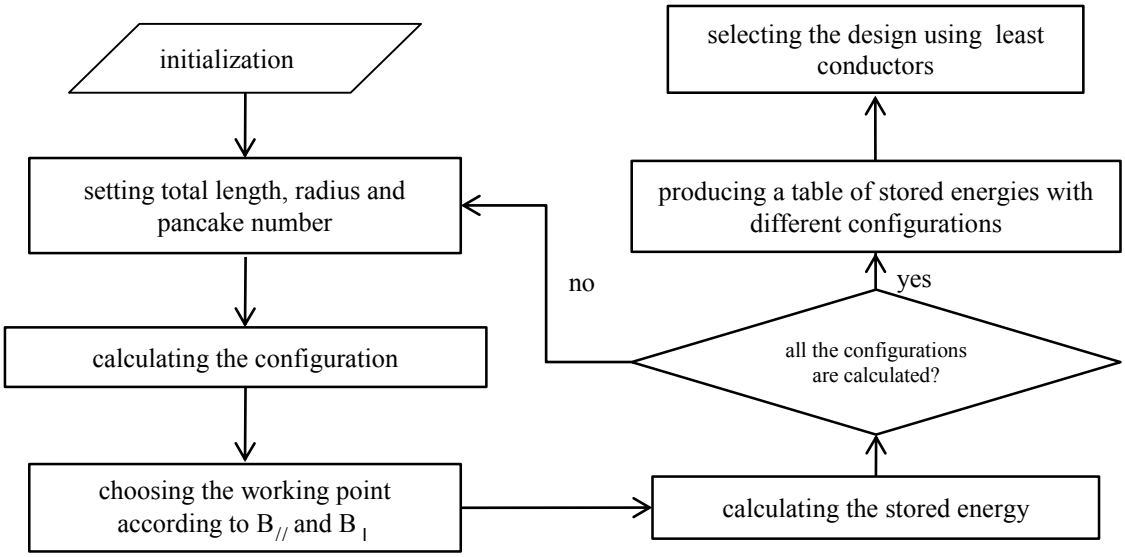

Figure 6-2 Flow chart for the optimization process.

Table 6-2 summarizes three optimized design configurations for the 60 kJ SMES. The total lengths for each design are almost the same: about 6200 m. The differences are the double pancake number and the radius. Design 1 has four double pancakes, while the other two designs have six and eight double pancakes, respectively. The table shows that although these three designs have different configurations, the total lengths don't vary much. This will help the engineers to simplify the design process, since the total energy is roughly related to the length of superconductor.

Table 6-2 Optimized design configurations of the 60 kJ HTS magnet

Parameters	Values		
	Design 1	**Design 2**	**Design 3**
Conductor length	6200 m	6100 m	6200 m
Inner radius	100 mm	140 mm	100 mm
Outer radius	186 mm	189 mm	150 mm
Number of double pancakes	4	6	8
Height	40 mm	60 mm	80 mm
Turns	5000	5880	7840
Inductance	3.8 H	3.8 H	3.9 H
Operating current	93 A	92.7 A	89 A

AC loss is a major problem for superconducting magnet designs, since it represents the main thermal load and determines the operating conditions. So far, very few methods are available to determine the AC losses for superconducting coils with thousands of turns. In Chapter 5, an efficient model based on the line front track and homogenisation was developed, which can be used for AC loss estimation and accurate magnetic field calculation in large coils. This method is used here to calculate the AC losses of the coils. This AC loss is the energy dissipation in one whole cycle.

Table 6-3 summarizes the AC losses, electromagnetic field and max von Mises stress for three different designs using the line front method when the applied currents are the critical currents of the coils. According to this table, Design 2 has 20% less magnetic field and 50% less von Mises stress, compared to Design 1 and Design 3. This is because Design 2 has a larger radius, 140 mm, while the other two designs have a radius of 100 mm. The smaller radius designs have more compact geometry which increases the magnetic field and hence increases the von Mises stress.

Based on the results in Table 6-3, Design 2 should be preferred in future construction, for several reasons. Firstly, the AC losses are smaller than the other two designs, which will render the thermal load easier to handle. Secondly, the magnetic and mechanical

fields are smaller, which makes the system safer to operate. Finally, as there are fewer winding turns in Design 2, the coil winding processes are less challenging.

Table 6-3 AC losses, electromagnetic field and max von Mises stress for three different designs. The applied currents are the critical currents presented in Table 6-2

Design No.	**Design 1**	**Design 2**	**Design 3**
AC loss	5204 J/cycle	5070 J/cycle	5562 J/cycle
Max B_{norm}	5.31 T	4.47 T	5.51 T
Max B_z	5.31 T	4.40 T	5.38 T
Max B_r	3.32 T	3.30 T	3.77 T
Max von Mises Stress	8.7 MPa	5.5 MPa	7.9 MPa

Figure 6-3 shows the current density distributions in the coil of Design 2 when the applied current is 90 A calculated using the line front track method. Figure 6-4 presents the current penetration depth of each pancake for the same coil under different currents. Figure 6-4 shows that when the current is small the penetration depths from the top and bottom to the middle decrease almost linearly. When the current increases, the penetration depth of each pancake also increases. After the outside pancakes are fully penetrated, the penetration depth remains constant. From this penetration depth graph, it can be inferred that the top and bottom will generate more losses, which will be discussed later.

Since the current running through the HTS is considerably large, the Lorentz force should be analysed to ensure the mechanical stability of the magnet. Figure 6-5 shows the maximum stress located on the inner edge of the coil for Design 2. The maximum von Mises stress was 5.4 MPa, which is within the permitted range of YBCO tape, so the SMES is mechanically stable in operation.

Figure 6-6 presents the distribution of the radial, axial and normal fields in the coil when the operation current ramps up to the peak value of 90 A. According to Figure 6-6(a), the radial fields peak at the top and bottom pancakes. Hence, it can penetrate most of the top and bottom pancakes. Also for this reason, the penetration proportion of a pancake decreases from the top and bottom pancakes to the middle two pancakes. Figure 6-6 (b), as expected, shows that the coil excites a positive axial field in the central

region and negative fields outside the coil. According to Biot-Savart's law and the superposition principle of the magnetic field, the magnitude of the radial fields increase along the *z* direction from the midplane. Figure 6-6 (c) shows that the contour of B_{normal} is parallel to the tape surface as the perpendicular field can't penetrate the superconducting tapes.

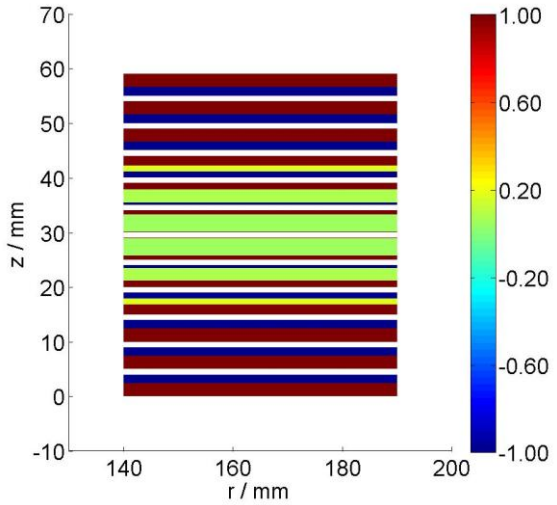

Figure 6-3 Current distribution of the Design 2 coil. Each pancake has 490 turns calculated by the line front track method. The applied current is 50 A. The current distribution is normalized by the local critical current density.

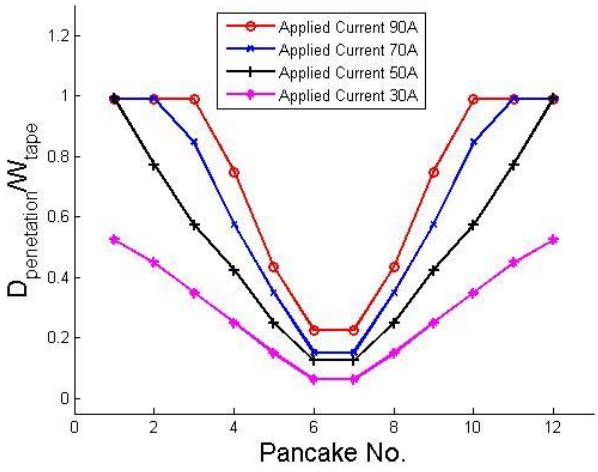

Figure 6-4 Penetration depth of each pancake for the Design 2 coil under different currents. The penetration depth is calculated by $a_{2i-1}+a_{2i}$ which is shown in Figure 5-1. W_{tape} is the width of the tape.

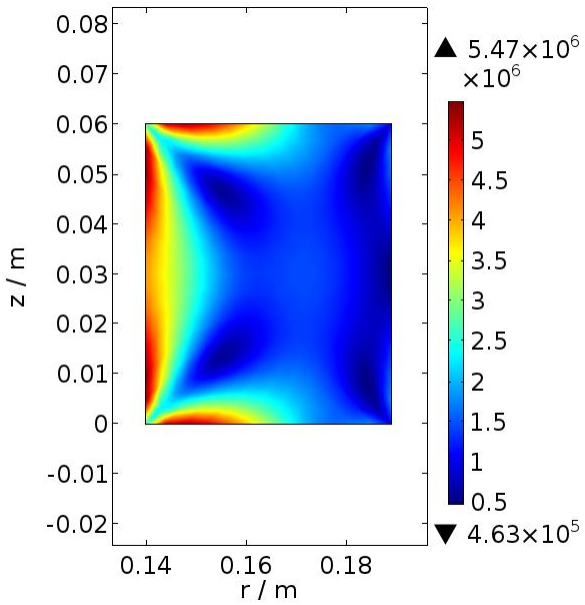

Figure 6-5 Stress distribution of Design 2 of the magnet (Pa).

Table 6-4 summarizes the AC losses for Design 2 with different applied currents using the line front track method. Figure 6-7 compares the normalized AC losses distribution for the Design 2 coil when the applied current varies from 90 A to 30 A. All the values are normalized by the total AC loss of the coil in the corresponding cycle so that we can directly see the proportional contribution of every pancake to the coil's total AC loss. It can be concluded that the bottom three pancakes and the top three pancakes contribute most of the total loss (these six pancakes generate more than 94% of the total AC losses). This is similar to the results in Figure 5-7. The AC losses distribution in the pancakes is partly related to the penetration depth distribution, as the larger the penetration depth, the higher the losses. However, comparison of Figure 6-4 and Figure 6-7 shows that there is some difference in the shape of the curve. In Figure 6-4, the penetration depth varies linearly, while Figure 6-7 varies in a higher order curve. The reason is the AC losses are dependent on two parameters: the penetrated current regions and the magnetic fields, as shown in Equation 5-4. As the top and bottom pancakes not only have larger penetration depths, but also higher magnetic fields, the AC losses distribution will vary in higher order curves.

Table 6-4 AC losses for Design 2 with different applied currents

Applied Current	**90 A**	**70 A**	**50 A**	**30 A**
AC loss	5436J/cycle	3089J/cycle	1176J/cycle	277J/cycle

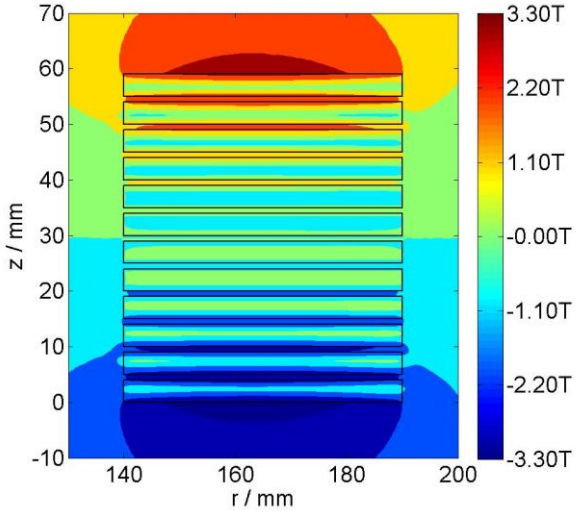

(a)

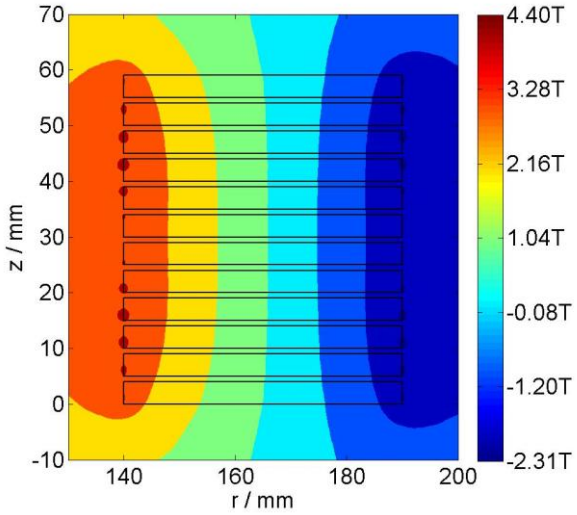

(b)

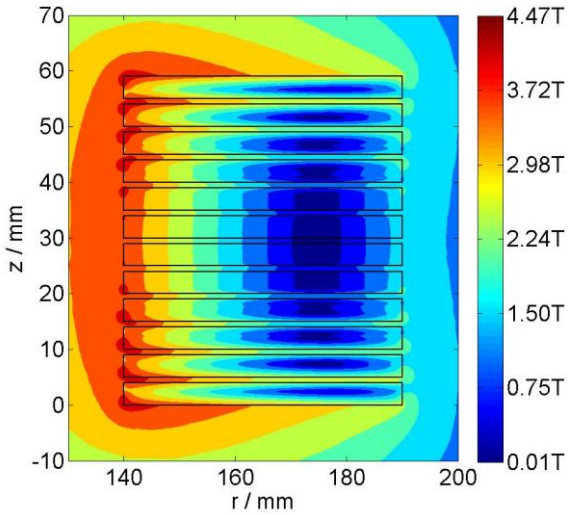

(c)

Figure 6-6 Magnetic field distribution of Design 2 (T): (a) B_r; (b) B_z; (c) B_{normal}.

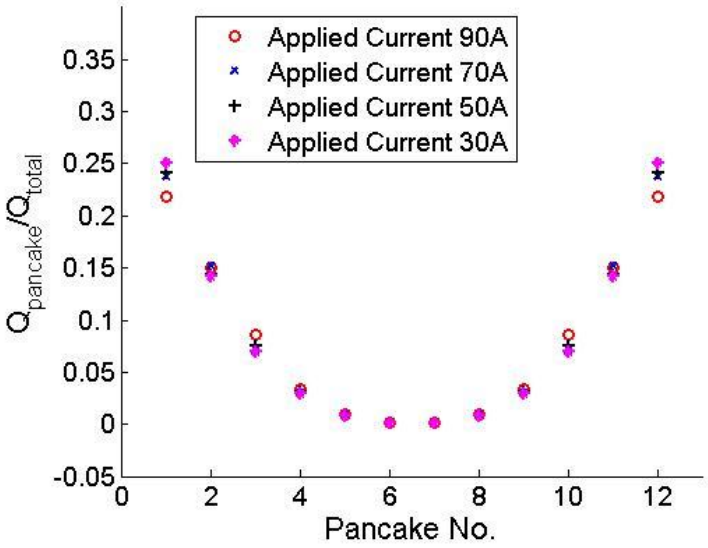

Figure 6-7 The normalized AC loss distribution in the Design 2 coil with different applied currents. $Q_{pancake}$ denotes the AC loss in each pancake, while Q_{total} represents the total AC loss in the coil.

6.1.5 Current lead and cooling system design

Current leads connect the superconducting coil to the room temperature power supply, which brings in heat from the ambient surroundings. Current leads are made from brass for their balanced conductivity between current and thermal flow.

The aim for current lead design is to minimize the heat transferred along the lead. Heat sources can be divided into two parts: the heat due to the resistance and the heat flow due to the difference in temperature between the two ends. The high temperature end is at 300 K, while the low end is at 65 K. According to [10], thermal conduction along the lead can be minimized when the length/cross-area ratio of the conduction cooled current lead has the relation:

$$\frac{l}{S} = \frac{\left(\frac{C\Delta T}{\rho}\right)^{0.5}}{I} \qquad \text{Equation 6-4}$$

where l is the length of the current lead, S is the cross-sectional area, C is the average thermal conductivity of the lead material, ΔT is the temperature difference between the warm and cold ends, and ρ is the electrical resistivity of the lead material. The minimum thermal flow through the current lead can be calculated as:

$$Q_{lead} = 2I\sqrt{\rho C \Delta T} \qquad \text{Equation 6-5}$$

According to Equation 6-5, the heat conduction through the current lead is 9 W. Cooling and thermal insulation systems are needed to maintain the cold temperature necessary for operation of the SMES. The total thermal load of the cryogen magnet includes four components:

1. Conduction loss in the coils. This can be calculated using the *E-J* power law. The loss is the product of the voltage and the current, where the voltage is solved by the current and the *n* value.

2. Radiation between the coil and the steel shell, i.e. heat flux through the vacuum. Based on the configuration of the cooling system in Figure 6-8, the radiation loss can be calculated.

3. Thermal conduction through the current lead.

4. Other thermal load through the mechanical support components. This part is estimated based on the configuration of the mechanical components.

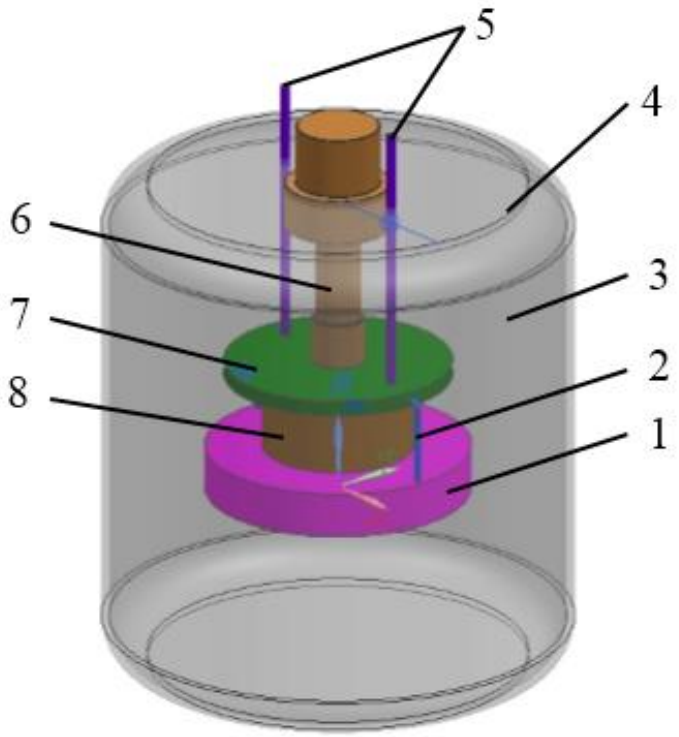

1. Superconducting coil; 2. Current lead (2nd stage); 3. Vacuum; 4. Dewar case; 5. Current lead (1st stage); 6. Cryocooler coldhead; 7. Cold plate; 8. Cold tube

Figure 6-8 Schematic of the cooling and thermal insulation system.

All the thermal loads are listed in Table 6-5. The total thermal load in the SMES was 28 W. Assuming that an efficiency of a cryogenic refrigerator is 20, the power of the refrigerator should be more than:

$$P=20\times28W=560W$$

Table 6-5 Thermal loads for the 60 kJ SMES

Thermal load	Value (W)
Conduction loss	8
Radiation flow	3
Current lead flow	9
Holder flow	8
Total	28

6.2 Applications for renewable energy

The formation of a hybrid energy storage combining a battery and SMES system, offers many benefits that will enable the system to make full use of the special properties of both technologies [131]. Firstly, such a combined system can be used to level the frequent fluctuations of output power on a short time scale, and to time shift energy over a longer term basis with a substantially reduced number of charge/discharge cycles and thus extending the battery life. Secondly, the system will also significantly reduce the volume of usage of electrochemical batteries in renewable energy integration. In addition, the size and the power losses of the main storage system will be considerably reduced. Therefore, several hybrid energy storages are under investigation to evaluate this technology for integration into renewable energy systems.

6.2.1 SMES in hybrid energy systems

A hybrid energy storage system using 60 kJ SMES and 15 AH (Amps*Hour) Li-ion battery is designed to balance the output power of a 10 kW wave generator. The DDLWEC generates electricity with varied frequency and amplitude. The generated AC power from DDLWECs is rectified to DC by an AC/DC converter as shown in Figure 6-9.

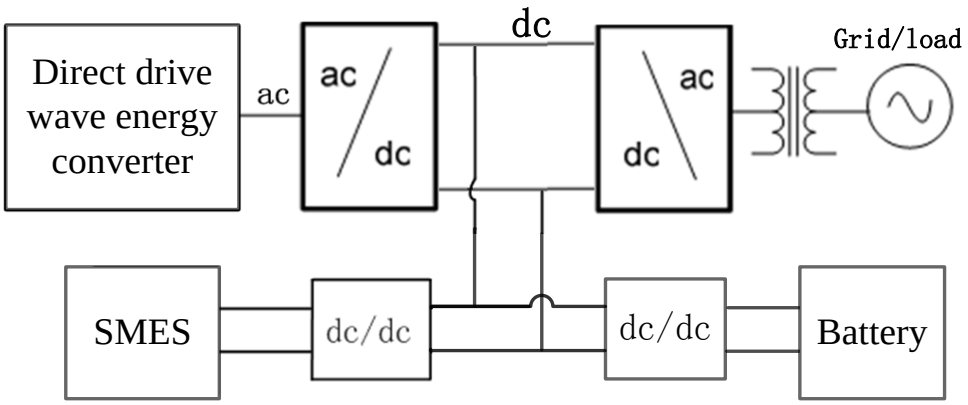

Figure 6-9 A microgrid system of DDWECs with a hybrid energy storage system.

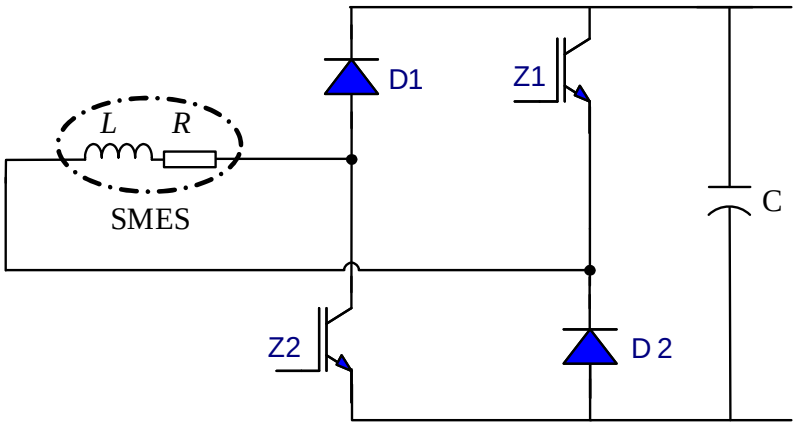

(a)

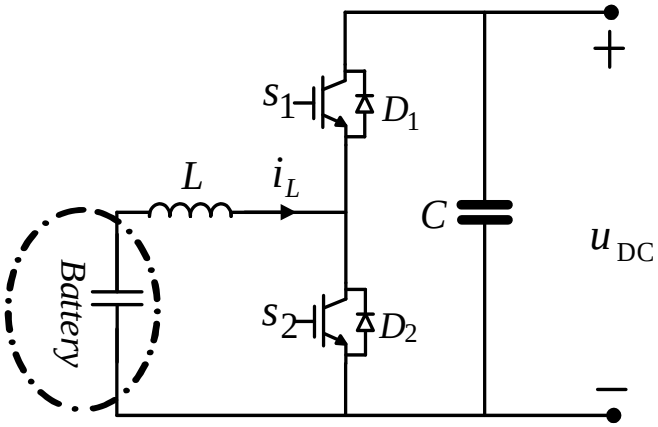

(b)

Figure 6-10 A microgrid system of DDWECs with a hybrid energy storage system.

The SMES and battery need to use different DC/DC interface circuits for exchanging energy with the DC link, as shown in Figure 6-10. When the DDLWEC generates excessive power, the interface circuits control the SMES and battery to absorb the redundant power from the DC link and maintain the desired DC link voltage. When the

DDLWEC generates power that is smaller than the load demand, the interface circuits control the SMES and battery to release power to meet the load demand and maintain a constant DC link voltage.

Figure 6-11 shows the output waveforms of a particular DDLWEC driven by a wave, which has 1.2 m amplitude from 0–5 s, 0.8 m from 5–15 s and 1.2 m from 15–20 s. The fluctuating power from the DDLWEC is smoothed out at the DC link by the hybrid energy storage system, thus a stable output power can be further converted and dispatched to the grid or local load.

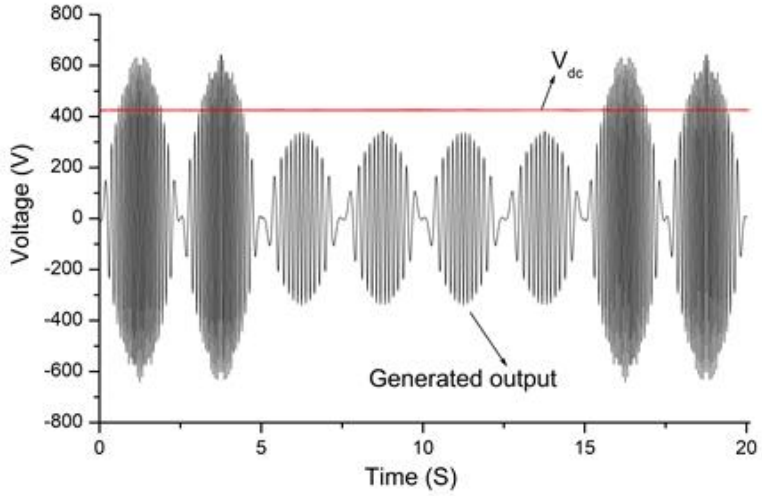

Figure 6-11 Simulation results of the generator waveforms and maintained DC link voltage.

6.2.2 Battery lifetime model

The performance and lifetime of battery in energy storage system are important aspects of renewable based energy systems. And batteries usually make up the major expenditure when considering the whole lifecycle cost of the system. Precise prediction of the battery lifetime can, therefore, enhance the viability and stability of the system over the long term.

The available capacity of all batteries drops during the charging/discharging processes. Failure of the battery is usually marked when the capacity of the fully charged batteries decreases to a predefined value, such as 80% of the original capacity. This degradation results from the wearing out of the cathode when the ions flow between the cathode and the anode. Battery calendar-life ageing is also heavily dependent on cell

chemistry, battery type and temperature. Avoiding a frequent charging/discharging process can therefore enhance the lifetime of a battery.

Two approaches are common in studying the lifetime of batteries. The first is based on experiments. Repeated charging/discharging cycles can be performed and the cycles are counted until the batteries fail. This approach can provide the detailed voltage and current relationships under different condition and form the basis for theoretical analysis. However, the experimental process requires a large investment of money and time, which limits the scope of usefulness. The second approach uses experimental data to simulate the battery lifetime. The simulation approach has the advantages of being efficient and economical. This research uses the simulation method to verify the benefit of an SMES/battery hybrid energy storage system.

There are several methods that can be used to characterize the lifetime of batteries. The first, known as "the FhG model" [132] employs an equivalent circuit to simulate the working process of batteries with the stated variables, such as voltage and internal resistance. In this way, the degradation in battery performance can be quantified to estimate the battery lifetime. The model varies significantly from the others considered due to its complexity and the need for input parameters and empirical test data.

The second type of model is the cycle-counting model. This model is based on the assumption that the amplitude of a charge cycle determines the fraction of the battery lifetime consumed during the cycle. The consumed lifetime fraction can be derived from the battery life curve against the magnitude of discharge. Therefore, the lifetime aging should be calculated by summation of the contribution of individual charge/discharge cycles at their corresponding depths of discharge.

Binder examined the results of real-life batteries and concluded that the FhG model significantly overestimates the battery lifetime when deployed with real renewable energy system data [132]. In contrast, the much simpler cycle counting algorithm provides a better prediction of battery lifetime with the same test data. Thus, the cycle counting method is used in this research and the FhG model is not considered any further.

The depth of discharge, *DOD*, in a battery reflects the changes in battery capacity, defined as the ratio of the released charge and the total capacity:

$$DOD = \frac{Q_I}{C_I}$$ Equation 6-6

where Q_I is the released charge from the battery, and C_I is the capacity of the battery with the discharging current I. Another parameter which denotes the remaining charge in the battery is the state of charge, SOC. The SOC can be derived from the DOD as:

$$SOC = 1 - DOD = 1 - \frac{Q}{C_I}$$ Equation 6-7

Figure 6-12 (a) shows a typical plot of cycles-to-failure against the depth of discharge for a typical lead-acid battery using the datasheet data. One problem is that manufacturers' datasheets [133] do not provide information for cycle ranges less than 0.1, so it is necessary to extend the battery life curve shown in Figure 6-12 (b). The existing manufacturer's data was extrapolated as a straight line on a log/log scale by using the final gradient of the curve at the last manufacturer's data point to extend to cycles in the range $<10^{-3}$, which was proposed by Ruddell et al. [134].

The equation of the curve that fits the extrapolated data is a logarithmic polynomial of the formula:

$$C_d = a_1 d^{-1} + a_2 d^{-2} + a_3 d^{-3} + a_4 d^{-4}$$ Equation 6-8

where C_d denotes the number of cycles-to-failure for a depth of discharge d. The fitting coefficients a_1 to a_4 are:

$a_1 = 601.5$

$a_2 = -0.001507$

$a_3 = 1.495 \times 10^{-7}$

$a_4 = -1.345 \times 10^{-12}$

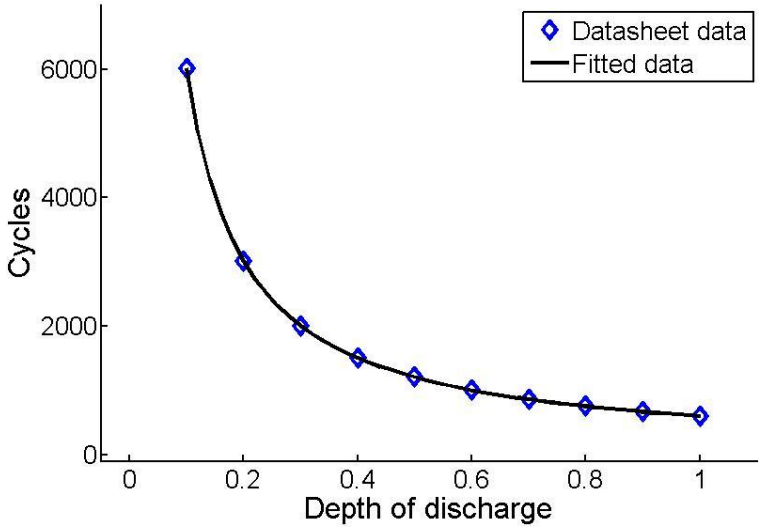

(a)

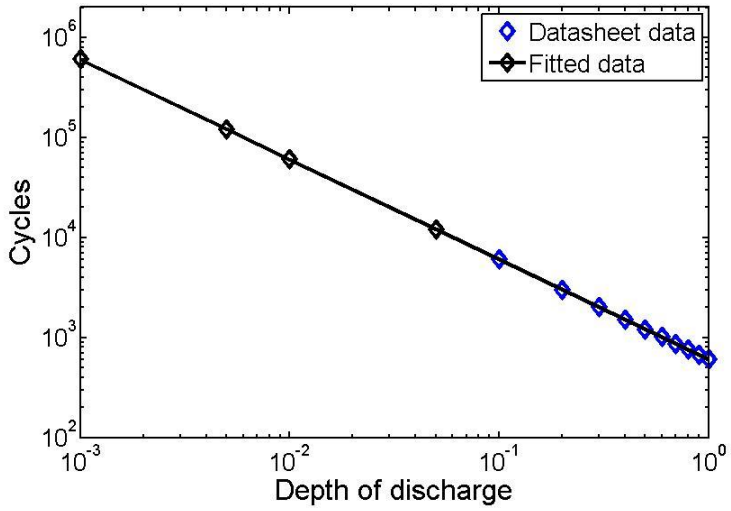

(b)

Figure 6-12 (a) The charge/discharge times against depth of discharge for a typical battery; (b) The extrapolated curve of a typical battery in a logarithmic scale.

6.2.3 Rainflow counting method

The key issue in determining the battery life with the cycle-counting model is how to identify the charging/discharging cycles. This is more challenging considering the random fluctuations in the output of renewable energy generation. The rainflow counting method is widely used to convert a complex load spectrum into simple patterns [135, 136]. The rainflow counting algorithm is used in the analysis of fatigue data in

order to reduce a spectrum of varying load into a set of basic load reversals. It was first proposed for analysis of the fatigue process of metallic materials in engineering structures. The rainflow counting method was later used for lifetime predictions of batteries, and good agreement was obtained between experiments and theoretical calculations.

Using the rainflow counting method to predict the lifetime of a battery involves two assumptions:

1) The loads are independent and the order of the loads does not matter to the lifetime consumption.

2). The cumulative damage model for battery failure caused by the charging/discharging process can be described by Miner's rule [137]. This means that the battery life consumption C_{test} during a certain test can be approximated by:

$$C_{test} = \sum_{i=1}^{k} \frac{n_i}{N_i} \qquad \text{Equation 6-9}$$

where N_i is the total number of cycles to failure at the ith depth of discharging, and D_i, n_i is the number of cycles accumulated at D_i .

Figure 6-13 presents the general process to determine the cycles using rainflow counting methods. These cycles include two categories: full cycles and half cycles. Two corresponding half cycles can be merged into one full cycle. These cycles are allocated into different groups by the magnitude of the depth of the discharge. Thereby, the numbers of simple charging/discharging cycles can be extracted from the complex loading profiles.

There are several software packages available to carry out rainflow counting procedures to predict the lifetime during the fatigue or aging. This section selects the code based on the MATLAB platform [138]. This code was prepared according to the ASTM standard and optimized considering the calculation time. The algorithm takes an array of preprocessed state-of-charge variations as the major input.

The rainflow counting method can count the number of simple loads with different magnitudes in complex conditions. With these simple loads, the total battery life time can be predicted using:

$$T_{total} = \frac{T_{test}}{C_{test}} \qquad \text{Equation 6-10}$$

where T_{total} is the estimated battery lifetime, T_{test} is the period length of the test, and C_{test} is the lifetime consumed during the test period T_{test}.

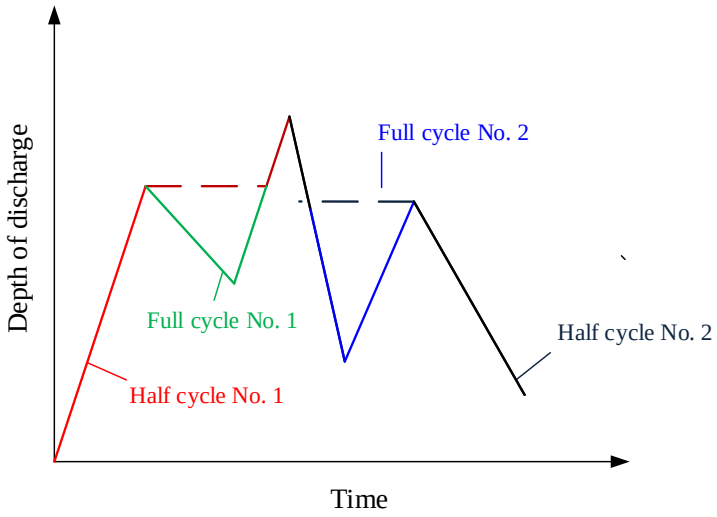

Figure 6-13 A simplified example to demonstrate rainflow cycle-counting algorithm.

6.2.4 Application in wave generation systems

Figure 6-9 presents a wave power generating system with a hybrid energy storage system. The SMES and battery are connected to the bus via a DC/DC converter to absorb and release energy, thereby compensating for the fluctuation in the output of the renewable energy power generation and maintaining the stability of the grid. In this wave generation system, the role of the hybrid energy system is to smooth the power fluctuations, where the SMES can smooth high-frequency power fluctuations and the battery energy storage can smooth low frequency fluctuations.

Figure 6-14 is the output power of a wave generator in 18 minutes where the rated power of the generator is 2 kW. In order to simplify the calculation, the voltage of the output is assumed to be 400 V. Hybrid energy storage systems act as a supplement to the generator and stabilize the bus voltage. Thus the generator and the energy storage system can be regarded as a generator with constant power and voltage.

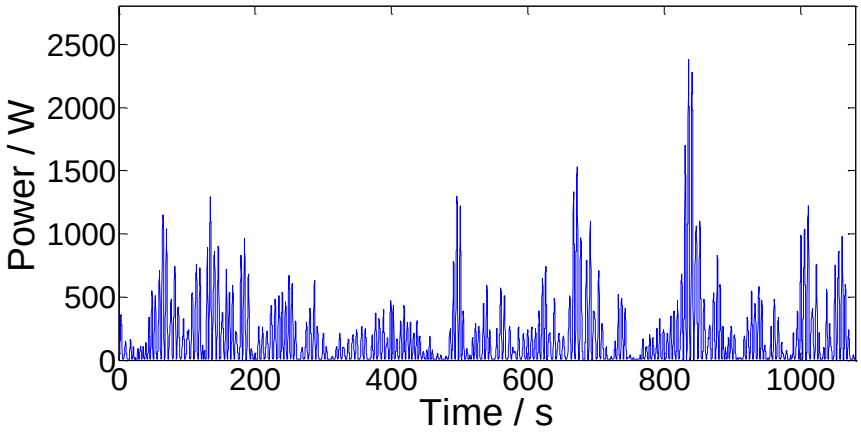

Figure 6-14 The output profile of a wave generator within 18 minutes.

The basic idea of a SMES—battery hybrid energy system is that the low frequency portion is absorbed or released by the battery, while the SMES handles the high frequency portion, which is shown in Figure 6-15. The fluctuation of the power output is filtered to seprate the high frequency part and low frequency part. The current curve is then converted into the battery *SOC* (state of charging) curve, and finally through the raindrops algorithm so that the data for charging and discharging cycles can be calculated.

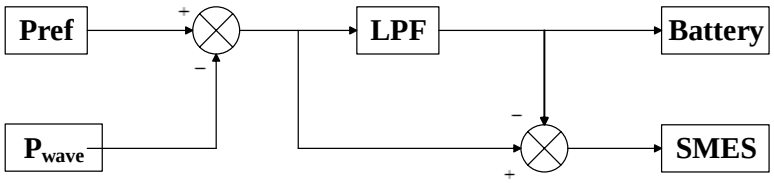

Figure 6-15 The power allocation algorithm for a hybrid energy system.

6.2.5 Results and Analysis

Figure 6-16 and Figure 6-17 compare the results of an energy storage system, including the charging/discharging curve, the SOC curve and the histogram of the cycles against different DODs. Figure 6-16 presents the battery only system, while Figure 6-17 shows the battery/SMES hybrid energy system with a filter time constant of 0.01 Hz.

In terms of battery current, two major differences can be observed. Firstly, the peak value of the hybrid system is relatively smaller than that of battery only system. Secondly, the battery current in the hybrid energy system undergoes significantly fewer polarity reversals. There are more than 100 total cycles in Figure 6-16 (c), whereas there are fewer than 6 charging/discharging cycles in Figure 6-17 (c). Consequently, the

battery in the hybrid energy storage system experienced not only lower DODs but also fewer charge/discharge cycles.

The prediction of battery lifetime for each system was calculated using the novel battery lifetime model in Figure 6-18. The batteries in a battery only system can be used for 96 hours, whereas in a hybrid energy system the battery lifetime can achieve a three times increase, reaching as high as 464 hours. A lower cut off frequency will generate a larger extension of battery lifetime, as shown in Figure 6-18. However, a lower cut off frequency requires a larger sized SMES, which means a higher initial investment and greater power losses. So the selection of lower cut off frequency needs some consideration to balance the AC losses and battery life extension.

6.3 Rough estimation of costs of SMES with different energy scale

Although many superconducting demonstration projects have been carried out for power system applications and their technical feasibilities are widely accepted, very few have been used commerically. One of the major obstructions is the economical consideration. For LTS-related projects, achieving a cooling temperature of 4 K is expensive, due to the scarcity of liquid helium. For HTS applications, the economic consideration is centred on the material cost of superconductors, since the fabrication of 2G HTS conductors is not yet mature and the price of 2G HTS is tens of times expensive than LTS. Thus, further analysis on the cost of HTS SMES systems is necessary for their future application.

The cost estimation of HTS SMES varies greatly depending on the designed capacity of the project, the status of the specific technology, as well as the particular materials. A standardized cost-breakdown structure for energy storage systems that would allow researchers to objectively compare the cost/benefit aspects of various storage technologies has been proposed by Sandia Laboratory [139]. According to this method, the cost of certain SMES system consists of three key components: superconductors, power conditioning system (PCS) and cryogenic system.

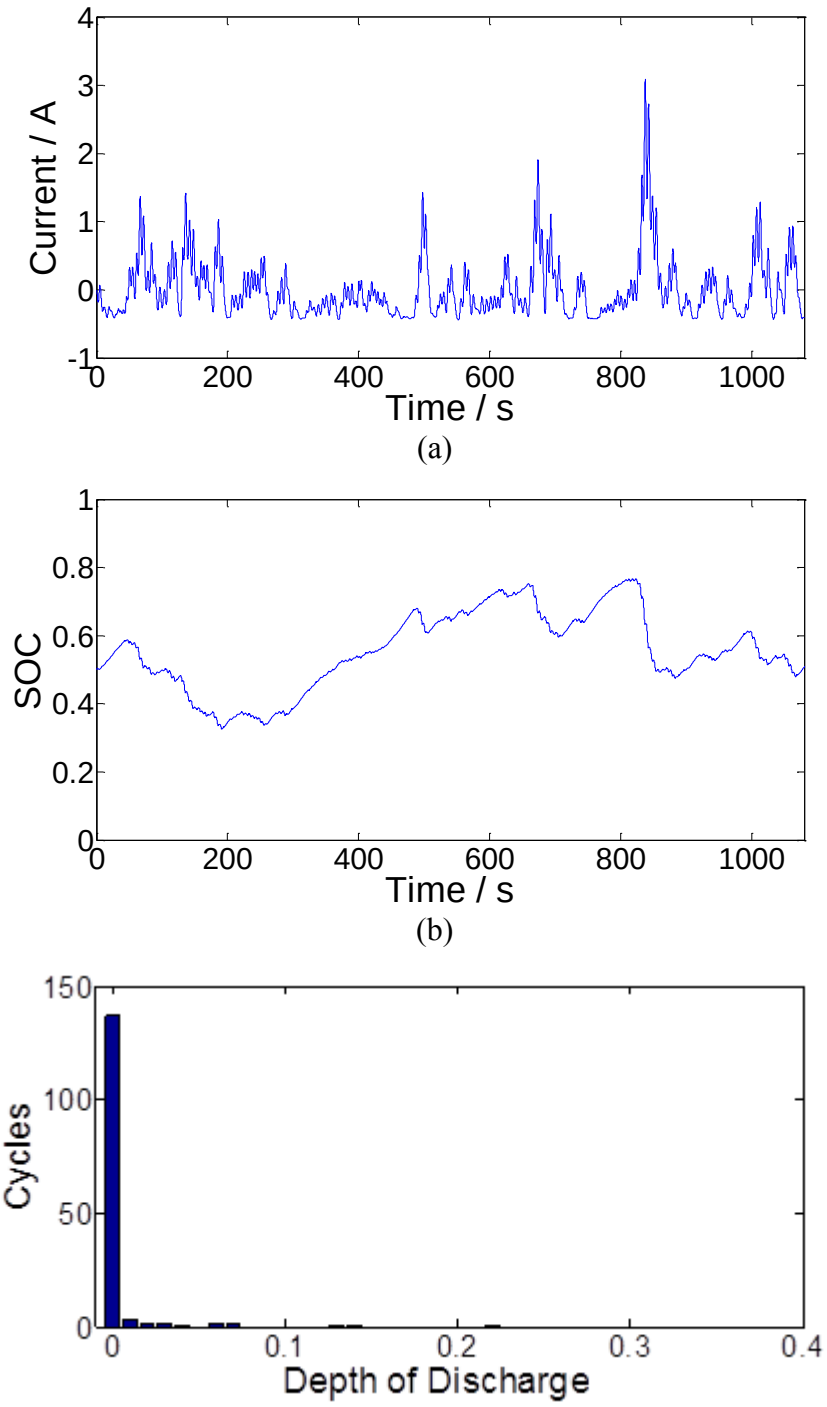

Figure 6-16 Results for a battery only system: (a) Current curve; (b) SOC curve; (c) Histogram of cycles vs depth of discharge.

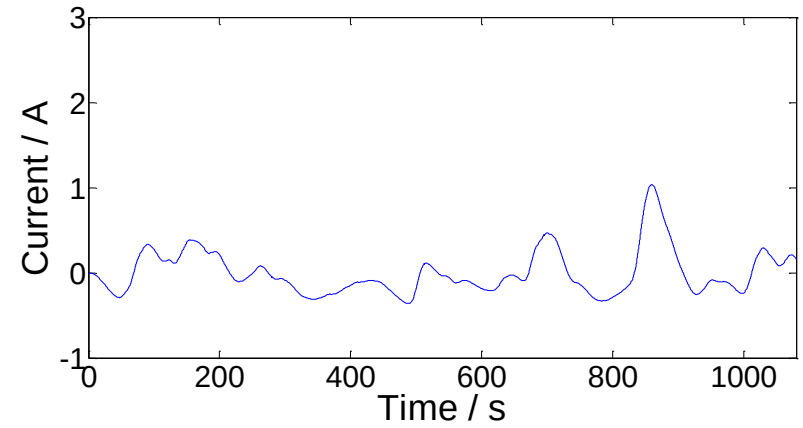

(a)

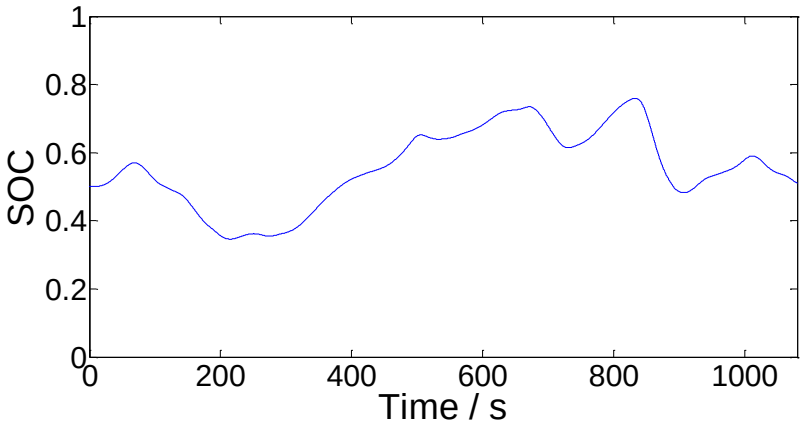

(b)

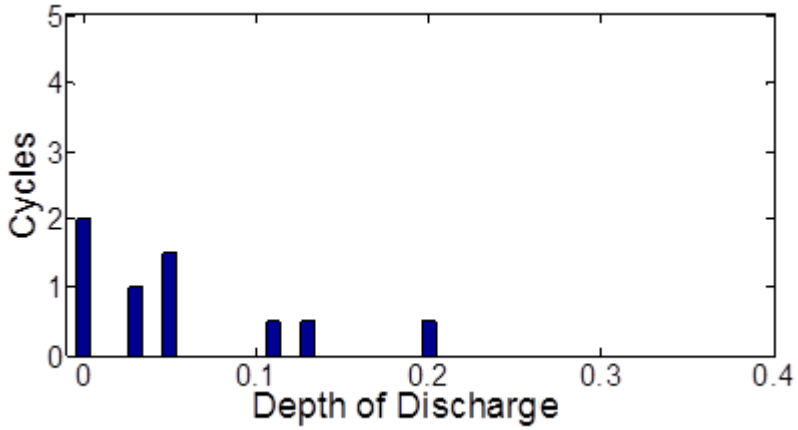

(c)

Figure 6-17 Results for a time constant of 100 s: (a) Current curve; (b) SOC curve; (c) Histogram of cycles vs depth of discharge.

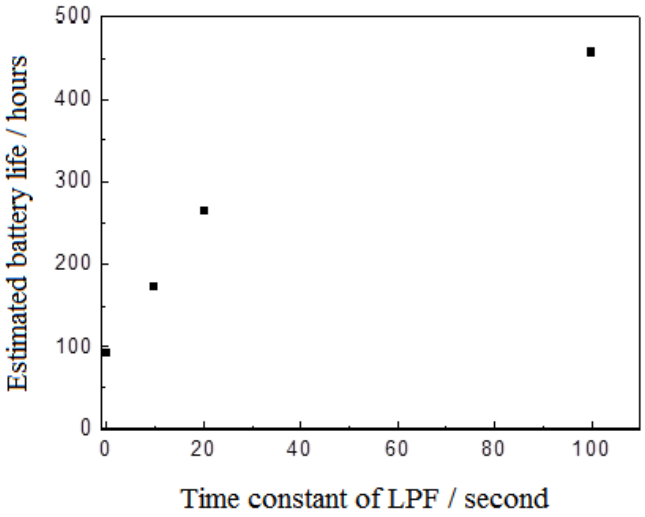

Figure 6-18 The estimated battery lifetime with different filter time constants.

To understand how some of the components of SMES affect the cost, the group at the University of Wisconsin established the empirical scale law which describes how various magnet parameters are related to the magnetic field intensity (*B*) and stored energy (*E*) [140]. Cost components based on the scaling law for LTS SMES projects were plotted and can be used to guide the design process. An analysis of SMES costs was discussed in [139] based on two real projects: a commercial 8 MJ SMES developed by Superconductivity, Inc. and a 1,350 MJ SMES (375 kwh) in Anchorage. The commercial 8 MJ SMES revealed that the magnetic storage, PCS and balance of plant cost of this system accounted for approximately 30%, 30% and 40% of the total project cost, respectively. Schwartz J. estimated the cost of the International Thermonuclear Experimental Reactor (ITER) magnet system developed at Lawrence Livermore National Laboratory. This magnet held an energy of 43 GJ and the total cost was about $200 million[141].

This section aims to discuss the economic aspects of 2G HTS SMES with different energy scales: kJ, MJ and GJ. This discussion includes two parts: magnet configurations and energy capacities. In order to simplify the analysis, the assumption is that the cost only considers material cost of the superconductor. This is a reasonable assumption for YBCO conductors since the price is ten times more expensive than LTS conductors, making material consume most of the budget for large systems, and at the same time the cooling of 2G HTS is much cheaper.

6.3.1 Coil structure design

There are two types of SMES magnets: solenoid configuration and toroid configuration. The unit cell of an SMES magnet is a double pancake coil as shown in Figure 6-19 [113]. In many small-scale and medium-scale SMES systems the solenoid configuration is preferable because it stores more energy than a toroidal SMES using the same amount of superconductor. The simple structure also makes it easier to manufacture. A drawback of the solenoid configuration is the stray field, which is a leakage magnetic field that presents threat to environment and human health. However, for small SMES, the stray field is not a major conern.

Figure 6-19 Schematic view of a double-pancake coil.

In a toroidal configuration several double pancake coils are placed in a circle, such as Figure 6-20. The magnetic field has been constrained within the coil, and therefore the stray magnetic field is significantly reduced. In this paper the SMES system is modelled as eight double pancake coils placed in the circumference of a circle with equal spacing between them to simplify the simulation work of the toroidal configuration.

Figure 6-20 Illustration of toroidal SMES configuration.

The AC/DC module of COMSOL is good at tackling electro- and magnet-related problems, and at providing access to any derived field quantities and unlimited couplings to other physics. In this section, the AC/DC model in COMSOL is used to simulate various types and sizes of magnets, which is convenient for modelling the electrical and magnetic field. Figure 6-21 shows the magnetic field of solenoidal MJ and toroidal MJ SMES.

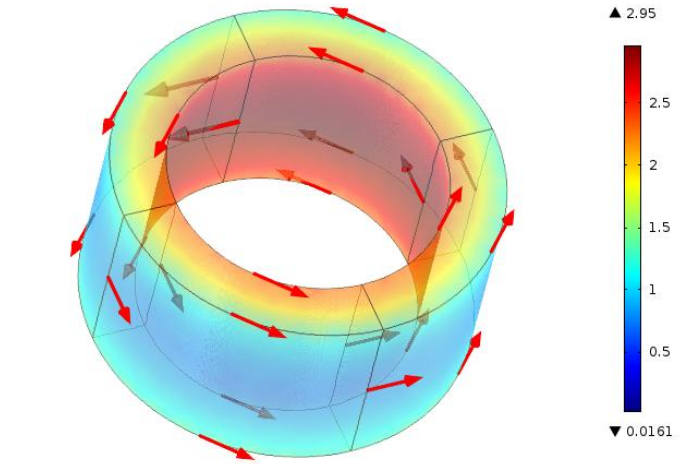

(a)

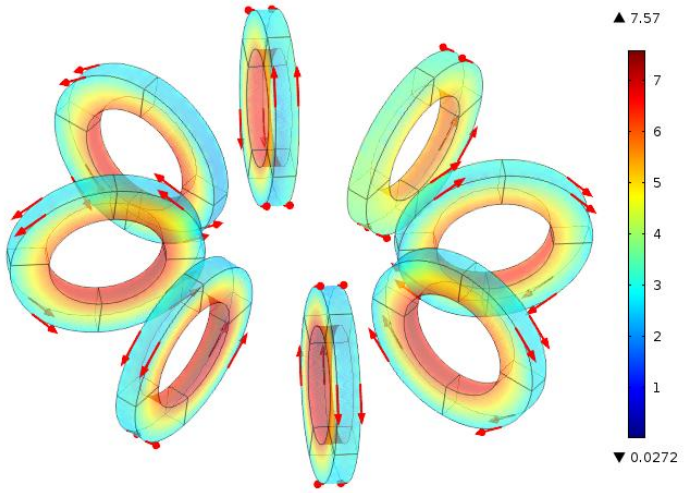

(b)

Figure 6-21 Magnetic field for an MJ-scale SMES, in which arrows represent the current flow. (a) Solenoid configuration; (b) Toroid configuration. (Unit is T)

For a small-capacity superconducting magnet the solenoid type configuration will be the prime consideration, because the magnetic field is small and the stray field is easy to handle. The simulation result shows that a bigger radius helps to reduce the maximum magnetic field and increase the storage capacity for solenoidal coil. However, more superconductors are required as the coil radius increases. Applying a larger current into

a conductor is an efficient way to increase the stored energy. But the maximum possible current is limited by the magnetic field produced by the current. Thus, an optimization process is necessary and it is implemented as shown in Figure 6-2.

For a medium or large SMES system, a toroidal configuration is a better option. This is because the modelling result indicates that a greater energy capacity could be achieved by a bigger radius of the toroid magnet, which would also reduce the magnetic flux density at the same time. However, more supporting structure materials and cryogenic costs would be required.

According to Table 6-5, the magnetic field in a toroid magnet is much larger than that of a solenoid magnet. This is because a toroid can constrain the magnetic flux inside the magnet and achieve a higher magnetic energy density. The unit cost per quantity of stored energy decreases when the stored energy increases from kJ scale to GJ scale. Therefore, for a small SMES a solenoid configuration is a better option due to its simple structure and low magnetic field. For a large SMES, the toroid configuration is better since it has a significantly lower stray magnetic field and a higher energy density.

Table 6-6 Current and maximum magnetic field in different SMES

Parameter	**1.2 kJ (solenoid)**	**1.6 MJ (solenoid)**	**1.3 MJ (toroid)**	**1 GJ (toroid)**
Current density (A/m^2)	2.5×10^8	2.05×10^8	1.00×10^8	5.3×10^7
Critical current (A)	300	250	120	64
Maximum Field (T)	1.91	2.9	7.6	14.3
Operating Temperature	65 K	65 K	65 K	65 K

6.3.2 Cost analysis

The specifications of the SMES magnets are shown in Table 6-6. According to Superpower Inc, the cost of a 12 mm wide YBCO tape is 85 $/m. Hence, the total expense of the tapes is calculated and shown in the table above. In Table 6-4, only the costs of the superconductors are presented. The unit costs for kJ, MJ (solenoid and toroid configuration) and GJ are $1,160 /kJ, $640 /kJ, $330 /kJ, and $45 /kJ, respectively,

showing that as the energy increases, the unit price of SMES systems decreases significantly.

Due to the scope of this thesis, a complete analysis is not done. But for future reference, a complete economic analysis will include life cycle cost estimation, which consists of capital cost, operating cost and maintenance cost. For the capital cost, two main parts need to be considered: energy capacity-related cost and power conversion-related cost. The former consists of the capital and construction costs of the superconductors, magnet structure components, cryogenics, protection systems, and control circuits. The latter is the cost of a required power electronics circuit. For different practical situations, different power electronics circuits are required. It is worth including all these factors in the calculations for a complete estimation.

Table 6-7 Specficiation and cost of different scales of SMES systems

Parameter	**1.2 kJ (solenoid)**	**1.6 MJ (solenoid)**	**1.3 MJ (toroid)**	**1 GJ (toroid)**
Inner radius (cm)	4.5	20	8	34
Outer radius (cm)	6.8	28	12	86
Height (cm)	2.4	12	-	-
Total length of tape (km)	0.17	12	5	533
Cost (USD)	1.4×10^4	1.02×10^6	4.25×10^5	4.5×10^7
Unit Price ($/kJ)	1 160	640	330	45

6.4 Summary

In Chapter 6, primary studies for applying superconducting magnets in energy storage systems were carried out. The optimal configuration of a 60 kJ SMES for a wave generator was achieved based on an electromagnetic field simulation. The stress due to the Lorentz force in the coil was calculated. Current leads were designed to minimize the thermal flow. The schematic chart of the cooling and insulation system was presented and the required cryocooler power was calculated. A hybrid SMES-battery energy storage system could be used to flatten out the power fluctuation of wave energy converters and ensure that a stable power output was dispatched to the grid or local load.

The control circuit was presented, and the simulation result showed that the fluctuating power from the DDLWEC was smoothed out at the DC link by the hybrid energy storage system.

The hybrid energy storage was analysed to discuss extension to the lifetime of the battery component. A low pass filter (LPF) with specified time constant was used to allocate the power between the battery and the SMES. The rainflow counting method was employed to calculate the number of cycles that the battery experienced during the test period. The battery life model was fitted from the data sheet. Our result showed that the battery life can be extended by four times with the help of the SMES system.

Different SMES systems were designed using YBCO tapes for different scales of energy capacity (kJ, MJ and GJ). The magnets of the SMES systems were designed using the global optimization algorithm, which took into account the properties of the YBCO tapes. Two types of SMES configurations were compared. It was shown that the solenoid configuration was easy to manufacture and install while having a large stray magnetic field, and was more suitable for small scale SMES systems. The toroid configuration confined the stray field inside the magnet, and was therefore more suitable for large SMES systems. The unit cost of energy for a SMES system was about 1200, 330, and 45 $/kJ for kJ, MJ and GJ SMES, respectively. The cost per unit energy ($/J) falls as the stored energy in a system increases.

Chapter 7. Conclusion and future work

7.1 Conclusion

This thesis has studied superconducting coils with coated conductors experimentally and numerically, as well as their application in energy storage systems. This study has been performed in four steps: from a tape to a single coil, to multiple coils, and finally to a conceptual SMES system. The research has addressed two technical challenges: how much current the 2G HTS coils can carry, and how much heat they generate under AC conditions. The first issue is related to the critical current prediction of the system, which determines the performance and cost of the whole device. The second issue involves the cryogenic design and safe operation of the system. With these two issues being properly analysed and evaluated, a conceptual design of a 60 kJ SMES was performed as a case study.

Chapter 3 studied the 2G HTS tapes which were used to fabricate superconducting coils. Firstly, the critical currents of different tapes under external magnetic fields were measured and these data were fitted using the Kim model. The field dependency of the *n*-value was also discussed, and it was found that the *n*-value decreases when the external magnetic field increases, similar to the magnitude of the critical current. This similarity was discussed based on the flux flow theory. The second part of Chapter 3 showed that Gallinstan hardly degraded the tape, while resins resulted in different degrees of degradation. Comparatively, Stycast Black caused slight degradation in the tape, however, the other two resins, Stycast 1266 and Araldite, degraded the tapes substantially. The degradation was closely related to the mismatch in thermal expansion.

In chapter 4, a fully multiphysics model of 2G HTS coils was proposed and validated using magnetic energy minimization, based on homemade finite element analysis code. This method coupled the magnetic energy minimization with magnetic, thermal and mechanical fields for the first time, and efficiently simulated the superconducting coils

using fewer elements and avoiding high non-linearity. The critical current and AC losses of the 2G HTS coils could be calculated accurately and efficiently. This model can be used to analyse the thermal and mechanical processes when the superconducting coil charges and discharges. Finally, the load line method for calculating the critical current of a coil was extended to the consideration of anisotropy in 2G HTS. The averaged normalized magnetic field was used to define the load line, and this new method gave very good critical current estimation.

Chapter 5 presented efficient numerical modelling of a stack of HTS pancake coils with thousands of turns using the line front track approximation. Accurate current distribution, magnetic field and AC losses were calculated and compared to established H-formula methods. We further analysed the screening current and the AC losses in different pancakes, finding that the majority of the losses are generated in the top and bottom coils. This method was further applied to a real 2G HTS SMES design for the first time. Key parameters, such as operating temperature, pancake radii, and gaps between neighbouring pancakes were compared based on the AC losses and stored energy simulation results.

Finally Chapter 6 presented a design for hybrid energy storage using an SMES system and battery. The full details were presented for the design of a 60 kJ SMES. The electromagnetic and mechanical fields were calculated using the line front approximation. This SMES was applied to a renewable energy system. Extension of the battery lifetime with the use of SMES in a hybrid energy system was discussed using the rainflow counting method. A rough cost estimation of the SMES system with different energy scales was presented and discussed. It was shown that the solenoid configuration was easy to manufacture and install while having a large stray magnetic field, and was more suitable for small scale SMES systems. The toroid configuration confined the stray field inside the magnet, and was therefore more suitable for large SMES systems.

7.2 Future work

Although some conclusions have been drawn in this thesis, further efforts are necessary for the future application of 2G HTS superconducting technologies.

In Chapter 3, field dependencies of critical current and n value of 2G HTS tape were investigated theoretically and experimentally, however, further work is needed to apply these results to the E-J power law in numerical simulations and to discuss their influence. For coil fabrication, the impregnation method should be researched more quantitatively to control the impregnation process. The impregnation material should be further applied to the coil to test the effects of I_c degradation and winding techniques. The differences in AC losses in the impregnated tapes should also be investigated further.

Chapter 4 implemented the simulation of a single coil under a self field and an external field, more work is needed to speed up the simulation. This can be approached by using a homogenization technique. For a superconducting coil with complex shapes, such as racetrack coils in electric machines, a 3D modelling technique is necessary. Another interesting work is to extend the magnetic energy minimization to non-insulated coils. Balancing the precision and the complexity of calculation is another issue worthy of deep consideration. It was demonstrated that the line front track approximation is efficient and accurate in a magnetic field for AC losses calculation, however additional work is necessary to optimize the parameters in the model, in order to further optimize the model.

Chapter 6 outlined the general process of designing an SMES system and presented a preliminary study of superconducting coil application. For practical SMES design, special attention is needed for the joint technique and the voltage insulation. The quench process simulation and the protection scheme are also very important in the design stage. For battery life time extension, more typical fluctuation curves, including wind and solar, should be applied to validate the algorithm for renewal energy systems.

Publications

1. **Zhang, H**., Yuan, W. etc., 2013.Design and simulation of SMES system using YBCO tapes for direct drive wave energy converters. IEEE Transactions on Applied Superconductivity, 23 (3), 5700704.

2. **Zhang Huiming**, Zhang M, Yuan W. Measurement and calculation of critical current and transport AC loss in YBCO pancake coils. IEEE Transactions on Applied Superconductivity(Accepted)

3. Zhu J, **Zhang Huiming**, Qiu M, Fu S, Zhang M, Yuan W. Electromagnetic Analysis of High Current-Carrying Superconducting Cable Consisted of YBCO Coated Conductor. IEEE Transactions on Applied Superconductivity(Accepted)

4. Zhu, J. **Zhang, H**., Yuan, W. etc., 2013, Design and cost estimation of superconducting magnetic energy storage (SMES) systems for power grids, IEEE on power & energy society

5. Nie, Z., **Zhang, H**. and Yuan, W. etc, 2013. SMES-battery energy storage system for conditioning outputs from direct drive linear wave energy converters. IEEE Transactions on Applied Superconductivity, 23 (3), 5000705.

6. **Zhang Huiming,** Zhang M, Yuan W. Study of 2G HTS Superconducting Coils Using Line Front Track Approximation. IEEE Transactions on Applied Superconductivity (Submitted)

References

[1]*Reducing emissions and preparing for climate change: 2015 Progress Report to Parliament*, 2015.

[2]*UK Renewable Energy Roadmap*, Department for Energy and Climate Change, London, 2011.

[3]*Global Wind Report: Annual market update 2012*, Global Wind Energy Council, 2013.

[4]"http://www.theguardian.com/environment/2012/feb/09/solar-power-ambition-uk," [access online]20151012.

[5]M. Ferrier, "Stockage d'energie dans un enroulment supraconducteur," Proceedings Conference on Low Temperatures and Electrical Power, London, England, pp. 150, 1969.

[6]S. Kalsi, D. Aized, B. Conner *et al.*, "HTS SMES magnet design and test results," Applied Superconductivity, IEEE Transactions on, vol. 7, no. 2, pp. 971-976, 1997.

[7]J. Paasi, R. Mikkonen, T. Kalliohaka *et al.*, "Design and performance of A 5 kJ HTS u-SMES," Advances in cryogenic engineering, vol. 45, pp. 779-786, 2000.

[8]C. J. Hawley, and S. Gower, "Design and preliminary results of a prototype HTS SMES device," Applied Superconductivity, IEEE Transactions on, vol. 15, no. 2, pp. 1899-1902, 2005.

[9]H. Rogalla, and P. H. Kes, 100 years of superconductivity: CRC Press/Taylor & Francis Group, 2012.

[10]S. S. Kalsi, Applications of high temperature superconductors to electric power equipment: John Wiley & Sons, 2010.

[11]N. Atomura, T. Takahashi, H. Amata *et al.*, "Conceptual design of MgB2 coil for the 100 MJ SMES of advanced superconducting power conditioning system (ASPCS)," Physics Procedia, vol. 27, no. 8, pp. 400-403, 2012.

[12]S. Nomura, S. Akita, R. Shimada *et al.*, "Design Considerations for SMES Systems Using and/or High-Temperature Superconductors," IEEE Transactions on Applied Superconductivity, vol. 16, no. 2, pp. 590 - 593, 2006.

[13]Y. Oga, S. Noguchi, and M. Tsuda, "Comparison of Optimal Configuration of SMES Magnet Wound With MgB2 and YBCO Conductors," IEEE Transactions on Applied Superconductivity, vol. 23, pp. 5700204-5700204, 2013.

[14]E. A. Young, J. Pelegrin, I. Falorio *et al.*, “Temperature and Background Field Dependence of a Compact React and Wind MgB2 Solenoid Coil,” Applied Superconductivity, IEEE Transactions on, vol. 25, no. 3, pp. 1-5, 2015.

[15]S. Kwak, S. Lee, S. Lee *et al.*, “Design of HTS magnets for a 2.5 MJ SMES,” Applied Superconductivity, IEEE Transactions on, vol. 19, no. 3, pp. 1985-1988, 2009.

[16]S. Noguchi, M. Yamashita, H. Yamashita *et al.*, “An optimal design method for superconducting magnets using HTS tape,” Applied Superconductivity, IEEE Transactions on, vol. 11, no. 1, pp. 2308-2311, 2001.

[17]D. C. Larbalestier, J. Jiang, ., U. P. Trociewitz *et al.*, “Isotropic round-wire multifilament cuprate superconductor for generation of magnetic fields above 30 T,” Nature Material, vol. 13, no. 4, pp. 375-381, 2014.

[18]S. Foltyn, L. Civale, J. MacManus-Driscoll *et al.*, “Materials science challenges for high-temperature superconducting wire,” Nature materials, vol. 6, no. 9, pp. 631-642, 2007.

[19]C. Bean, “Magnetization of hard superconductors,” Physical Review Letters, vol. 8, no. 6, pp. 250, 1962.

[20]C. P. Bean, “Magnetization of high-field superconductors,” Reviews of Modern Physics, vol. 36, no. 1, pp. 31-38, 1964.

[21]D. Chen, and R. Goldfarb, “Kim model for magnetization of type-II superconductors,” Journal of Applied Physics, vol. 66, no. 6, pp. 2489-2500, 1989.

[22]M. Tinkham, Introduction to superconductivity: Courier Corporation, 2012.

[23]F. London, and H. London, "The electromagnetic equations of the supraconductor." pp. 71-88.

[24]V. L. Ginzburg, “Nobel Lecture: On superconductivity and superfluidity (what I have and have not managed to do) as well as on the “physical minimum” at the beginning of the XXI century,” Reviews of Modern Physics, vol. 76, no. 3, pp. 981, 2004.

[25]L. N. Cooper, and D. Feldman, BCS: 50 years: World scientific, 2011.

[26]J. Nagamatsu, N. Nakagawa, T. Muranaka *et al.*, “Superconductivity at 39|[thinsp]|K in magnesium diboride,” Nature, vol. 410, no. 6824, pp. 63-64 (1 March 2001) | doi :10.1038/35065039, 2001.

[27]S. Solutions, "Basic research needs for superconductivity." p. 11.

[28]W. Norris, “Calculation of hysteresis losses in hard superconductors carrying ac: isolated conductors and edges of thin sheets,” Journal of Physics D: Applied Physics, vol. 3, no. 4, pp. 489, 1970.

[29]E. H. Brandt, and M. Indenbom, “Type-II-superconductor strip with current in a perpendicular magnetic field,” Physical Review B, vol. 48, no. 17, pp. 12893, 1993.

[30]F. Grilli. "[Lecture Note]http://www.ims.kit.edu/english/327_1357.php."

[31]F. Grilli, S. Stavrev, Y. Le Floch *et al.*, “Finite-element method modeling of superconductors: from 2-D to 3-D,” Applied Superconductivity, IEEE Transactions on, vol. 15, no. 1, pp. 17-25, 2005.

[32]N. Amemiya, S.-i. Murasawa, N. Banno *et al.*, “Numerical modelings of superconducting wires for AC loss calculations,” Physica C: Superconductivity, vol. 310, no. 1, pp. 16-29, 1998.

[33]Z. Hong, A. Campbell, and T. Coombs, “Numerical solution of critical state in superconductivity by finite element software,” Superconductor Science and Technology, vol. 19, no. 12, pp. 1246, 2006.

[34]R. Brambilla, F. Grilli, and L. Martini, “Development of an edge-element model for AC loss computation of high-temperature superconductors,” Superconductor Science and Technology, vol. 20, no. 1, pp. 16, 2007.

[35]A. Campbell, “An introduction to numerical methods in superconductors,” Journal of superconductivity and novel magnetism, vol. 24, no. 1-2, pp. 27-33, 2011.

[36]A. Hauser, “Calculation of superconducting magnetic bearings using a commercial FE-program (ANSYS),” Magnetics, IEEE Transactions on, vol. 33, no. 2, pp. 1572-1575, 1997.

[37]A. Stenvall, and T. Tarhasaari, “An eddy current vector potential formulation for estimating hysteresis losses of superconductors with FEM,” Superconductor Science and Technology, vol. 23, no. 12, pp. 125013, 2010.

[38]A. Stenvall, and T. Tarhasaari, “Programming finite element method based hysteresis loss computation software using non-linear superconductor resistivity and T-omega formulation,” Superconductor Science and Technology, vol. 23, no. 7, pp. 075010, 2010.

[39]F. Grilli, and S. P. Ashworth, “Measuring transport AC losses in YBCO-coated conductor coils,” Superconductor Science and Technology, vol. 20, no. 8, pp. 794, 2007.

[40]M. Zhang, J. Kvitkovic, S. Pamidi *et al.*, “Experimental and numerical study of a YBCO pancake coil with a magnetic substrate,” Superconductor Science and Technology, vol. 25, no. 12, pp. 125020, 2012.

[41]M. Zhang, K. Matsuda, and T. Coombs, “New application of temperature-dependent modelling of high temperature superconductors: Quench propagation and pulse magnetization,” Journal of Applied Physics, vol. 112, no. 4, pp. 043912-043912-8, 2012.

[42]V. K. Chari, and P. P. P. Silvester, Finite Elements in Electrical and Magnetic Field Problems: John Wiley & Sons, 1980.

[43]J. R. Clem, J. Claassen, and Y. Mawatari, "AC losses in a finite Z stack using an anisotropic homogeneous-medium approximation," Superconductor Science and Technology, vol. 20, no. 12, pp. 1130, 2007.

[44]W. Yuan, A. Campbell, Z. Hong *et al.*, "Comparison of AC losses, magnetic field/current distributions and critical currents of superconducting circular pancake coils and infinitely long stacks using coated conductors," Superconductor Science and Technology, vol. 23, no. 8, pp. 085011, 2010.

[45]W. Yuan, A. Campbell, and T. Coombs, "A model for calculating the AC losses of second-generation high temperature superconductor pancake coils," Superconductor Science and Technology, vol. 22, no. 7, pp. 075028, 2009.

[46]E. Pardo, J. Souc, and J. Kovac, "AC loss in ReBCO pancake coils and stacks of them: modelling and measurement," Superconductor Science and Technology, vol. 25, no. 3, pp. 035003, 2012.

[47]E. Pardo, "Modeling of coated conductor pancake coils with a large number of turns," Superconductor Science and Technology, vol. 21, no. 6, pp. 065014, 2008.

[48]L. Prigozhin, "Analysis of critical-state problems in type-II superconductivity," Applied Superconductivity, IEEE Transactions on, vol. 7, no. 4, pp. 3866-3873, 1997.

[49]L. Prigozhin, and V. Sokolovsky, "Computing AC losses in stacks of high-temperature superconducting tapes," Superconductor Science and Technology, vol. 24, no. 7, pp. 075012, 2011.

[50]F. Grilli, E. Pardo, A. Stenvall *et al.*, "Computation of losses in HTS under the action of varying magnetic fields and currents," Applied Superconductivity, IEEE Transactions on, vol. 24, no. 1, pp. 78-110, 2014.

[51]N. Magnusson, S. Hörnfeldt, J. Rabbers *et al.*, "Comparison between calorimetric and electromagnetic total ac loss measurement results on a BSCCO/Ag tape," Superconductor Science and Technology, vol. 13, no. 3, pp. 291, 2000.

[52]N. Magnusson, and S. Hörnfeldt, "Calorimetric apparatus for alternating current loss measurements on high-temperature superconductors," Review of scientific instruments, vol. 69, no. 9, pp. 3320-3325, 1998.

[53]R. Pei, A. Velichko, Y. Jiang *et al.*, "High-precision digital lock-in measurements of critical current and ac loss in hts 2g-tapes." pp. 3147-3150.

[54]W. Yuan, M. Ainslie, W. Xian *et al.*, "Theoretical and experimental studies on Jc and AC losses of 2G HTS coils," Applied Superconductivity, IEEE Transactions on, vol. 21, no. 3, pp. 2441, 2011.

[55]C. Barth, N. Bagrets, K. Weiss *et al.*, “Degradation free epoxy impregnation of REBCO coils and cables,” Superconductor Science and Technology, vol. 26, no. 5, pp. 055007, 2013.

[56]M.-J. Park, S.-Y. Kwak, W.-S. Kim *et al.*, “Stress analysis of HTS magnet for a 600 kJ SMES,” Applied Superconductivity, IEEE Transactions on, vol. 17, no. 2, pp. 1994-1997, 2007.

[57]W. Hassenzahl, “Superconducting magnetic energy storage,” IEEE Trans. Magn.;(United States), vol. 25, no. CONF-880812-, 1989.

[58]M. Beaudin, H. Zareipour, A. Schellenberglabe *et al.*, “Energy storage for mitigating the variability of renewable electricity sources: An updated review,” Energy for Sustainable Development, vol. 14, no. 4, pp. 302-314, 2010.

[59]W. Yuan, Second-generation high-temperature superconducting coils and their applications for energy storage: Springer, 2011.

[60]Y. Tang, J. Shi, and L. Ren, Superconducting magnetic energy storage and its application in power system: China Electric Power Press, 2009.

[61]J. Rogers, H. Boenig, J. Bronson *et al.*, “30-MJ superconducting magnetic energy storage (SMES) unit for stabilizing an electric transmission system,” Magnetics, IEEE Transactions on, vol. 15, no. 1, pp. 820-823, 1979.

[62]S. Schoenung, W. Meier, J. Hull *et al.*, “Design aspects of mid-size SMES using high temperature superconductors,” Applied Superconductivity, IEEE Transactions on, vol. 3, no. 1, pp. 234-237, 1993.

[63]A. Friedman, N. Shaked, E. Perel *et al.*, “HT-SMES operating at liquid nitrogen temperatures for electric power quality improvement demonstrating,” Applied Superconductivity, IEEE Transactions on, vol. 13, no. 2, pp. 1875-1878, 2003.

[64]C. J. Hawley, D. Cuiuri, C. D. Cook *et al.*, "Characterisation and control of a prototype HTS SMES device." p. 809.

[65]P. Tixador, M. Deleglise, A. Badel *et al.*, “First tests of a 800 kJ HTS SMES,” Applied Superconductivity, IEEE Transactions on, vol. 18, no. 2, pp. 774-778, 2008.

[66]P. Tixador, B. Bellin, M. Deleglise *et al.*, “Design and first tests of a 800 kJ HTS SMES,” Applied Superconductivity, IEEE Transactions on, vol. 17, no. 2, pp. 1967-1972, 2007.

[67]P. W. Parfomak, “Energy storage for power grids and electric transportation: A technology assessment,” Congressional Research Service, Tech. Rep. R, vol. 42455, 2012.

[68]B. Dunn, H. Kamath, and J.-M. Tarascon, “Electrical energy storage for the grid: A battery of choices,” Science, vol. 334, no. 6058, pp. 928-935, 2011.

[69]G. Ries, and H.-W. Neumueller, “Comparison of energy storage in flywheels and SMES,” Physica C: Superconductivity, vol. 357, pp. 1306-1310, 2001.

[70]D. Rastler, Electricity energy storage technology options: a white paper primer on applications, costs and benefits: Electric Power Research Institute, 2010.

[71]R. Howes, “Electrical Energy Storage and the Grid,” Bulletin of the American Physical Society, vol. 52, 2007.

[72]E. Hoffmann, J. Alcorn, W. Chen *et al.*, “Design of the BPA superconducting 30 MJ energy storage coil,” Magnetics, IEEE Transactions on, vol. 17, no. 1, pp. 521-524, 1981.

[73]W. V. Hassenzahl, “Superconducting magnetic energy storage,” Proceedings of the IEEE, vol. 71, no. 9, pp. 1089-1098, 1983.

[74]"Energy Storage Technologies for Distributed Energy Resources and Other Electric Power Systems," EPRI PEAC Corporation and Sandia National Laboratory, 2003.

[75]M. N. Wilson, Superconducting magnets: Clarendon Press Oxford, 1983.

[76]Y. Yanagisawa, K. Sato, R. Piao *et al.*, “Removal of degradation of the performance of an epoxy impregnated YBCO-coated conductor double pancake coil by using a polyimide-electrodeposited YBCO-coated conductor,” Physica C: Superconductivity, vol. 476, pp. 19-22, 2012.

[77]K. Mizuno, M. Ogata, and K. Nagashima, “An Innovative Superconducting Coil Fabrication Method with YBCO Coated Conductors,” Quarterly Report of RTRI, vol. 54, no. 1, pp. 46-51, 2013.

[78]J. Sarrao, W. Kwok, I. Bozovic *et al.*, *Basic Research Needs for Superconductivity. Report of the Basic Energy Sciences Workshop on Superconductivity, May 8-11, 2006*, DOESC (USDOE Office of Science (SC)), 2006.

[79]Y. Yoshida, M. Uesaka, and K. Miya, “Magnetic field and force analysis of high T c superconductor with flux flow and creep,” Magnetics, IEEE Transactions on, vol. 30, no. 5, pp. 3503-3506, 1994.

[80]P. W. Anderson, and Y. B. Kim, “Hard Superconductivity: Theory of the Motion of Abrikosov Flux Lines,” Reviews of Modern Physics, vol. 36, no. 1, pp. 39-43, 01/01/, 1964.

[81]E. Zeldov, N. M. Amer, G. Koren *et al.*, “Flux creep characteristics in high-temperature superconductors,” Applied Physics Letters, vol. 56, no. 7, pp. 680-682, 1990.

[82]O. Van der Meer, B. Ten Haken, and H. Ten Kate, “A model to describe the angular dependence of the critical current in a Bi-2223/Ag superconducting tape,” Physica C: Superconductivity, vol. 357, pp. 1174-1177, 2001.

[83]T. Kiss, M. Inoue, S. Nishimura *et al.*, “Angular dependence of critical current properties in YBCO coated tape under high magnetic field up to 18 T,” Physica C: Superconductivity, vol. 378, pp. 1113-1117, 2002.

[84]T. Kiss, and H. Okamoto, “Anisotropic current transport properties and their scaling in multifilamentry Bi-2223 Ag-sheathed tapes,” Applied Superconductivity, IEEE Transactions on, vol. 11, no. 1, pp. 3900-3903, 2001.

[85]G. M. Zhang, L. Z. Lin, L. Y. Xiao *et al.*, “A theoretical model for the angular dependence of the critical current of BSCCO/Ag tapes,” Physica C: Superconductivity, vol. 390, no. 4, pp. 321-324, 7/15/, 2003.

[86]T. Takematsu, R. Hu, T. Takao *et al.*, “Degradation of the performance of a YBCO-coated conductor double pancake coil due to epoxy impregnation,” Physica C: Superconductivity, vol. 470, no. 17, pp. 674-677, 2010.

[87]E. M. Petrie, Handbook of adhesives and sealants: McGraw-Hill Professional, 2000.

[88]H. Song, P. Brownsey, Y. Zhang *et al.*, “2G HTS coil technology development at SuperPower,” Applied Superconductivity, IEEE Transactions on, vol. 23, no. 3, pp. 4600806-4600806, 2013.

[89]M. Zhang, W. Wang, Z. Huang *et al.*, “AC Loss Measurements for 2G HTS Racetrack Coils With Heat-Shrink Tube Insulation,” Applied Superconductivity, IEEE Transactions on, vol. 24, no. 3, pp. 1-4, 2014.

[90]"http://www.superpower-inc.com/."

[91]"http://www.i-sunam.com/home/."

[92]“http://www.superox.ru/en/products/42-2G-HTS-tape/,” [access online] 20151014.

[93]W. Yuan, M. Ainslie, W. Xian *et al.*, “Theoretical and experimental studies on and AC losses of 2G HTS coils,” Applied Superconductivity, IEEE Transactions on, vol. 21, no. 3, pp. 2441-2444, 2011.

[94]N. Morley, J. Burris, L. Cadwallader *et al.*, “GaInSn usage in the research laboratory,” Review of Scientific Instruments, vol. 79, no. 5, pp. 056107, 2008.

[95]G. Ventura, and M. Perfetti, Thermal Properties of Solids at Room and Cryogenic Temperatures: Springer, 2014.

[96]B. Perea Solano, “Cryogenic Silicon Microstrip detector modules for LHC,” 2004.

[97]Y. Yanagisawa, E. Okuyama, H. Nakagome *et al.*, “The mechanism of thermal runaway due to continuous local disturbances in the YBCO-coated conductor coil winding,” Superconductor Science and Technology, vol. 25, no. 7, pp. 075014, 2012.

[98]D. N. Nguyen, F. Grilli, S. P. Ashworth *et al.*, "AC loss study of antiparallel connected YBCO coated conductors," Superconductor Science and Technology, vol. 22, no. 5, pp. 055014, 2009.

[99]M. Zhang, J.-H. Kim, S. Pamidi *et al.*, "Study of second generation, high-temperature superconducting coils: Determination of critical current," Journal of Applied Physics, vol. 111, no. 8, pp. 083902, 2012.

[100]L. Prigozhin, "On the Bean critical-state model in superconductivity," European Journal of Applied Mathematics, vol. 7, no. 3, pp. 237-248, 1996.

[101]M. Polak, P. Barnes, and G. Levin, "YBCO/Ag boundary resistivity in YBCO tapes with metallic substrates," Superconductor Science and Technology, vol. 19, no. 8, pp. 817, 2006.

[102]H. Fukushima, A. Ibi, H. Takahashi *et al.*, "Properties of long GdBCO coated conductor by IBAD-PLD method—The first GdBCO coil test," Applied Superconductivity, IEEE Transactions on, vol. 17, no. 2, pp. 3367-3370, 2007.

[103]J. Šouc, E. Pardo, M. Vojenčiak *et al.*, "Theoretical and experimental study of AC loss in high temperature superconductor single pancake coils," Superconductor Science and Technology, vol. 22, no. 1, pp. 015006, 2009.

[104]F. Gomory, M. Vojenciak, E. Pardo *et al.*, "AC losses in coated conductors," Superconductor Science and Technology, vol. 23, no. 3, pp. 034012, 2010.

[105]M. Chudy, Y. Chen, M. Zhang *et al.*, "Anisotropy of 2G HTS racetrack coils in external magnetic fields," Superconductor Science and Technology, vol. 26, no. 7, pp. 075012, 2013.

[106]D. Hu, M. Ainslie, J. Rush *et al.*, "DC characterization and 3D modelling of a triangular, epoxy-impregnated high temperature superconducting coil," Superconductor Science and Technology, vol. 28, no. 6, pp. 065011, 2015.

[107]J. Zhu, Z. Zhang, H. Zhang *et al.*, "Electric Measurement of the Critical Current, AC Loss, and Current Distribution of a Prototype HTS Cable," Applied Superconductivity, IEEE Transactions on, vol. 24, no. 3, pp. 1-4, 2014.

[108]W. R. Smythe, and W. R. Smythe, Static and dynamic electricity: McGraw-Hill New York, 1950.

[109]E. Weber, Electromagnetic Fields: Theory and Applications: Wiley, 1950.

[110]T. F. Coleman, and Y. Li, "A reflective Newton method for minimizing a quadratic function subject to bounds on some of the variables," SIAM Journal on Optimization, vol. 6, no. 4, pp. 1040-1058, 1996.

[111]J. Duron, F. Grilli, L. Antognazza *et al.*, "Finite-element modelling of YBCO fault current limiter with temperature dependent parameters," Superconductor Science and Technology, vol. 20, no. 4, pp. 338, 2007.

[112]D. Van der Laan, and J. Ekin, "Dependence of the critical current of YBa2Cu3O7 coated conductors on in-plane bending," Superconductor Science and Technology, vol. 21, no. 11, pp. 115002, 2008.

[113]Y. Iwasa, Case studies in superconducting magnets: design and operational issues: Plenum Press New York, 2009.

[114]J. Pitel, P. Kováč, M. Tropeano *et al.*, "Study of the potential of three different MgB 2 tapes for application in cylindrical coils operating at 20 K," Superconductor Science and Technology, vol. 28, no. 5, pp. 055012, 2015.

[115]H. Zhang, Z. Nie, X. Xiao *et al.*, "Design and Simulation of SMES System Using YBCO Tapes for Direct Drive Wave Energy Converters," Applied Superconductivity, IEEE Transactions on, vol. 23, no. 3, pp. 5700704-5700704, 2013.

[116]M. Däumling, and R. Flükiger, "Factors determining the magnetic field generated by a solenoid made with a superconductor having critical current anisotropy," Cryogenics, vol. 35, no. 12, pp. 867-870, 12//, 1995.

[117]Q. Wang, J. Liu, S. Song *et al.*, "High Temperature Superconducting YBCO Insert for 25 T Full Superconducting Magnet," Applied Superconductivity, IEEE Transactions on, vol. 25, no. 3, pp. 1-5, 2015.

[118]H. W. Weijers, W. D. Markiewicz, A. J. Voran *et al.*, "Progress in the Development of a Superconducting 32 T Magnet With REBCO High Field Coils," Applied Superconductivity, IEEE Transactions on, vol. 24, no. 3, Jun, 2014.

[119]A. V. Gavrilin, L. Jun, B. Hongyu *et al.*, "Observations from the Analyses of Magnetic Field and AC Loss Distributions in the NHMFL 32 T All-Superconducting Magnet HTS Insert," Applied Superconductivity, IEEE Transactions on, vol. 23, no. 3, pp. 4300704-4300704, 2013.

[120]C. Senatore, M. Alessandrini, A. Lucarelli *et al.*, "Progresses and challenges in the development of high-field solenoidal magnets based on RE123 coated conductors," Superconductor Science and Technology, vol. 27, no. 10, pp. 103001, 2014.

[121]Y. Yanagisawa, Y. Kominato, H. Nakagome *et al.*, "Magnitude of the screening field for YBCO coils," Applied Superconductivity, IEEE Transactions on, vol. 21, no. 3, pp. 1640, Jun, 2011.

[122]G. Wojtasiewicz, T. Janowski, S. Kozak *et al.*, "Experimental Investigation of the Model of Superconducting Transformer With the Windings Made of 2G HTS Tape," Applied Superconductivity, IEEE Transactions on, vol. 22, no. 3, pp. 5500504-5500504, 2012.

[123]M. Zhang, M. Chudy, W. Wang *et al.*, "AC loss estimation of HTS armature windings for electric machines," Applied Superconductivity, IEEE Transactions on, vol. 23, no. 3, pp. 5900604-5900604, 2013.

[124]"http://www.superpower-inc.com/content/2g-hts-wire," [access online] 20151014.

[125]H. Tonsho, M. Toyoda, S. Fukui *et al.*, "Numerical evaluation of AC loss in high temperature superconducting coil," Applied Superconductivity, IEEE Transactions on, vol. 14, no. 2, pp. 674-677, 2004.

[126]J. Claassen, "An approximate method to estimate ac loss in tape-wound superconducting coils," Applied physics letters, vol. 88, no. 12, pp. 122512, 2006.

[127]M. Zhang, W. Yuan, D. K. Hilton *et al.*, "Study of second-generation high-temperature superconducting magnets: the self-field screening effect," Superconductor Science and Technology, vol. 27, no. 9, pp. 095010, 2014.

[128]A. F. d. O. Falcao, "Wave energy utilization: A review of the technologies," Renewable and sustainable energy reviews, vol. 14, no. 3, pp. 899-918, 2010.

[129]D. A. Halamay, T. K. Brekken, A. Simmons *et al.*, "Reserve requirement impacts of large-scale integration of wind, solar, and ocean wave power generation," Sustainable Energy, IEEE Transactions on, vol. 2, no. 3, pp. 321-328, 2011.

[130]W. Yuan, W. Xian, M. Ainslie *et al.*, "Design and test of a superconducting magnetic energy storage (SMES) coil," Applied Superconductivity, IEEE Transactions on, vol. 20, no. 3, pp. 1379-1382, 2010.

[131]A. G. Ter-Gazaran, Energy storage for power systems: The Institution of Engineering and Technology, 1994.

[132]H. Bindner, T. Cronin, P. Lundsager *et al.*, Lifetime modelling of lead acid batteries, 2005.

[133]"http://www.trojanbattery.com/pdf/GEL_SS_Web.pdf," [access online] 20150714.

[134]A. Ruddell, A. Dutton, H. Wenzl *et al.*, "Analysis of battery current microcycles in autonomous renewable energy systems," Journal of Power sources, vol. 112, no. 2, pp. 531-546, 2002.

[135]S. D. Downing, and D. Socie, "Simple rainflow counting algorithms," International Journal of Fatigue, vol. 4, no. 1, pp. 31-40, 1982.

[136]M. Matsuichi, and T. Endo, Fatigue of metals subjected to varying stress, 1968.

[137]P. Edwards, Cumulative damage in fatigue with particular reference to the effects of residual stresses: Citeseer, 1969.

[138]"http://www.mathworks.com/matlabcentral/fileexchange/3026-rainflow-counting-algorithm," [access online] 20150714.

[139]A. Akhil, S. Swaminathan, and R. K. Sen, *Cost analysis of energy storage systems for electric utility applications*, Sandia National Labs., Albuquerque, NM (United States), 1997.

[140]R. Giese, *Superconducting energy storage*, Argonne National Lab., IL (United States), 1993.

[141]J. Schwartz, E. E. Burkhardt, and W. R. Taylor, *Preliminary Investigation of Small Scale Superconducting Magnetic Energy Storage (SMES) Systems*, 1996.

[142]S. Stavrev, and B. Dutoit, "*Frequency dependence of AC loss in Bi(2223)Ag-sheathed tapes,*" Physica C: Superconductivity*,* vol. 310, no. 1–4, pp. 86-89, 1998